A NUMERICAL STUDY OF TOPOGRAPHICAL EFFECTS ON FLOW REGIMES IN THE LOWER ATMOSPHERE

by

John David Lindeman
A Dissertation
Submitted to the
Graduate Faculty
of
George Mason University
in Partial Fulfillment of
the Requirements for the Degree
of
Doctor of Philosophy
Computational Sciences and Informatics

Committee:

	Dr. Zafer Boybeyi, Dissertation Director
	Dr. Dave Broutman, Committee Member
	Dr. Nash'at Ahmad, Committee Member
	Dr. Joseph Chang, Committee Member
	Dr. Dimitrios Papaconstantopoulos, Department Chairperson
	Dr. Peter Becker, Associate Dean for Graduate Programs, College of Science
	Dr. Vikas Chandhoke, Dean, College of Science

Date: 4/17/2008

Spring Semester 2008
George Mason University
Fairfax, VA

A Numerical Study of Topographical Effects on Flow Regimes in the Lower Atmosphere

A dissertation submitted in partial fulfillment of the requirements for the degree of Doctor of Philosophy at George Mason University

By

John David Lindeman
Master of Science
University of Reading, UK, 1996
Bachelor of Science
Millersville University, PA, 1995

Director: Dr. Zafer Boybeyi, Professor
Department of Computational and Data Sciences

Spring Semester 2008
George Mason University
Fairfax, VA

Acknowledgments

I would like to thank the members of my dissertation committee: Dr. Zafer Boybeyi, Dr. Dave Broutman, Dr. Nash'at Ahmad, and Dr. Joseph Chang - without whom this dissertation would not have been possible. I would also like to thank my co-workers at the Naval Research Laboratory, Dr. Stephen Eckermann and Dr. Jun Ma, for their assistance and guidance at our weekly meetings. Thirdly, I would like to thank the folks at the College of Science such as Jozsef Bakosi and Dr. Fernando Carmelli for their tech support. I would also like to thank my family and friends for all of their support. Finally, I would like to thank Dr. Jim Doyle for his assistance regarding meteorological modeling, the WRF team, and the National Science Foundation for funding this endeavor.

Table of Contents

List of Figures

List of Symbols

Note that the subscript (o) appended to a variable refers to a reference value, and that the apostrophe (') refers to a perturbation quantity. q denotes a generic variable, while $\overline{q}$ is an averaged quantity.

Chapter 1

Fr_h (also just Fr) Height (h) dependent Froude number

Fr_h Half-width (a) dependent Froude number

N Static stability

g Gravity (9.8 ms^{-2}

a half-width along wind direction

b half-width normal to wind direction

θ Potential temperature

ρ Density

p Pressure

U, V background uniform wind speed

u, v, w Linearized wind perturbation velocity components

x, y, z Cartesian coordinates

t time

$Re[...]$ Real component of a complex number

L_x, L_y, L_z Wavelength components

$h(x, y)$ Orography

h_m Maximum orographic height

$\kappa = (k, l, m)$ Total wavenumber and the components

ϕ Wave phase

ω Frequency

$\hat{\omega}$ Intrinsic frequency

$c = (c_x, c_z)$ Wave phase speed and the components (2D)

$c_G = (c_{Gx}, c_{Gz})$ Total group velocity and the components (2D)

$\tilde{w}$ Fourier transform of w

$\tilde{h}$ Fourier transform of h

l Scorer parameter

S Heterogeneity term

i Imaginary number

T Temperature

η Vertical displacement

D Drag term

z_c Dividing streamline height

α Drag and/or pressure acceleration term in Sheppard's formula

Chapter 2

WRF Weather, Research, and Forecasting model

$\overline{uw}$, $\overline{uw}$ Linear gravity wave momentum fluxes

FT Fourier Transform method

FT_w FT method initialized by WRF w field

FT_o FT method initialized by surface vertical displacement (orography)

Appendix A

p_h Hydrostatic pressure component

p_{hs} Pressure on terrain-following surface

p_{hs} Pressure on top of WRF model domain

$\mu = p_{hs} - p_{ht}$ Column mass

η Mass vertical coordinate

$\mathbf{V} = \mu V$ Flux form of the velocity

ϕ Geopotential

α Inverse of density

$\dot{\omega}$ Contravariant vertical velocity

F_q WRF model turbulent forcing terms

R_d Gas constant for dry air

c_p Specific heat at constant pressure

c_v Specific heat at constant volume

K_h Horizontal eddy viscosity

K_v Vertical eddy viscosity

D Deformation tensor

e Turbulent kinetic energy

$\triangle x$ Horizontal grid spacing

C, C_k TKE constants

l_{cr} Critical length scale

P_r Prandtl number

k von Karman constant

$\Phi = (U, V, W, \Theta, \phi', \mu')$ Generic variable used in Runge-Kutta timestep scheme

$\Phi*, \Phi**$ predictor terms for the RK scheme

q'' Fractionally small time steps for acoustic terms

$\triangle t$ Maximum possible timestep

Cr Courant number used in timestep formulation

γ_d Divergence damping coefficient (diffusive)

γ_c External mode damping coefficient

β Off-centering term in acoustic-step vertical momentum equation

τ Rayleigh damping term

γ_r Rayleigh damping coefficient

Abstract

A NUMERICAL STUDY OF TOPOGRAPHICAL EFFECTS ON FLOW REGIMES IN THE LOWER ATMOSPHERE

John David Lindeman, PhD

George Mason University, 2008

Dissertation Director: Dr. Zafer Boybeyi

Orographically generated gravity waves, or mountain waves, have been the focus of much research for decades because of their importance on the general mean atmospheric circulation. These waves affect the flow on scales which are too small to be resolved by global weather and climate models, and so their impact on the larger scale flow must be parameterized. Linear theory has proven useful for obtaining a quantitative understanding of wave processes and their effects on the background flow, though one must assume that the low level flow in mountainous regions is approximately linear. Numerical simulations and field experiments indicate that this is often not the case, however, as nonlinear effects can dominate the flow near the orography. These nonlinear effects, which include processes such as flow splitting around a mountain or upstream blocking of the flow, affect gravity wave generation and decrease the accuracy of predictions based on linear theory.

The purpose of this dissertation is to investigate the extent that linear theory-based mountain wave predictions can be improved by using an alternative initialization scheme. Linear orographic gravity wave models traditionally have been initialized at the lower boundary assuming the orography is equivalent to the surface vertical displacement field. While this method works when wave-induced perturbations are small compared to the mean

flow, this has been shown to fail in weak flow regimes and tall mountains. We introduce an initialization technique where the linear model is initialized on a horizontal plane with results from a corresponding simulation from a nonlinear numerical model. The height level of initialization must be in a region in which the flow can be approximated by linear theory, and in practice this occurs above the low level nonlinear processes in the vicinity of the mountain.

We show that this method leads to greater accuracy in the solutions of the wavefield above the orography. This new method is tested for flow regimes of uniform background wind and stability, and for simple bell shaped hills and more complex and realistic orography. Parameters derived from linear theory which are useful for global weather models are shown to be significantly affected by the new initialization scheme. These results have the potential to quantitatively improve global weather model mountain wave parameterization schemes in the relatively common instance of orographically-induced nonlinear flows , as well as to provide quick and accurate forecasts of wave activity for the aviation community.

Chapter 1: Introduction

1.1 The Meteorological Significance of Mountain Waves

Mountains influence the atmospheric circulation on many different spatial and time scales, ranging from generating local mountain / valley flows to impacting the global atmospheric circulation (Smith, 1979). A subset of this general topic, mountain waves, is the principal focus of this dissertation. Mountain waves are atmospheric gravity waves caused by orographically generated buoyancy oscillations in a stably stratified flow. These waves are important part of the overall atmospheric circulation because of their ability to transport momentum fluxes over considerable distances, and it is essential for these processes to be accurately represented in global circulation models. Mountain waves occur on many different spatial scales, and due to the complex nature of the underlying orography and associated nonlinear processes the wave structure itself can be very complex (Nappo, 2002). Thus, parameterization schemes for estimating effects of wave fields below the resolution capabilities of forecasting models is very important for forecast accuracy, and research into improving these schemes continues presently (Kim et al., 2002). The research in this dissertation is, in part, motivated by ongoing efforts to improve these parameterization schemes.

Our knowledge of mountain wave dynamics is incomplete, even after many decades of research. Studies generally approach the problem from one or more of three broad categories: (1) analytical solutions, (2) field experiments, and (3) numerical simulations. Each method has its own advantages and disadvantages, and all have contributed significantly to our understanding and prediction of wave processes. Analytical solutions are generally used for wave studies in which the linear approximation is valid, where physical characteristics of the wavefield are assumed to be directly related to the orography (Nappo, 2002). Solutions for the wavefield and effects such as the wave drag are readily available from these analytical techniques. In section 1.3 we explore the linear approximation and analytical solutions in greater detail. When the linear approximation is no longer appropriate, however, researchers tend to rely more upon environmental data from field experiments and nonlinear numerical experiments.

Several field experiments over the years have well documented accounts of mountain waves in flow regimes where low level nonlinear processes dominate. Characteristically, these processes arise as a result of the interaction of the flow with the orography and include flow splitting around mountains, upstream flow blocking by an obstacle, and lee vortex generation. Other nonlinear processes can cause wave breaking and internal drag (though not necessarily at low levels), and usually result from wave interaction with the background flow such as when the waves approach a critical level (Wurtele et al., 2002). The 1972 Boulder, Colorado windstorm, the Pyrenees Experiment (PYREX), and the Alps field campaign (MAP) have in particular contributed to our knowledge of mountain waves in nonlinear flow regimes, and will be discussed in section 1.4.2.

Numerical simulations have become more common as computational capabilities increase and weather models are more refined and complex. Many state-of-the-art numerical mesoscale meteorological models today are fully nonlinear, nonhydrostatic, and have some type of terrain-following lower boundary that is convenient for simulating the orographic forcing of the flow (Pielke, 2002). Researchers who apply results from numerical simulations often do so for idealized mountain wave studies or in conjunction with field experiments. Simulations are currently perhaps the most commonly used tool in mountain wave research.

Many different applications such as weather, climate, and aviation forecasting benefit from mountain wave research (Nappo, 2002; Eckermann et al., 2006b). In this dissertation, we use numerical simulations from both linear and nonlinear models to investigate how low level nonlinear flows influence mountain wave generation. More specifically, a new 'hybrid' initialization scheme is developed in which a linear model is initialized with the flow field from a corresponding nonlinear simulation at a height above the low level nonlinear processes (Lindeman et al., 2008). The new hybrid initialization scheme enables the linear wavefield model to produce gravity wave forecasts on a sufficiently expedient time scale. Applications from this research should be of benefit for gravity wave parameterization schemes used by global weather forecasting models and mountain wave and turbulence forecasts for the aviation community.

This dissertation is organized as follows: For the remainder of this chapter the brief overview of linear and nonlinear flow processes is examined in greater detail. In chapter 2, the linear and nonlinear models are described and evaluated for different linear wavefield analytical solutions. In chapter 3 we examine two idealized nonlinear flow regimes, and assess wavefield generation and physical characteristics of the waves. The accuracy of the hybrid initialization scheme is assessed for flows in realistically complex orographic areas in chapter 4, with an emphasis on the Big Island of Hawaii. In chapters 3 and 4, quantitative estimates of the wave momentum fluxes are also presented. We conclude our research in chapter 5, which also features a discussion of possible avenues for future research.

1.2 A Discussion of Linear and Nonlinear Wave Regimes

The Froude number (Fr) is used extensively to describe orographic flow regimes (Baines, 1995). Expressed as a ratio of inertial to gravitational forces on a flow, Fr has been applied extensively in engineering applications, and many manifestations of this parameter exist to describe flow-obstacle interactions.

In the mountain meteorological community, two versions of Fr are most widely used (Baines, 1995). We denote Fr_h which is expressed in terms of an obstacle's maximum height h_m. Another form of the Froude number is used in relation to the half-width of an obstacle,

Fr_a, where a is half the width of the obstacle at half of its maximum height. Fr_h is most often used to describe the linear or nonlinear nature of a flow, and is expressed as:

$$Fr_h = \frac{U}{Nh_m}, \tag{1.1}$$

where U is the background wind speed, and N is the buoyancy frequency:

$$N^2 = \frac{g}{\theta_0}\frac{d\theta}{dz}.$$

g is gravity and θ is the potential temperature. The subscript '0' denotes an averaged value of θ over the vertical layer δz. Note that U and N are uniform values. If the flow over the hill is described in simple energy arguments, and all other processes such as pressure acceleration, internal drag, diabatic effects, etc. are ignored, the Froude number can be described in terms of the ability of an upstream air parcel to ascend a mountain.

When $Fr_h > 1$ the air parcel contains sufficient kinetic energy (as represented by U) to travel over the mountain. When $Fr_h < 1$ the air parcel lacks the kinetic energy and does not ascend the hill, resulting in nonlinear processes such as the parcel being deflected around the mountain or becoming stagnant upstream. When Fr_h is greater than 1, the flow can be reasonably approximated by linear theory (particularly when $Fr_h >> 1$). When $Fr_h < 1$ nonlinear processes are important. Fr_h also refers to the steepness of a wavefield (Baines, 1995), which attain their maximum steepness when $Fr_h = 1$.

Research into nonlinear orographic flow regimes have been typically classified in terms of Fr_h (Schär and Durran, 1997; Miranda and James, 1992; Smolarkiewicz and Rotunno, 1989a; Smolarkiewicz and Rotunno, 1989b), though the half-width dependent Froude number, Fr_a, is useful when analyzing wavefield propagation characteristics (Kaimal and Finnigan, 1994; Baines, 1995):

$$Fr_a = \frac{U}{Na}, \tag{1.2}$$

In this case, Fr_a is regarded as the ratio of the inertial frequency U/a to the atmosphere's natural frequency response N. When $Fr_a < 1$ bouyancy effects are important and the atmosphere can support gravity waves generated by the obstacle (mountain). When $Fr_a > 1$, inertial effects dominate the flow and the atmospheric cannot support gravity wave propagation. Instead, flow perturbations induced by the orography decrease with height. The first case can lead to the generation of propagating gravity waves, while evanescent (decaying) wave modes occur in the second case.

1.3 Linear Wave Theory

Much of what we know about mountain wave activity comes from linear analytical solutions of mountain waves (Nappo, 2002), and so a description explained within this context is given presently. Linear systems provide for a relatively easy understanding of mountain wave dynamics, and derived wave quantities such as the momentum flux have been applied in global weather model parameterization schemes.

1.3.1 The Dispersion Relationship

The dispersion relationship is central to one of the models used in this research, the Fourier Transform method, as it expresses a relationship between wave number and frequency. Here we derive a dispersion relationship, though we restrict the discussion to a two-dimensional flow oriented along the x-axis. We also neglect the effects of rotation and employ the Boussinesq approximation, where density is constant everywhere except in the buoyancy term of the vertical momentum equation. Thus, the atmosphere is incompressible and density variations are considered to be small perturbations in the basic state density field (Holton, 1992). We begin with the basic state equations (neglecting rotation):

$$\frac{\partial u}{\partial t} + u\frac{\partial u}{\partial x} + w\frac{\partial u}{\partial z} + \frac{1}{\rho}\frac{\partial p}{\partial x} = 0 \tag{1.3}$$

$$\frac{\partial w}{\partial t} + u\frac{\partial w}{\partial x} + w\frac{\partial w}{\partial z} + \frac{1}{\rho}\frac{\partial p}{\partial z} + g = 0 \tag{1.4}$$

$$\frac{\partial u}{\partial x} + \frac{\partial w}{\partial z} = 0 \tag{1.5}$$

$$\frac{\partial \theta}{\partial t} + u\frac{\partial \theta}{\partial x} + w\frac{\partial \theta}{\partial z} = 0 \tag{1.6}$$

where u and w are the x and z components of the wind velocity, respectively, p is pressure, and ρ is density. The equations are linearized by assuming that the prognostic variables $q = \overline{q} + q'$, where $\overline{q}$ denotes the basic state unchanging flow and q' is the perturbation component of the flow. In this case, $\overline{u}(z)$, $\overline{\theta}(z)$, and $\overline{p}(z)$ are height dependent, and $\overline{w} = 0$. Since the Boussinesq approximation is being employed, we use $\rho = \rho_0 + \rho'$, where ρ_0 is constant everywhere. We also assume that the mean state atmosphere is hydrostatic, so that:

$$\frac{d\overline{p}}{dz} = -\rho_0 g$$

To obtain the linearized equations, we substitute the mean and perturbation variables into Eqns. (1.3) to (1.6), and neglect terms containing the product of perturbation quantities. Assuming that the perturbations to the background state are caused by gravity waves, we also ignore wave-wave interactions (i.e. the perturbation product terms). This means that while wave superposition can lead to wave packets, waves cannot interact to form new waves or destroy existing waves (Nappo, 2002).

In the linearized Boussinesq formulation of the basic state equation set, the buoyancy term contains a density perturbation variable. It is convenient to substitute ρ' with θ' by noting that density fluctuations due to pressure changes are small compared to density fluctuations due to temperature changes (Holton, 1992), so that $\theta'/\overline{\theta} = -\rho'/\rho_0$. For convention, the perturbation wind velocity components are denoted as (u, v, w). Eqns. (1.3) to (1.6) are then transformed to:

$$\frac{\partial u}{\partial t} + \overline{u}\frac{\partial u}{\partial x} + \frac{1}{\rho_0}\frac{\partial p'}{\partial x} = 0 \tag{1.7}$$

$$\frac{\partial w}{\partial t} + \overline{u}\frac{\partial w}{\partial x} + \frac{1}{\rho_0}\frac{\partial p'}{\partial z} + \frac{\theta'}{\overline{\overline{\theta}}_0}g = 0 \tag{1.8}$$

$$\frac{\partial u}{\partial x} + \frac{\partial w}{\partial z} = 0 \tag{1.9}$$

$$\frac{\partial \theta'}{\partial t} + \overline{u}\frac{\partial \theta'}{\partial x} + w\frac{\partial \overline{\theta}}{\partial z} = 0 \tag{1.10}$$

Eqns. (1.7) to (1.10) can then be manipulated to eliminate variables u, θ', and p' to form a single equation for w:

$$\left(\frac{\partial}{\partial t}+\overline{u}\frac{\partial}{\partial x}\right)^2\left(\frac{\partial^2 w}{\partial x^2}+\frac{\partial^2 w}{\partial z^2}\right)+N^2\frac{\partial^2 w}{\partial x^2}=0. \tag{1.11}$$

The next step is to find a solution for w. We would like to note here that it is desirable to find solutions to these type of wave problems in terms of sinusoidal wave motions. An important property of these wave motions is that the period (time) of an oscillation is independent of the amplitude of the oscillation. While this property technically only holds true for oscillations of sufficiently small amplitude, sinusoidal-based solutions are perfectly valid for linear wave theory (Holton, 1992).

As will be explained later, many wave solutions require a Fourier Series of sinusoidal waves. However, for Eqn. (1.11), we seek a solution of the form:

$$w = Re[\hat{w}e^{-i\phi}] = w_r cos\phi - w_i sin\phi,$$

where $\hat{w} = w_r + iw_i$ is a complex amplitude with real part w_r and imaginary part w_i. The wave phase $\phi = kx + mz - vt$ is assumed to depend linearly on z as well as on x and t. Since the solution is always sinusoidal in x, the horizontal wave number $k = 2\pi/L_x$ is real. However, the vertical wave number $m = 2\pi/L_z = m_r + im_i$ can be complex where m_r represents sinusoidal variations in z and m_i represents exponential decay or growth in z depending on whether m_i is positive or negative. For cases where m is real, we can substitute our assumed solution to Eqn. (1.12) to derive the following dispersion relationship:

$$(v-\overline{u}k)^2(k^2+m^2)-N^2k^2=0,$$

or

$$\hat{\omega} = \omega - Uk = \pm Nk/(k^2 + m^2)^{1/2} = \pm Nk/ \mid \kappa \mid, \tag{1.12}$$

where κ the total wave number is a vector $\kappa = (k, m)$. $\hat{\omega}$ is known as the intrinsic frequency, which is the frequency relative to the mean wind, and the plus (minus) sign is to be taken for eastward (westward) propagation relative to the mean wind (Holton, 1992). The dispersion relationship is an important parameter in linear wave theory expressing the relatinship between frequency (ω) and wavenumber (k). Note that mountain waves are stationary relative to the ground, and so their frequency $\omega = 0$.

The wave group velocity is obtained from the dispersion relation. Relative to the ground, the wave fronts are stationary and so the wave phase speed $c = 0$. The horizontal and vertical group velocity components $c_G = (c_{Gx}, c_{Gz})$ are expressed as (respectively):

$$c_{Gx} = \frac{\partial \omega}{\partial k} = \overline{u} + \frac{\partial \hat{v}}{\partial k} = \overline{u}\frac{k^2}{k^2 + m^2}, \tag{1.13}$$

$$c_{Gz} = \frac{\partial \omega}{\partial m} = \overline{u} + \frac{\partial \hat{v}}{\partial m} = \overline{u}\frac{km}{k^2 + m^2}. \tag{1.14}$$

1.3.2 Analytical Mountain Wave Solutions

Linearized analytical mountain wave solutions are often used for numerical model validation. An analytical solution developed by Smith (1979) is used as a benchmark case to the numerical models used in this dissertation. This particular solution has been similarly used by Durran and Klemp (1983) and Doyle (2005).

In a similar manner to the derivation of a single equation for w presented earlier in section 1.3.1, Smith (1979) derives an expression for w based on the linearized equations of state. The expression for w is (Eqn. 2.23) of (Smith, 1979):

$$\frac{\partial^2 \tilde{w}}{\partial x^2} + \frac{\partial^2 \tilde{w}}{\partial z^2} + l^2(z)\tilde{w} = 0, \tag{1.15}$$

where

$$\tilde{w} \equiv [\overline{\rho}/\rho_0]^{1/2} w,$$

and l is the Scorer parameter, which is expressed as:

$$l^2(z) \equiv \frac{N^2}{\overline{u}^2} + \frac{\overline{S}}{\overline{u}}\frac{\partial \overline{u}}{\partial z} - \frac{1}{4}\overline{S}^2 + \frac{1}{2}\frac{\partial \overline{S}}{\partial z} - \frac{1}{\overline{u}}\frac{\partial^2 \overline{u}}{\partial z^2} \tag{1.16}$$

The coefficient $\overline{S} \equiv \frac{d}{dz} ln\overline{\rho}(z)$ is not related to the generation of Bouyancy forces, but describes the effect of density variations in the divergence of the velocity field and the vertical variation in inertia in the momentum equations (Smith, 1979). The terms involving $\overline{S}$ are usually neglected in Eqn. (1.16), which is the equivalent to making the Boussinesq approximation, as density variations are only important as they affect the Bouyancy term (first term RHS). The wind curvature term (last term in Eqn. (1.16)) is also neglected often, though it can become important if vertical shear becomes significant (Smith, 1979).

We now seek a solution for $\tilde{w}$ over an isolated bell-shaped obstacle. Smith (1979) uses a Fourier integral to derive a solution:

$$\hat{w} = \int_{-\infty}^{\infty} \tilde{w} e^{ikx} dk$$

We then obtain an expression for $\tilde{w}(k, z)$ by substitution into Eqn. (1.16):

$$\frac{\partial^2 \tilde{w}}{\partial z^2} + [l^2(z) - k^2]\tilde{w} = 0$$

The lower boundary condition is then expressed as:

$$\tilde{w}(k, 0) = \overline{u}(0) ik\tilde{h}(k),$$

where $\tilde{h}(k)$ is the Fourier transform of the mountain shape:

$$\tilde{h}(k) = \int_{-\infty}^{\infty} h(x) e^{-ikx} dx$$

For the case of no mean shear (i.e. l^2 is constant), solutions for $\tilde{w}$ depend on whether $k^2 > l^2$ or $k^2 < l^2$, and the upper boundary condition must be specified to ensure a realistic behaving solution. When $k^2 > l^2$ the gravity wave solution is said to be evanescent, and the upper boundary condition is set so that solution decays as $z \to \infty$. When $k < l^2$, a propagating gravity wave solution results, and so the upper boundary is specified so that the phase lines tilt upstream and energy is propagated upward. In the evanescent case:

$$\tilde{w}(k, z) = \tilde{w}(k, 0) exp[-(k^2 - l^2)^{1/2} z], \tag{1.17}$$

and in the propagating case:

$$\tilde{w}(k, z) = \tilde{w}(k, 0) exp[i(l^2 - k^2)^{1/2} z], \tag{1.18}$$

Smith (1979) solves for w' in terms of the vertical displacement of a streamline, $\eta(x, z)$:

$$w = \overline{u}\frac{\partial \eta}{\partial x} \tag{1.19}$$

Two solutions for η are obtained, one for the evanescent case and the other for the propagating wave case. The determining factor for the gravity wave regime is the dimensionless quantity al, where a is the mountain half-width and l is the Scorer parameter. al is proportional to the ratio of the time it takes for an air parcel to cross the ridge to the period of a buoyancy oscillation $2\pi/N$. When $al << 1$, an air parcel will cross a ridge quickly enough so that buoyancy forces do not affect the parcel's motion. This case, the evanescent wave case, might be characteristic of a narrow ridge, weak stability, strong horizontal wind speed, or a combination thereof. The solution for η when $al << 1$ turns out to be (Smith, 1979):

$$\eta(x, z) = \left(\frac{\rho_0}{\overline{\rho}}\right)^{1/2} \frac{h_m a(a+z)}{(a+z)^2 + x^2} \tag{1.20}$$

A solution for w can be seen in Fig. 1.1. For this particular case, $\overline{u} = 20\text{ms}^{-1}$, $a = 220\text{m}$, $h_m = 100\text{m}$, and $N = 0.0182\text{s}^{-1}$. The atmosphere is isothermal, so that $T = \textit{constant} = 288\text{K}$. $Fr_h = 11$, $Fr_a = 5$, and $al = 1/5$ for this case. As can be seen in the plot, buoyancy forces do not significantly affect the flow as the vertical velocity field shows no sign of propagating wave activity. Instead, rising motion occurs on the windward side of the ridge and sinking motion of an identical magnitude over the lee slope.

The solution is significantly different when $al >> 1$. In this case, the propagating gravity wave case, air parcels traversing the ridge are significantly affected by buoyancy forces. The streamline solution takes the form:

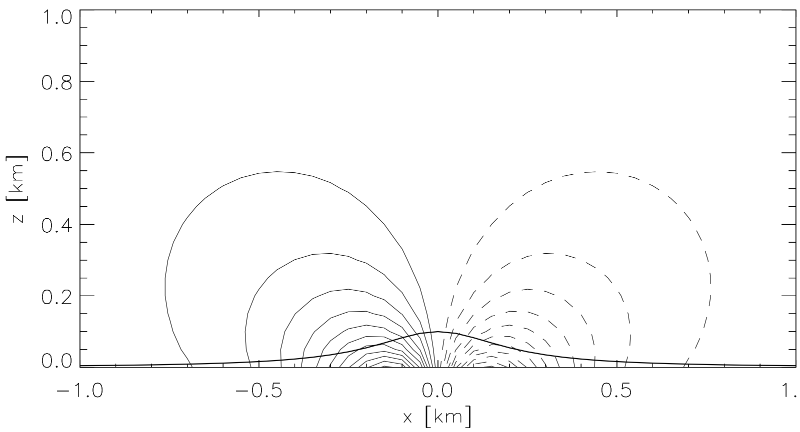

Figure 1.1: Vertical velocity w contours for the evanescent case. Contour intervals are 0.5ms^{-1}, with the zero interval omitted and negative contours dashed. Minimum value: -5.6ms^{-1}, maximum value: 5.6ms^{-1}

$$\eta(x,z) = \left(\frac{\rho_0}{\overline{\rho}}\right)^{1/2} h_m a \frac{(a\cos lz - x\sin lz)}{a^2+x^2} \tag{1.21}$$

In this case, to satisfy the criteria that $al >> 1$, the mountain half-width $a = 10$km, $Fr_a = 0.11$, and $al = 9.12$. Otherwise, all other variables are the same as in the evanescent case to generate the w field in Fig. 1.2. Nondispersive vertically propagating gravity waves are clearly evident, as energy is propagating vertically away from the mountain.

Gravity waves propagation when $al >> 1$ is usually referred to as hydrostatic waves. When $al \sim 1$ gravity wave propagation can occur, though buoyancy forces are not so important as they are in the hydrostatic gravity wave case. Smith (1979) outlines a solution for η when $al \sim 1$, termed nonhydrostatic case. The derivation is considerably more complex than in the previous two cases, but an expression for η is derived as:

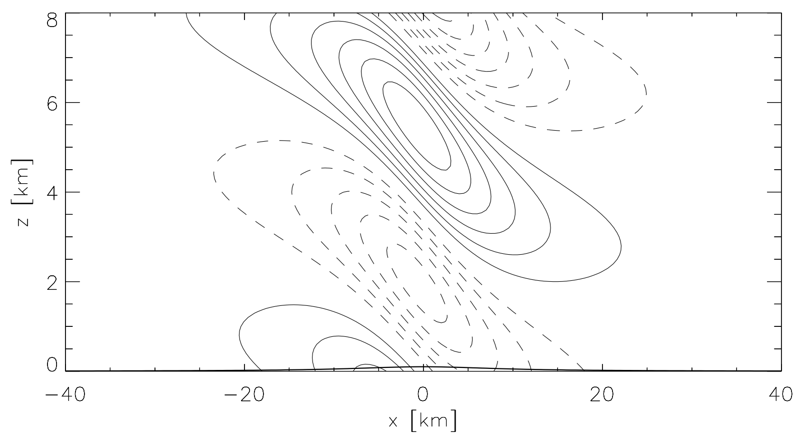

Figure 1.2: Vertical velocity w contours for the hydrostatic case. Contour intervals are $0.04 \mathrm{ms}^{-1}$, with the zero interval omitted and negative contours dashed. Minimum value: $-0.32 \mathrm{ms}^{-1}$, maximum value: $0.27 \mathrm{ms}^{-1}$. Note that horizontal and vertical length scales are different from those in Fig. 1.1.

$$\eta(x,z) = \left(\frac{\rho_0}{\overline{\rho}}\right)^{1/2} (2\pi)^{1/2} \left(\frac{(l^2 - k^{*2})^{3/2}}{l^2 z}\right)^2 h_m a$$
$$e^{-k^* a} \cos\left(l^2 - k^{*2})^{1/2} z + k^* x - \frac{\pi}{4}\right) \tag{1.22}$$

where $k^*(x,z) = l/[(z/x)^2 + 1]^{1/2}$. k^* represents a range of wave numbers whose contribution to the wave field do not cancel each other out downstream of the mountain. Waves of wave number $k*$ propagate away downstream of the mountain. The resulting wave field (shown in Fig. 1.3 for $a = 1100$m) features a trail of nonhydrostatic waves trailing behind the vertically propagating hydrostatic gravity wave. The nonhydrostatic gravity waves decrease in amplitude further downstream of the mountain. Note that the solution is technically only valid when $x > 0$, and is not valid directly above the mountain (Smith, 1979).

Pressure perturbations p' and the horizontal velocity perturbation u are also useful

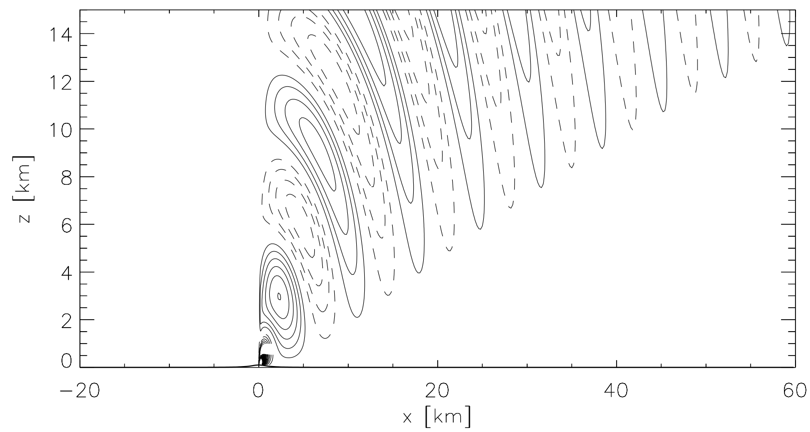

Figure 1.3: Vertical velocity w contours for the nonhydrostatic case. Contour intervals are $0.12\mathrm{ms}^{-1}$, with the zero interval omitted and negative contours dashed.

variables which can be obtained from η. In the evanescent case, a wind velocity maximum and pressure minimum occur over the summit, while in the hydrostatic wave case those features occur over the lee slope. A net drag is produced on the mountain in the hydrostatic case from a pressure difference across the mountain. This drag D can be computed as either the horizontal pressure force on the mountain h or the vertical flux of horizontal momentum in the wave motion (Smith, 1979):

$$D = \int_{-\infty}^{\infty} p'(x, z = 0)\frac{dh}{dx}dx = \overline{\rho}\int_{-\infty}^{\infty} uwdx \tag{1.23}$$

When the bell-shaped mountain is used as the lower boundary, the drag per unit length is:

$$D = \frac{\pi}{4}\rho_0 N U h_m^2 \tag{1.24}$$

This momentum flux across a horizontal level is constant with height (Wurtele et al., 2002), and so there is no contribution to the mean flow acceleration until a point is reached at which the gravity wave breaks down (this can be far away from the mountain source). This result concerning wave drag is a central part of many first-generation gravity wave drag parameterization schemes used by global weather models (Kim et al., 2002). In these early parameterization schemes, the mountain wave drag, calculated at the surface, would then be transferred upwards and deposited in regions where the mountain wave was assumed to become unstable (perhaps from a critical level or density variations with height). Global weather models were found to forecast the stratospheric polar night jet and the subtropical jet with more accuracy after the inclusion of this parameterization scheme which would typically introduce drag in the lower stratosphere.

Linear theory has also been applied for instances of a vertically varying background atmospheric profile. (Scorer, 1949) showed that trapped lee waves are possible when l^2 decreases with height. Trapped waves occur when vertically propagating wave modes encounter an atmospheric layer where the atmosphere's natural frequency (N) is lower than that of the gravity wave mode. In this case, the gravity waves are reflected back downwards, resulting in a propagation horizontally in the atmospheric layer that can support the waves. Lee waves occur when N decreases with height or U increases with height, and considering that in the lower atmosphere wind speeds generally increase with height, partial trapping of the wavefield is not uncommon. There also can be instances when the smaller wavelengths of a wave field are reflected, while larger wavelengths continue to propagate upwards. The process in which larger wavelengths continue through the partially-reflecting layer is known as wave ducting. Trapped waves are also characteristically non-hydrostatic. A mathematical derivation of trapped waves is beyond the scope of this dissertation though a satellite image of trapped waves as seen by the clouds over Virginia is shown in Fig. 1.4. The lee waves are generated over the Appalachians and propagate horizontally towards the southeast over the Chesapeake Bay.

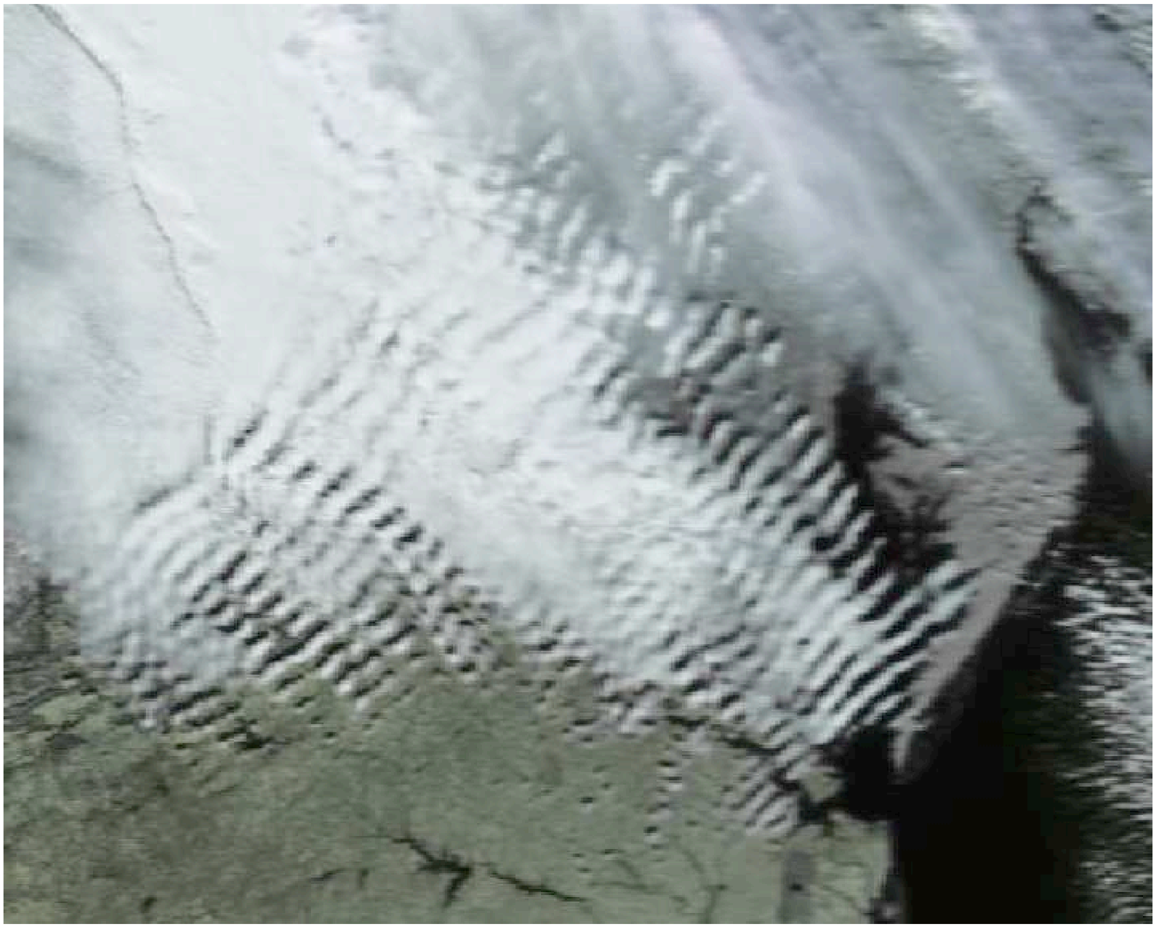

Figure 1.4: High resolution image of a trapped lee wave field on January 27, 2007 from a high resolution NOAA POES satellite. Gravity waves originating over the Allegheny Mountains in West Virginia can be seen as far as over the Chesapeake Bay in southeast Virginia (from the Center for Earth Observing and Space Research, George Mason University).

The critical layer is another phenomena which affects gravity waves and has been successfully explained in terms of linear theory (Bretherton, 1966; Booker and Bretherton, 1967). Although we do not investigate effects of critical layers on wavefields, a brief definition is presented here as internally-generated internal critical layers are evident in a few of the results presented in chapter 4. In the vicinity of a critical layer, the background wind U decreases with height so that a vertical propagation of a gravity wave field through the layer is not possible. The behavior of a wavefield as it interacts with a critical layer has been characterized by its effective Richardson number Ri, which is the ratio of atmospheric stability to vertical wind shear. The critical level, located within the critical layer, can be diagnosed from Eqn. (1.12) (the dispersion relation for mountain waves) $\hat{\omega} = \overline{U}(z)k$ where $\overline{U}(z) = 0$. At this level, the intrinsic frequency $\hat{\omega}$ approaches zero. As $\overline{U}(z) \rightarrow 0$, the vertical wavelength and vertical group velocity component of a wave packet approaches zero (Bretherton, 1966). The wave packet theoretically takes an infinite amount of time to reach the critical level.

Booker and Bretherton (1967) use linear theory to show that the vertical wave number and horizontal perturbation velocity approach infinity at the critical level, and wave momentum and energy transfer occur below the critical level. For $Ri > 1$ the gravity wave is almost completely absorbed into the mean flow, a process which does not include turbulence or dissipation. When $1 > Ri > 1/4$, absorption is attenuated as partial reflection occurs (reflection increases with decreasing Ri). Grubisic and Smolarkiewicz (1997) confirm the linear predictions with a nonlinear, anelastic nonhydrostatic model for gravity waves with sufficiently small amplitude perturbations and critical layers where $Ri > 1/4$. Good agreement is found everywhere except in the vicinity of the critical level due to numerical finite-difference approximations of viscosity. When Ri is between 1/4 and 1, the range at which linear theory remains valid becomes very limited as the gravity wave perturbations in the flow must be sufficiently small so that wave-induced nonlinearities do not occur. In the non-linear critical level regime, where either the wave amplitudes are sufficiently large or the critical layer contains strong background vertical shear so that Ri locally becomes less than 1/4, nonlinear effects such as wave breaking renders linear theory invalid. For local Richardson numbers of less than 0.25, 'over-reflection' can occur, where the reflecting wave draws energy from the background atmosphere (Clark and Peltier, 1977).

Linear methods have proved to be very useful in our understanding of mountain wave phenomena and various applications such as parameterization schemes and drag estimates.

However, the central assumption in linear theory that the wave perturbation is small compared to the mean state horizontal velocity (i.e. $|u| << |\overline{u}|$), does not always accurately reflect flow regimes in mountainous regions. In the next section, ongoing research into such nonlinear flow regimes are examined.

1.4 Nonlinear Orographic Flows

In linear theory, the Fr_h is assumed to be greater than 1. When Fr_h is close to or less than unity, nonlinear effects in the flow must be considered. To physically understand these nonlinear processes, consider the Froude number definition: $Fr_h = U/(Nh_m)$. Assuming an average tropospheric N value of 0.01s^{-1}, when $Fr < 1$ either the mountain is sufficiently tall or the upstream wind speed is weak so that the upstream flow does not have the kinetic energy to ascend the mountain. For a relatively small mountain of $h_m = 1$km, a horizontal wind speed of 5ms^{-1} means $Fr_h = 0.5$, which suggests the low-level upstream flow is not passing over the mountain (i.e. see Hunt et al. (2001)).

The response of the upstream flow to a sufficiently tall mountain has been of considerable interest to the atmospheric science community for the last half century. Global weather model parameterization schemes and dispersion models must account for low Froude number flows in mountainous regions. An often-applied theory to these flows regimes is known as Sheppard's formula (Sheppard, 1956; Hunt and Snyder, 1980), which is derived from simple energy arguments concerning whether an upstream parcel at a particular height will have sufficient kinetic energy to ascend a mountain. If this is not the case for air parcels below a height z_c, the air parcel is assumed to be diverted around the mountain (this is also referred to as flow splitting). In the case of a uniform atmosphere, Sheppard's formula is expressed as:

$$\frac{z_c}{h} = 1 - Fr_h. \tag{1.25}$$

z_c is referred to as the dividing streamline height, or the upstream height at which an air parcel has sufficient energy to ascend a mountain. It can be seen from the equation that z_c is dependent on Fr_h. As Fr_h decreases, z_c increases with respect to the height of the mountain. In any instance where $Fr_h < 1$, if we substitute the mountain height h for $h - z_c$ (the maximum actual height that an upstream air parcel ascends) in the Froude number definition, the *effective* Froude number for the gravity wave-contributing component of the flow will always be unity.

A shortcoming of Sheppard's formula is that it does not account for drag or pressure accelerations (Trombetti and Tampieri, 1987). A modified form of Eqn. (1.25) includes these forces:

$$\frac{z_c}{h} = 1 - \alpha Fr_h, \tag{1.26}$$

where α modifies the height of z_c in relation to Fr_h. When $\alpha > 1$ pressure accelerates the flow so that z_c is raised. When $\alpha < 1$ internal drag slows the flow, so that z_c is lowered. Dividing streamline theory has held up to many laboratory tank simulations and model simulations. Snyder et al. (1985) test Sheppard's formula and find good agreement for numerous tank experiments with axisymmetric hills and density gradients. Numerical simulations by Ding et al. (2003) support Snyder et al. (1985), and theorize that pressure accelerations and internal drag affect the flow, but are of roughly equal magnitude and therefore cancel each other out. However, field experiments and numerical simulations of atmospheric simulations generally put the value of α to be in the 0.5 to 0.8 range Trombetti and Tampieri (1987).

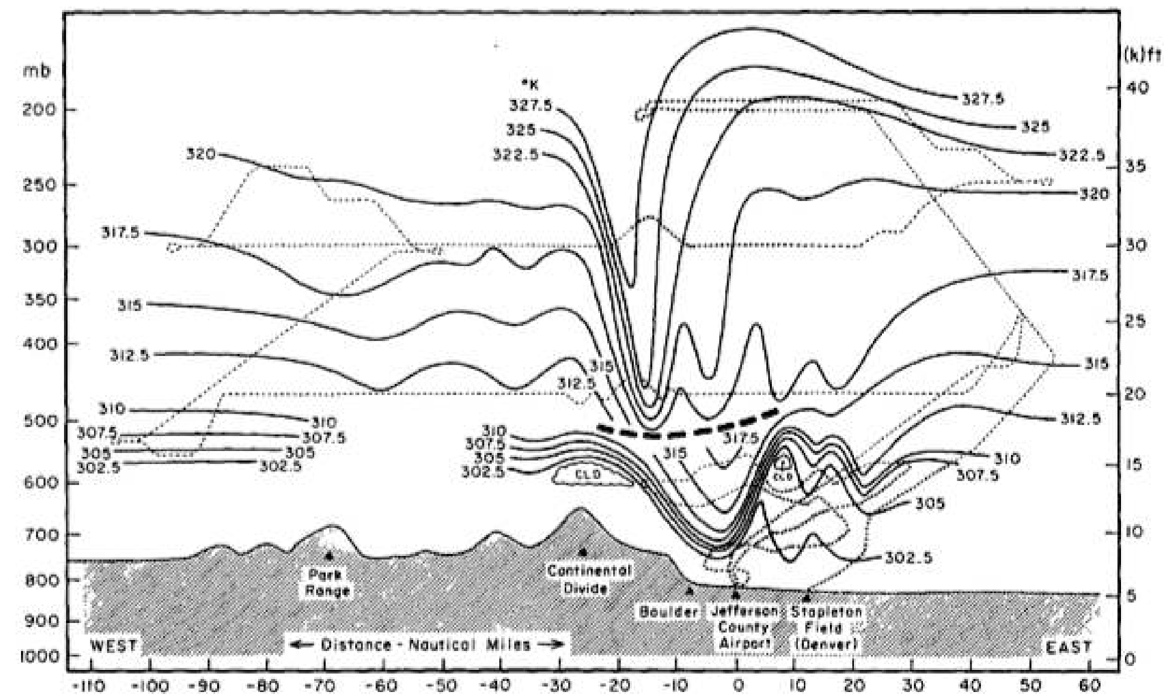

Figure 1.5: The often-referenced Boulder, CO windstorm of 1972, where surface winds on the lee of the front range exceeded $50 \mathrm{ms}^{-1}$ and intensive aircraft turbulence was observed at higher altitudes (from Klemp and Lilly (1975)).

1.4.1 Numerical Experiments

There are many papers devoted to uniform low-Froude number atmospheric flows. Research by Smolarkiewicz and Rotunno (1989a), Miranda and James (1992), and Schär and Durran (1997) all concern a low Froude number flow regime over a bell-shaped ridge. Their research shows that when $Fr \sim 2/3$, the flow is in what can be described as a wave-breaking regime, where significant amounts of TKE is generated by an unstable low level mountain wave breaking over the lee slope of the ridge. This type of flow has been characterized as analogous to a hydraulic jump, as streamlines fall steeply over the ridge before ascending rapidly slightly further downstream. Model results depicting a downslope wind velocity maximum has been cited as being a cause for windstorms. The upstream flow splits around the mountain at the lowest levels while a stagnation point forms on the windward slope, and a small pair of lee vortices are generated. Significant amounts of internal drag associated with the breaking wave and the nonlinear flow around the mountain is also associated with this type of flow regime. These results have been achieved by various researchers with a free-slip lower model boundary, so that surface friction does not play a role. This particular flow regime is extensively studied in section 3.3.

In the above cited numerical simulations, a gradual change occurs in the prominent dynamical forces acting near the mountain as Fr is decreased. For the case when $Fr \sim 1/3$, the lee side vortices are much larger and prominent downstream of the mountain, and more of the upstream flow splits around the mountain. Upstream flow blocking is also more pronounced, and flow stagnation and upwards propagating columnar modes have been observed by Pierrehumbert and Wyman (1985) and Smolarkiewicz and Rotunno (1989b). These features are the underlying reason for a phenomena called 'orographic adjustment' Pierrehumbert and Wyman (1985), where upstream flow stagnation leads to upwind ripples in the flow. The upwind flow 'senses' these ripples as a stationary forcing mechanism as parcels are advected over them, generating a weak gravity wave field upstream of the dominant wave train over the mountain. Low level wave breaking and TKE generation is noted over the lee slope, but the intensity is not as strong as when $Fr \sim 2/3$.

A variation on this type of flow was observed in the simulations of Schär and Durran (1997), who simulated lee vortex shedding by introducing an initial asymmetrical potential temperature perturbation on one side of the mountain. An alternating pair of vortices are then advected downstream of the mountain. This feature has been observed in satellite photographs of island mountains. Fig. 1.6 shows such a flow regime, reflected in the low level clouds to the lee of Galapagous island.

The flow approaches a potential flow state as Fr drops below 0.1 Smolarkiewicz and Rotunno (1989a). In this state, there is little gravity wave generation as virtually all of

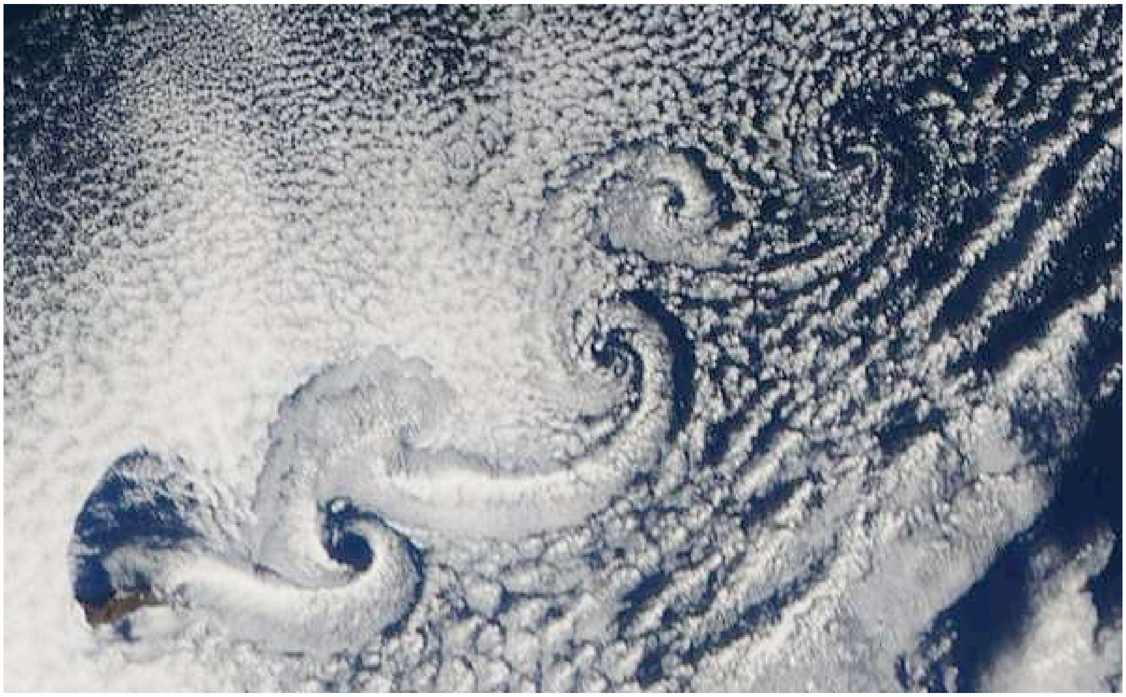

Figure 1.6: NASA MODIS high-resolution satellite image of vortex shedding off of Galapagous island on September 14, 2006. Note that the image has been rotated 90 degrees counter-clockwise so that the north direction is to the left.

the flow is advected around the mountain and does not pass over. It should be noted that all of these studies concentrated on the low level flow field around the mountain, and did not elaborate very much on the wave generation above the mountain. While these studies have contributed much to our understanding of lower level drag caused by upstream flow blocking and downstream lee vortices, much remains to be learned about how the actual wave field is affected by these lower level nonlinear processes. The wave forcing mechanisms in these low Froude number flows is not very well understood, though Sheppard's formula does provide an approximation of how the resulting wave structure might appear like as the divided streamline height field acts as the main gravity wave forcing mechanism.

The low level flow behavior and structure in the vicinity of bell-shaped hills is apparent in papers such as Smolarkiewicz and Rotunno (1989a), Miranda and James (1992), and

Schär and Durran (1997). As the circular hill shape is elongated to resemble more of a two-dimensional ridge, the flow begins to act somewhat differently as it adjusts to the orography. Several researchers including Smolarkiewicz and Rotunno (1989b), Ólafsson and Bougeault (1996), Bauer et al. (2000), and Epifanio and Durran (2001) have examined the flow in the vicinity of a ridge as a function of the horizontal aspect ratio, β, which is the ratio of the ridge half-width in the direction normal to the wind velocity (b) to the half-width along the wind trajectory (a).

Their research shows, that for a given low Froude number flow regime, as β is increased the amount of upstream flow blocking and stagnation increases since more of the flow is diverted around the mountain. The upstream 'ripples' in the flow associated with orographic adjustment become more apparent (Smolarkiewicz and Rotunno, 1989b). As β becomes larger, the ripple is located further upstream of the mountain, and the associated secondary gravity wave's vertical wavelength becomes larger in size. The entire region of upwind flow deceleration also increases as β becomes larger, and upwind propagating columnar modes are more pronounced. Smolarkiewicz and Rotunno (1989b) conjecture that the upwind flow stagnation region can primarily be explained by linear theory as heavier fluid piles-up on the windward side, but that the columnar modes are primarily a result of wave breaking. In the limit of a two dimensional ridge, Pierrehumbert and Wyman (1985) show that the upstream effects eventually reach infinity.

Epifanio and Durran (2001) find that the mountain wave amplitude for a two dimensional ridge is stronger than in any of the elongated ridge cases, as deflection of the low level flow weakens wave amplitude. In the case of an elongated ridge, wave breaking is more pronounced on either side and not in the middle (Ólafsson and Bougeault, 1996), as the maximum extent of upstream flow blocking and negative return flow to the lee suppresses wave generation at the center. As the mountain becomes elongated, a larger amount of the upstream flow is diverted around the ridge. The lee vortex pair becomes wider and moves downstream, with the vortex centers being located about $2b$ downstream of the mountain top and are almost independent of the mountain height Bauer et al. (2000). The amount of surface drag produced in the elongated ridge case is greater than for the circular hill, but not as much as in the two dimensional hill case (Ólafsson and Bougeault, 1996; Epifanio and Durran, 2001).

Numerical simulations of critical layers have found that nonlinear processes are often very important as vertically propagating waves interact with the layer. Clark and Peltier (1977), and Peltier and Clark (1979), and Peltier and Clark (1983), find that topographically forced gravity wave breaking effectively generate an 'internal' critical layer, where the isentropes overturn locally and the wave in the underlying region becomes amplified to have an intensity in excess to that predicted by linear theory. Clark and Peltier (1984) include an external critical layer in their background flow and note that for a mountain generating waves with sufficient amplitudes, reflection and over-reflection due to convective instabilities occur. This happens even though the gradient Richardson number of the external critical layer may exceed 0.25. The local Richardson number, in the vicinity of the gravity waves, is often less than 0.25 as gravity wave-induced wind and stability gradients affect the critical layer. It is also noted that the placement of the external critical layer at certain distances above the mountain lead to constructive wave interference between the upward propagating and reflecting wave modes (Clark and Peltier, 1984). At these levels, high drag states are generated along with wavebreaking, and downslope wind storms occur. Wave amplification is much reduced when the critical layer is not on one of the resonant levels.

Other studies of external critical layers in mountainous flows have been conducted by Bacmeister and Pierrehumbert (1988), Durran and Klemp (1987), and Wang and Lin (1999). These papers primarily focus on non-linear interactions between the mountain waves and the environmental critical layer, and compare results from Clark and Peltier (1984) and hydraulic theory for hydrostatic mountain waves (Smith, 1985), which implicitly assumes a critical level as its upper boundary condition. Numerical simulations generally support the theories of Clark and Peltier (1984) and Smith (1985) for predicting the resonant levels for high drag states and downslope wind storms. Bacmeister and Pierrehumbert (1988) note that the predictions of Smith were not very much affected by nonhydrostatic mountain waves.

1.4.2 Field Experiments

Much recent effort into the understanding of gravity wave generation and propagation has been motivated by several field experiments such as the Fronts and Atlantic Storm-Track Experiment (FASTEX) (Doyle et al., 2004), the Seirra Rotor Project (SRP) (Jiang et al., 2007), the Pyrenees Experiment (PYREX) (Bougeault et al., 1990, 1997), and particularly the Mesoscale Alpine Experiment (MAP) (Smith et al., 2002; Doyle and Smith, 2003; Volkert et al., 2003; Jiang and Doyle, 2004; Jiang et al., 2005; Smith et al., 2007). One of the principal objectives of the MAP experiment was to understand 3D bravity wave breaking and wave drag for better parameterizations of gravity wave effects in global weather models. There were seven well-documented gravity wave events in the MAP field campaign, of which (Smith et al., 2007) note that "...it is clear that any quantitative prediction of mountain wave generation must take full account of these lower tropospheric processes..." In particular, lower tropospheric processes such as low-level wind shear, upstream blocking, a slow-moving stagnant boundary layer, and latent heat release are found to affect mountain wave generation and propagation.

The first field experiment to document a wave-breaking event in detail was the Boulder, CO windstorm of 1972. The windstorm was part of an intense nonlinear flow regime over the Rocky Mountains. The ridge, located near Boulder, is longitudinally-oriented and extends for about 500km. The across-ridge length is about 50km, and the ridge peak is about 2km above the plains. A large breaking mountain wave was observed throughout the troposphere by surface and aircraft observations, which had a horizontal wavelength of $50-100$km. The downslope windstorm wind speeds were observed to be in excess of 50ms^{-1}, along with intense regions of TKE which also was found in the region of the breaking wave. The horizontal wind speed in the breaking wave reversed direction from upstream values of 40ms^{-1}. A schematic of the windstorm from Klemp and Lilly (1975) is shown in Fig. 1.5. Potential temperature contours are shown, which give an indication of the airflow as it descends rapidly over the Continental Divide, and then shoots back up over Boulder. The maximum wind velocity occurs in the region of tightly packed contours over the Continental Divide and Boulder, while the stagnant and reversed u region is located in the region of the rapidly ascending isentropes at $30-35$kft. Significant TKE is located in the region of the ascending isentropes aloft, as well as closer to the surface downstream of Boulder.

The Boulder, CO windstorm has been the subject of many numerical experiments (Klemp and Lilly, 1975; Clark and Peltier, 1977; Peltier and Clark, 1979; Peltier and Clark, 1983; Clark and Farley, 1984; Durran, 1986; Doyle et al., 2000) and a motivation for the hydraulic jump description derived by Smith (1985). This experiment also helped establish the relationship between wave breaking aloft and the surface downslope windstorm, though there has been some debate as to the mechanisms behind the windstorm such as hydraulic theory (Smith, 1985), downward reflection of wave energy Klemp and Lilly (1975), and downward reflection from the internal critical level (Clark and Peltier, 1977; Peltier and Clark, 1979). Doyle et al. (2000) conducted a numerical experiment for this particular case with identical simulations from 11 different nonhydrostatic models. While all the models predicted the upper-level wave breaking that occurred during that case, the wave breaking structure as predicted by the models was very sensitive to numerical dissipation, numerical representation of the horizontal advection, and lateral boundary conditions.

A similar wave breaking and surface downslope windstorm case was observed over the east coast of Greenland during the FASTEX experiment. Doyle et al. (2004) was able to run accurate simulations of the case with high resolution runs with the nonlinear and nonhydrostatic COAMPS (Coupled Ocean Atmospheric Mesoscale Prediction System) numerical model. Potential temperature perturbations of 25K were observed along with w speeds of up to 10ms^{-1} and a near-zero horizontal velocity region in the vicinity of the breaking wave.

Large-amplitude breaking waves over large ridges were observed in the Boulder, CO and FASTEX field experiments, though wave activity in the PYREX and MAP experiments were much more limited. The primary objectives of the PYREX field experiment was to measure the mountain pressure drag, the wave momentum flux, and any TKE in the mountain wave fields (Bougeault et al., 1997). Another objective was to understand the low level flow field around the Pyrenees to better predict mountain wind storms common to the area. With the Pyrenees having a height of around 3km and a length of 400km oriented roughly east-to-west, they also hoped to gain an understanding to what extent the deceleration of the lower level flow affects the synoptic-scale flow. To achieve these goals, surface observations, sodars, and soundings were coordinated with observations from multiple aircraft simultaneously flying at different height levels. Perhaps the most surprising of their findings was that no tropospheric wave breaking was observed, despite predictions of such events by mesoscale models for typically low Froude number flow regimes. The flow was also found to diverge around the mountains rather than flow over them, thereby weakening gravity wave forcing mechanisms. In addition, surface pressure drag and the divided streamline height estimates were found to be reasonably accurate, despite the complex geometry or the orography and the nonlinear nature of the lower atmospheric flow.

The MAP experiment was similar to PYREX, but on a much larger scale (Smith et al., 2007). Detailed observational events of mountain wave fields from coordinated observations by aircraft, lidars, balloons, and wind profiles allowed for a detailed picture of lower atmospheric processes affecting wave generation. MAP took place in the Alps, which like the

Pyrenees, is a tall and broad mountain range oriented laterally that often induces highly nonlinear flows. The Alps have a complex geometry - there are many steep valleys and peaks, and so high-resolution three dimensional modeling was thought to be essential in accurately capturing the flow processes and wave fields. In this sense, the MAP field experiment was the first field campaign to capture a detailed picture of the lower atmospheric wave generation region as well as the wave field in a highly nonlinear three-dimensional orographic setting (Smith et al., 2007). In a sense, some of the key findings in the PYREX experiment such as the lack of breaking wave events could be explained with the detailed observations and numerical experiments of MAP.

There exists much literature based on findings from MAP - key findings relevant to the dissertation are discussed here. For an excellent overview of the MAP experiment in its entirety, we refer the reader to issue 133 (year 2007) of the Quarterly Journal of the Royal Meteorological Society, which contains summaries of all the major research pursued in MAP.

As previously mentioned, MAP allowed researchers to examine lower atmospheric atmospheric processes in detail. Flow blocking and stagnant boundary layers were found to be a common feature in the Alps. In one case over Mont Blanc, Smith et al. (2002) observed a remarkably stationary and small amplitude wave field. Given the background atmospheric profile, they found that linear theory incorrectly predicted a trapped wave event (an evanescent layer was located above the tropopause), when in fact no lee waves were observed. It was theorized that the relatively stagnant boundary layer was absorbing the downward-reflecting waves. The stagnant region also had the effect of reducing the effective height of the mountains - which explained the reduced wave amplitude. Despite the steady wave field, the wave momentum flux was found to be variable. Smith and Broad (2003) attribute this to increasing vertical wind shear throughout the day and the reflection of momentum flux in the opposite direction due to the trapping region.

More work on flow blocking was done by Jaubert and Stein (2003) in their analysis of a strong fohn event. The flow regime during the fohn changed from flow splitting around the Alps to flow partially going over the Alps. Wave generation was enhanced, and wave breaking and hydraulic jumps were observed with the fohn. Similar fohn events were also observed and modeled by Jiang and Doyle (2004) and Volkert et al. (2003).

Hydraulic jumps associated with external critical layers were observed by Jiang and Doyle (2004) and Doyle and Jiang (2006). In these cases background flow turning and weakening aloft caused the flow in the lower troposphere to accelerate over the mountains and then 'spill' over the downwind slope, creating a downslope windstorm. The flow was also observed to decelerate further downstream and jump upwards, resembling a hydraulic jump. Jiang and Doyle (2004) observed maximum w magnitudes around $9\mathrm{ms}^{-1}$ and maximum TKE magnitudes of around $10\mathrm{m}^2\mathrm{s}^2$.

Latent heat release was also found to have an impact on gravity wave generation in MAP by Doyle and Smith (2003), who performed a series of numerical simulations with and without the effects of latent heat release. In one particular case where trapped waves were observed, model simulations showed that latent heat release was essential for lee wave ducting. Latent heat release associated with orographic and synoptic scale induced precipitation decreased the stability aloft, causing wave reflection. A downslope windstorm also observed that day was also found to be enhanced by latent heat release.

Numerical modeling played an essential part in the MAP field campaign for understanding the various physical processes involved in the cases where gravity waves were observed. In the Mont Blanc case (Smith et al., 2002; Smith and Broad, 2003) mesoscale models initially incorrectly predicted a trapped wave response because the stagnant boundary layer which muted the downwards reflecting waves was under-represented. For a number of gravity wave events in MAP, the dominant wave signature in the horizontal wavelength was found to be in the range of $3 - 15$km. Since 6 to 8 grid points are generally considered adequate to resolve a wavelength (Smith et al., 2007), model simulations have been very sensitive to their horizontal resolutions. As previously mentioned, model-predicted surface drag effects were found to be dependent on the models' ability to resolve peaks and valleys, which had a major impact on the model predicting whether air currents would flow over or go around a mountain. The ability of the models to predict the gravity waves also depended on whether the observed wave fields were stationary or non-stationary (Smith et al., 2007). Mesoscale models are much better at reproducing observations of stationary wave fields.

This explanation of nonlinear and linear flow regimes in mountainous regions is by no means complete, but provides sufficient background material for my dissertation. The general research area is very broad and intersects many other research interests such as precipitation, multi-scale weather modeling, Coriolis effects, and boundary layer meteorology (to name just a few), so a narrowing of the range of topics is necessary to obtain a handle on the fundamental dynamical processes at work. In the next section, the major research focus of this dissertation is explained in more detail.

1.5 Focus of Research and Methodology

Understanding mountainous flows and wave generation and propagation in nonlinear flow regimes is essential for effective parameterization schemes. It is particularly helpful to know to what extent nonlinear flow regimes can be predicted by linear theory. While nonlinear flows usually require complex modeling efforts to understand flow response to a type of forcing, we showed in section 1.3 that many linear gravity wave processes can be predicted by analytical solutions. The use of analytical solutions can render information about flows virtually instantly or in a short amount of time, while nonlinear numerical models solving complex flow fields often require a time scale which precludes their use operationally (though improvements in computer technology are continuously enabling nonlinear simulations of increasing complexity). Global weather model parameterization schemes for mountain waves are likely to be used for at least the next few decades as their current typical horizontal resolutions ($\sim$ 50km) are inadequate for gravity wave spatial scales which sometimes are no larger than 5km (Kim et al., 2002). Similarly, some of the lower atmospheric nonlinear processes which affect gravity wave generation and propagation occur at these small scales.

Fully capturing a mountain wave field generated in a nonlinear flow regime requires high resolution nonlinear modeling. Many of the recent studies of these types of flows apply high-resolution numerical meteorological models, as this dissertation does. The Weather, Research, and Forecasting (WRF) model, developed at the National Center for Atmospheric Research (NCAR) in Boulder, Colorado, will be the primary numerical model for the dissertation. We will provide a background explanation of this model in great detail in Chapter 2, though for now it should be said that WRF is a fully compressible nonlinear meteorological model in a terrain-following coordinate system. The experiments we conduct require that the terrain is the principal forcing mechanism, and WRF is well suited for this type of simulation due to its terrain-following lower boundary. Initially, only simple idealized bell-shaped circular mountains are studied in order to simplify the problem as much as possible. We will, however, explore some complex orographic terrain later in this dissertation.

In addition to the non-linear WRF model, a linearized semi-analytical model has also proved to be an essential research component. The Fourier Transform (FT) method, developed at the Naval Research Laboratory (NRL) in Washington, DC, provides nonhydrostatic linear wave solutions which can be compared directly to the corresponding WRF solutions. By analyzing results from these two different models, we can see to what extent nonlinear solutions can be approximated with a linear solution. A primarily goal of this research is to find a range of circumstances in which nonlinear flows can be predicted by linear theory. These results might then be applied to parameterization schemes for geographic regions where tall mountains or weak stability gradients often ensure that the lower atmospheric flow is at least moderately nonlinear.

In addition to ascertaining the linearity of a wave field, another main goal of this dissertation is to employ novel ways to initialize the linear FT model for accurately capturing the wave field in nonlinear flow regimes. As was explained in section 1.3, linear analytical models are often initialized with a surface (or lower boundary) vertical displacement field which is assumed to be the orography. While this assumption provides reasonable solutions in high Froude number flow regimes, for low Froude number flows the low-level flow can be significantly influenced by the orography, which in turn affects mountain wave generation and propagation. Thus, the use of orography might not always be the best way to initialize a linear model for predicting wave fields.

The alternative FT initialization method is to initialize FT with the WRF w field at a specified height above the mountain. The gravity wave solution is then obtained at heights both above and below the level of initialization. We can then compare corresponding WRF and FT results to assess the linearity of the wave field. Similar results between the WRF and FT models would indicate that the gravity wave field can be approximated by linear theory, and that corresponding linear predictions such as the momentum flux are applicable.

In addition to capturing the wave field in a nonlinear flow regime, we can then use the w-initialized FT model to obtain the vertical displacement field at the lower boundary. Of course, in this particular case, the 'lower boundary' is somewhat arbitrary as the vertical displacement field can be calculated at any height. We decided to place the lower boundary at the critical dividing streamline height (section 1.4), as any upstream air parcels originating below this height are diverted around the mountain and theoretically do not affect wave generation (as they do not oscillate vertically).

As was the case for section 1.3 of this chapter, we will be describing and visualizing the gravity wave field primarily in terms of the vertical velocity w. Virtually all of the research articles examined in this chapter have used w for this very purpose, and so it is convenient should the reader wish to peruse those papers. In addition, it lends itself well to the physical description of buoyancy-related processes in terms of vertical oscillations in an otherwise horizontally-homogeneous flow field. The lower atmospheric flow distortion phenomena can well be visualized with other physical meteorological variables and streamlines, so those are used when deemed appropriate.

A uniform atmosphere is chosen as the background atmospheric profile for the current research here. Eventually we would like to graduate to more realistic atmospheric profiles to observe the effects of wave trapping, critical layers, boundary layer flows, etc on the lower level flow distortion and gravity wave fields, but such effects introduce a level of complexity which will be very difficult to understand if the more basic issue of the flow response in a uniform atmosphere is not resolved.

In summary, the research for this dissertation has two primary objectives: (1) improve the initialization scheme of FT using horizontal cross-sections of w from WRF, and (2) examine the impact of nonlinear flows over complex orography on mountain wave momentum flux estimates calculated from both FT initialization methods. In the following chapter, descriptions of the WRF and FT models are given. To ensure their ability to accurately predict the gravity wave field, results from both WRF and FT are then compared to the analytical solutions presented in section 1.3. The WRF and FT models are then applied to a nonlinear flow regimes around simple bell-shaped obstacles in Chapter 3. This analysis will be extended to include cases with complex orography in Chapter 4, which focuses on a cases using the terrain of Hawaii's Big Island. Hawaii, with two volcanic mountains over 4000m over an area not adequately resolved by most global weather models, is ideally suited for studying smaller scale nonlinear flows generated by the upstream flow's interaction with the orography. Lastly, chapter 5 highlights the major results and conclusions obtained in this dissertation, and discussions of future work pertaining to this research are presented there.

Chapter 2: Discussion of the WRF and FT Models

Much of the research in this dissertation is carried out with the Weather, Research, and Forecasting (WRF) model and the Fourier Transform (FT) model. WRF is a fully compressible nonlinear mesoscale meteorological model and FT is a semi-analytical linear wavefield model. Both are ideally suited for modeling terrain-generated gravity waves. A detailed description of both models is given in this chapter, and we will compare corresponding results from both models with the analytical benchmark linear wave solution provided in section 1.3. The new FT initialization method is also discussed.

2.1 The Weather, Research, and Forecasting Model

The Weather, Research, and Forecasting (WRF) model is a mesoscale meteorological model developed at the National Center for Atmospheric Research (NCAR), and is intended for both meteorological forecasts and idealized research. WRF has been chosen for this dissertation research primarily for its applicability to idealized orographic flow simulations. Additionally, WRF has a large and active research community and it updated on a fairly regular basis, which is beneficial for user support. Following is an explanation of WRF as is applied for my research. A detailed explanation of WRF including the governing equations and numerical methods is presented in Appendix A of this dissertation.

2.1.1 Overview of WRF

A fully compressible and non-hydrostatic model, WRF integrates the Euler equations of motion. Prognostic equations are solved for the u and v cartesian velocity components, the vertical velocity w, the perturbation potential temperature θ, perturbation geopotential, and the surface pressure for dry air. A prognostic equation is also solved for turbulent kinetic energy (TKE), as part of the 1.5 order turbulent closure scheme. WRF filters noise and acoustics with divergence damping, external-mode filtering, and a vertically implicit acoustic step off-centering scheme (Skamarock et al., 2005).

The prognostic variables are discretized on an Arakawa-C staggered grid, where u, v, and w are spaced half grid point away from the center in the x, y, and z directions, respectively. Scalar variables and TKE are solved in the center of the grid, and the geopotential is solved on the w points. WRF employs 5th order horizontal advection and 3rd order vertical advection, which allow for higher order accuracy while taking advantage of the scheme's inherently diffusive nature. TKE and scalar variables employ a positive definite advection scheme. The vertical coordinate is terrain-following mass (pressure) based, and the vertical grid is stretched in the Cartesian z direction. A third order Runge-Kutta time step is used, with six smaller timesteps for acoustic and gravity wave modes.

We conduct our research with the idealized WRF model, and our simulations employ radiative lateral boundaries, a free-slip (frictionless) lower boundary, and a rigid lid for the upper boundary. A Rayleigh damping sponge layer absorbs gravity waves in the upper half of the model domain. WRF is initialized with a uniform atmosphere with no moisture and the Coriolis term set to zero. The orography is specified depending on the simulation.

2.1.2 Initializing the WRF Model

The WRF model is initialized with a 1D sounding profile for the idealized experiments. It is assumed that initially, the flow varies in the vertical direction only, and is horizontally homogeneous. Thus, the atmosphere is initially in a steady state, and the orography provides the forcing. This initial steady state is referred to as the 'background flow' or 'reference state'. The 1D profile consists of the potential temperature, and the u and v

horizontal wind components. As will be explained below, the model then calculates the other thermodynamic variables such as pressure and density so that the initial state is in hydrostatic equilibrium.

The reference state is calculated after WRF reads in θ, u, and v from the 1D profile, and then a full state that includes moisture is calculated for the initial conditions in the model. However, that is not relevant within the context of this dissertation as none of the simulations contain water vapor. The equations below do not include water vapor, though they can be generalized to include moisture.

After the 1D profile is read-in by WRF, density is calculated at the sounding levels by integrating the hydrostatic equation up the column using the surface pressure (given a standard value of 1000mB as a lower boundary condition). The hydrostatic equation is

$$\frac{\delta p}{\delta z} = -\overline{\rho}^{z} \tag{2.1}$$

where $\overline{\rho}^{z}$ is an average value of density between the two pressure levels, and $\delta p/\delta z$ is the vertical pressure difference between the input sounding levels. To close Eqn. (2.1), the equation of state is used:

$$\alpha = \frac{1}{\rho} = \frac{R_d \theta}{p_0} \left(\frac{p}{p_0} \right)^{-\frac{c_v}{c_p}}, \tag{2.2}$$

where θ is from the input sounding. Eqns (2.1) and (2.2) form a coupled set nonlinear equations for pressure and density, and are solved by iteration. The pressure at the model top (which corresponds with the height of the model top given in the 'namelist.input' file) is interpolated from the calculated 1D pressure profile. The column mass μ can then be diagnostically calculated from pressure. The potential temperature used in WRF is interpolated to the pressure levels from the initial values of the 1D profile. Density also has to be interpolated to the pressure levels. The geopotential ϕ is calculated using the hydrostatic relation

$$\frac{\delta\phi}{\delta\eta} = -\alpha\mu \tag{2.3}$$

When the model is integrated forward in time (after initialization), hydrostatic equilibrium is maintained because inverse density α is calculated from the geopotential equation and pressure is obtained from the equation of state using inverse density and the prognostic potential temperature (Skamarock et al., 2005).

2.2 The Fourier Transform Method

The Fourier Transform model applies a three-dimensional version of the dispersion relation in Eqn. (1.12) to solve linear wavefields in Fourier space, and is then transformed back to physical space. The dispersion relation is written as:

$$m = (k^2 + l^2)^{1/2} \left(\frac{N^2}{\hat{\omega}} - 1 \right), \tag{2.4}$$

where, as before, (k, l, m) is the wavenumber vector, and only stationary waves are considered so that the intrinsic frequency $\hat{\omega} = -k\overline{u} - l\overline{v}$. As outlined in Lindeman et al. (2008), a Fourier transform algorithm is used that only considers a steady-state ($t \rightarrow \infty$) and a uniform background atmosphere where $\overline{u}$, $\overline{v}$, and N are constant. It should be noted that the Fourier Transform method has been applied to cases of background vertical wind shear (Broutman et al., 2003), vertically varying background stability and wind direction (Eckermann et al., 2006a), and transient solutions (Broutman et al., 2006). The research in this dissertation, however, introduces a new Fourier Method initialization scheme and momentum flux calculations.

The vertical velocity field $w(x, y, z)$ is obtained from the vertical eigenfunctions $\tilde{w}(k, l, z)$ by the inverse Fourier transform

$$w(x, y, z) = \int_{-\infty}^{\infty} \int_{-\infty}^{\infty} \tilde{w}(k, l, z) e^{i(kx+ly)} dkdl. \tag{2.5}$$

The vertical eigenfunctions are exponentials, scaled in the anelastic approximation by the inverse square root of the mean density $\overline{\rho}$ values obtained by the WRF model:

$$\tilde{w}(k, l, z) = \tilde{w_o}(k, l) \frac{\overline{\rho}(z)}{\overline{\rho}(z = 0)}. \tag{2.6}$$

where $\tilde{w_o}$ is evaluated at $z = 0$.

Traditionally, linear analytical models are initialized at the lower boundary where the orography h is assumed to be equivalent to the surface vertical displacement, η, so that $\eta(x, y, z = 0) = h(x, y)$. This is converted to w at the surface by $w(x, y, z = 0) = Uh(x, y)$, or for the vertical eigenfunction

$$\tilde{w}(k, l, z) = -i\hat{\omega}\tilde{h}(k, l), \tag{2.7}$$

where $\tilde{h}(k, l)$ is the Fourier transform of $h(x, y)$. We initialize the FT model in this manner, as it is appropriate for high Froude number flows. However, in low Froude number cases which are highly nonlinear, a new method of FT initialization is presently introduced. We introduce a hybrid FT scheme where the FT model is initialized with a horizontal cross-section of the vertical velocity w_{WRF} field from a corresponding WRF simulation. In this method, we show that it is possible to run a WRF simulation of a nonlinear flow around the mountain and obtain an approximately linear wave field above the nonlinear region. When FT is initialized in this manner, the initialization level can be at an arbitrary height, and so FT can be run both upwards and downwards. The initialization of FT is then

$$\tilde{w}(k, l, z_i) = \tilde{w}_{WRF}(k, l, z_i, t_i) \tag{2.8}$$

where z_i is the initialization height and t_i is the initialization time, and $\tilde{w}_{WRF}$ is the horizontal Fourier transform of w_{WRF}.

In the next chapter we explain the reasoning for choosing a particular height level z_i for initializing the FT model. In short, we want to initialize FT in a region where we believe the wave field is behaving in a roughly linear and steady-state fashion. In addition to obtaining the wave field in terms of w at various levels, FT is also capable of transforming back to η at all levels. This is desirable in obtaining a representative surface vertical displacement field when FT is initialized with w_{WRF}. The lower boundary η field is termed 'wave orography' in this dissertation, though as we shall see, this should not be confused with the actual orography.

We also present Fourier Transform phase-averaged wave momentum flux calculations for $\overline{uw}$ and $\overline{vw}$. Since the Fourier-Ray method gives complex solutions, we can take advantage of this to phase-average wave solutions or products of wave solutions. We assume that u, w have the same phase function, as they do for slowly varying, vertically propagating gravity waves. This is primarily accomplished by converting $\tilde{w}$ to $\tilde{u}$ or $\tilde{v}$, and then convert to the physical components of u, v, and w, and lastly use the following equation:

$$\overline{uw} = 0.25(uw^* + u^*w)$$
$$\overline{vw} = 0.25(vw^* + v^*w) \tag{2.9}$$

where u^* and v^* are the complex conjugates of u and v. The wavefield momentum fluxes can be obtained from both Fourier Transform initialization techniques. For clarification purposes FT initialized with the surface vertical displacement field (i.e. orography) will be denoted as FT_o, and the WRF-initialized scheme is FT_w. In the following section, we see how the two FT initialization schemes compare with the linear analytical case presented in section 1.3.2. In the following two chapters, both FT schemes will be applied to nonlinear orographic flow regimes.

The FT model produces wave field solutions on horizontal surfaces, and to obtain vertical cross-sections we simply take vertical slices through multiple horizontal surfaces. A key advantage of FT is that it produces wave field solutions very quickly - thousands of times faster than a mesoscale numerical model such as WRF. Thus, FT can be applied to near instantaneous real-time weather forecasts of the wave field.

2.3 Model Comparisons

It is useful to compare results from identical simulations of the WRF and FT models to ensure they are working properly. We can have better confidence in the results if the models show good agreement. The analytical solutions presented in section 1.3 provide excellent benchmark cases to which both WRF and FT can be compared with, and the hydrostatic wave solution is a commonly used benchmark for mesoscale meteorological models (Durran and Klemp, 1983; Doyle, 2005). All three cases are simulated by the WRF model, but the FT model cannot be compared to the evanescent wave case since we only use it to simulate propagating waves. Results from both FT methods are shown. For the remainder of this dissertation, we specify the traditional Fourier Transform method initialization scheme (orography at $z = 0$) with FT_o. The new initialization approach with w from WRF is denoted as FT_w.

The WRF model is initialized with the isothermal atmosphere specified in section 1.3 for all of the simulations presented in this section, where the ground potential temperature is 288K, and pressure is 1000mB. The WRF simulations are two-dimensional, with radiative lateral boundaries in the x-direction, a free-slip lower boundary, and the sponge layer beginning at 15km extending up to thetop of the domain at 30km. There are 600 vertical levels, amounting to an average vertical grid spacing of about 50m. The orography is the same as that outlined in all three cases of the analytical solution, with the peak being centered halfway along the x-axis.

In the hydrostatic case, $nx = 600$ and $dx = 500$m. WRF was run for 2 hours with 2s time step intervals. For the nonhydrostatic case, $nx = 600$, $dx = 200$m, and WRF was run for 2 hours at 1s intervals. For the evanescent case, $nx = 600$, $dx = 50$m, and WRF is run for 2 hours at 1/2s intervals. The Fourier Transform model is specified in the same way as WRF for both initialization schemes, and FT_w is initialized at a height of 2km, and after 2 hours of WRF simulation time.

The WRF solution of w for the hydrostatic case is shown in Fig. 2.1. The results closely agree with the corresponding analytical solution presented in Fig. 1.2. Two solutions from the FT model are shown in the middle and bottom panels, where FT_o (middle panel) is initialized with the surface vertical displacement and FT_w (bottom panel) is initialized by w from WRF (at the location of the dashed line). In the latter case, the FT model ray-traces the solution both upwards to 15km and downwards to the surface. It is evident from the FT plots that both initialization methods produce a wave field which is very similar to the WRF and analytical solutions.

Fig. 2.2 shows the WRF and both FT solutions for the non-hydrostatic case, which is

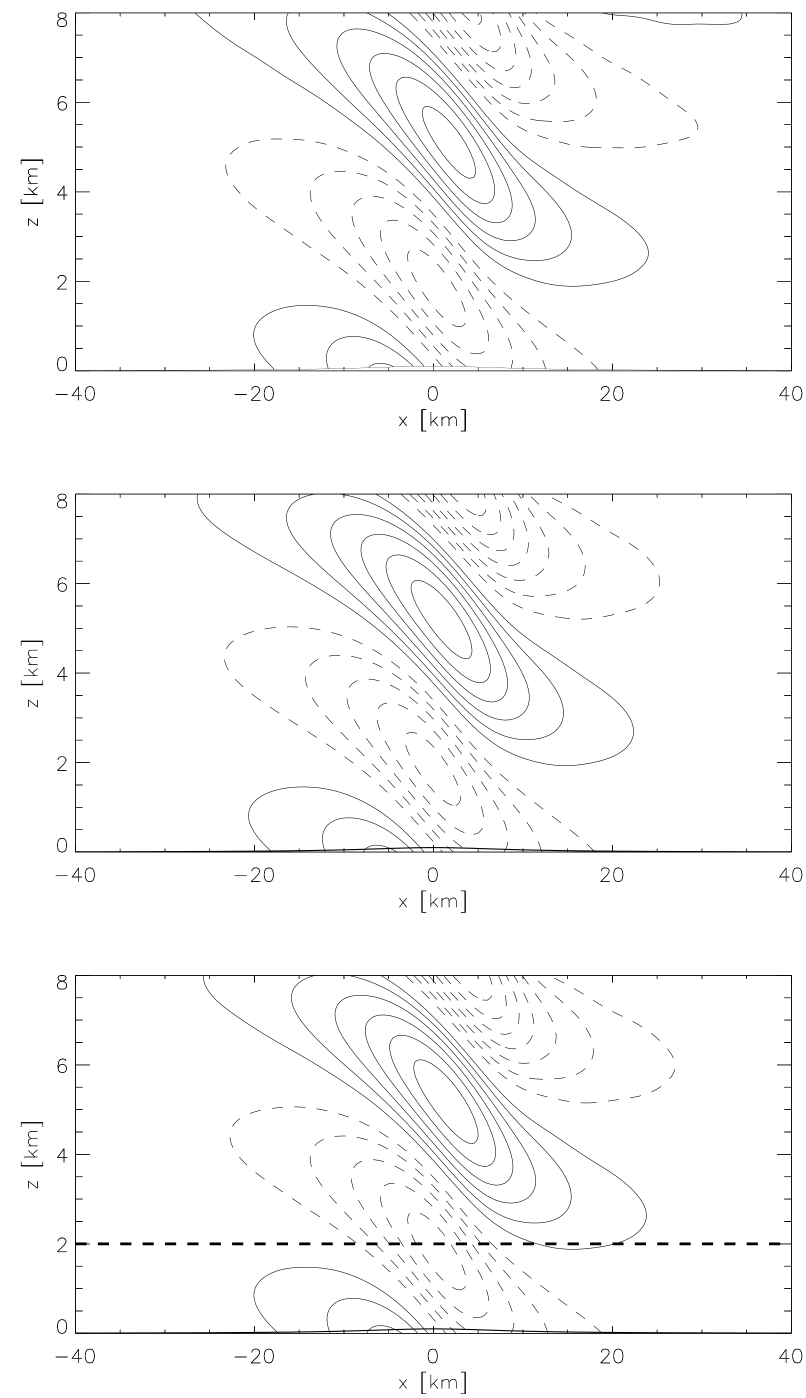

Figure 2.1: Vertical velocity w contours for the hydrostatic case (same as in Fig. 1.2) for WRF (top panel), FT initialized with the surface vertical displacement (middle panel), and FT initialized at 2km by w (dashed line) from WRF (bottom panel). Contour intervals are $0.04\mathrm{ms}^{-1}$, with the zero interval omitted and negative contours dashed.

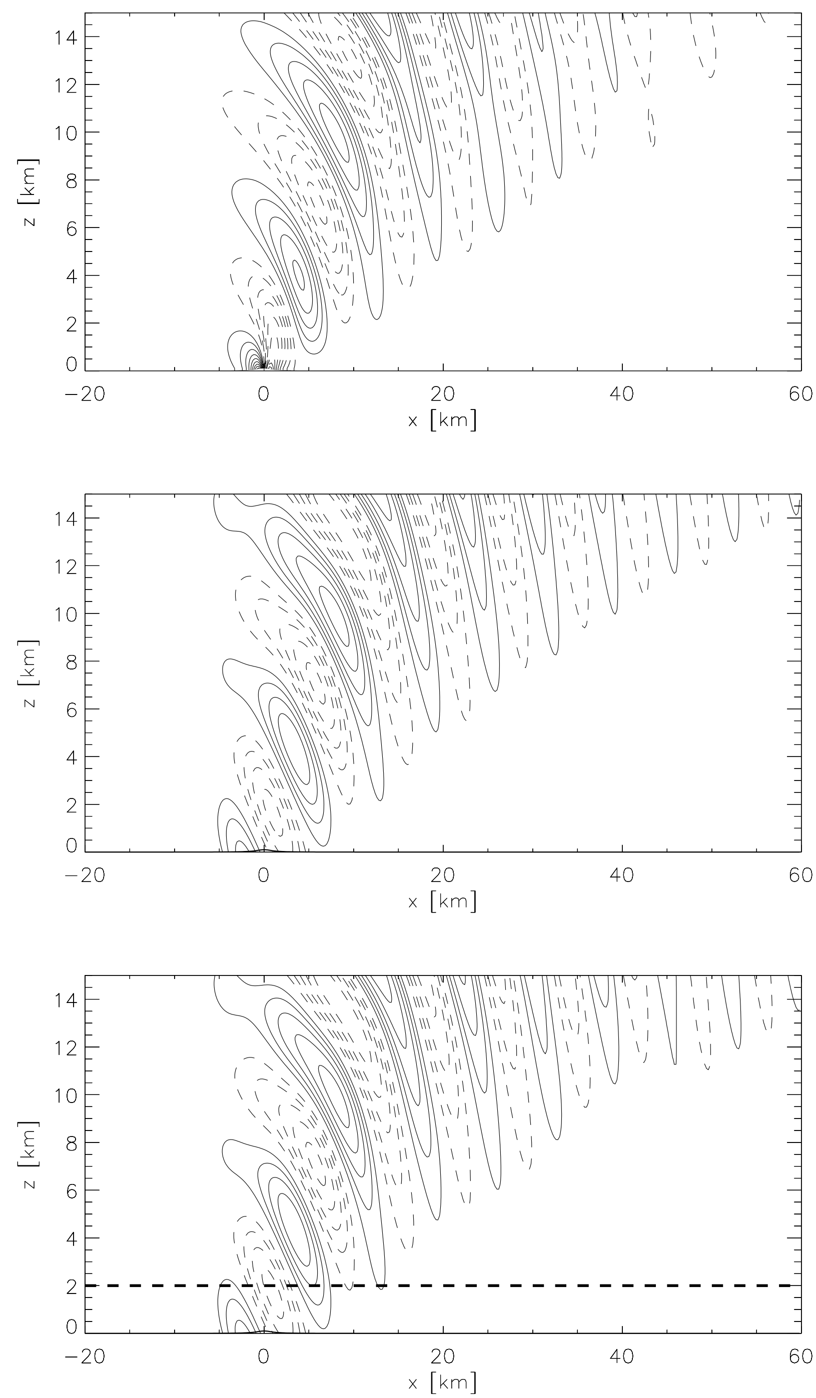

Figure 2.2: Vertical velocity w contours for the nonhydrostatic case (same as in Fig. 1.3) for WRF (top panel), FT initialized with the surface vertical displacement (middle panel), and FT initialized at 2km by w (dashed line) from WRF (bottom panel). Contour intervals are $0.12 \mathrm{ms}^{-1}$, with the zero interval omitted and negative contours dashed.

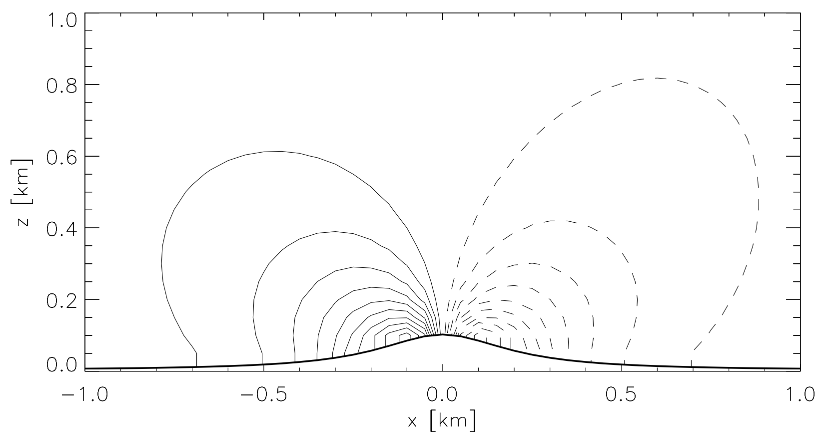

Figure 2.3: WRF w contours for the evanescent case, (same case as the analytical solution in Fig. 1.1). Contour intervals are 0.5ms^{-1}, with the zero interval omitted and negative contours dashed.

comparable to the analytical solution shown in Fig. 1.3. It can be seen that WRF and FT initialized with the surface vertical displacement show reasonably good agreement, though not quite as good as in the previous hydrostatic case. The wave amplitude near the hill is considerably larger in the WRF results than for either FT simulation. This increased amplitude is due to evanescent modes which are important when $al = 1$ (and FT does not account for).

WRF results for the evanescent case is shown in Fig. 2.3. The WRF solution is very similar to its analytical counterpart presented in Fig. 1.1.

The next set of comparisons is for the surface vertical displacement, as obtained by backwards ray-tracing with FT_w. We compare these to the orography, which is taken to be the surface vertical displacement in FT_o. Both the vertical displacement (dashed line) and the orography (solid line) are plotted in Fig. 2.4 for the hydrostatic case (top panel) and non-hydrostatic case (bottom panel). As can be seen in the top panel, the surface vertical displacement line is almost parallel to the orography, though is about 12m lower. We attribute this to numerical errors such as the diffusive nature of the discretized governing

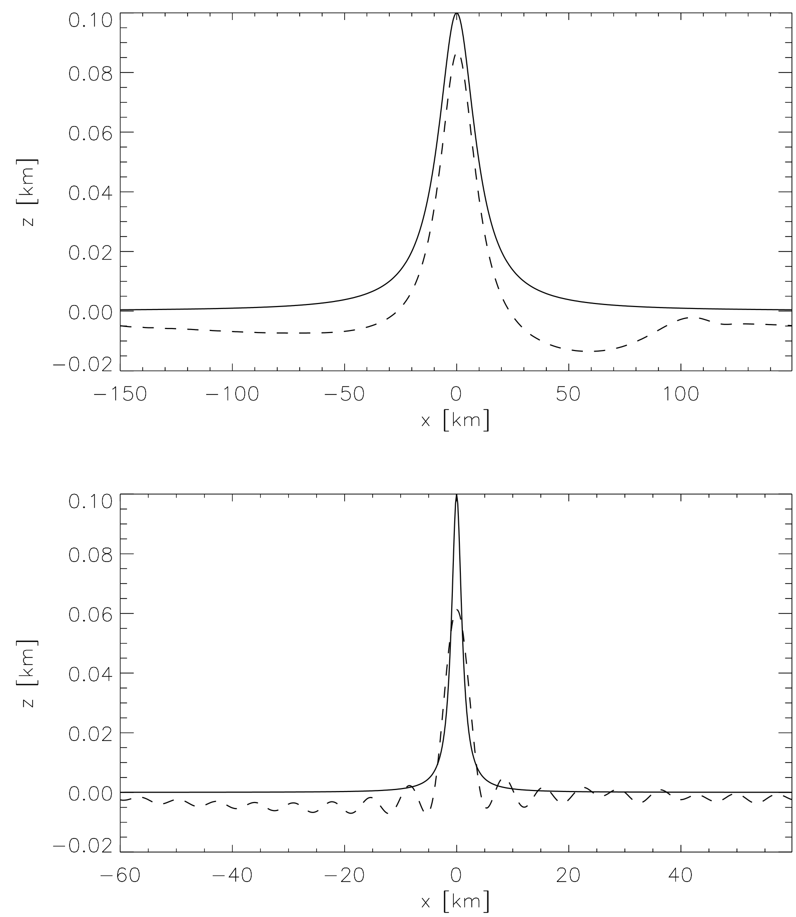

Figure 2.4: The vertical displacement field at the surface ($z = 0$) from FT_w (dashed line) and the orography (solid line) for the hydrostatic case in the top panel, and the non-hydrostatic case in the bottom panel. Note that the Fourier Transform method only applies the non-evanescent wave modes.

equations, or possibly the terrain-following lower boundary of WRF affecting the wave field. Additionally, the Fourier Transform method does not account for evanescent modes which are significant near the orography (particularly in the non-hydrostatic case). For these reasons, the total height change in the surface vertical displacement field predicted by FT_w is less than the mountain height h_m. However, the FT_w surface vertical displacement field is able to accurately reproduce the non-evanescent modes of the wave field (as is shown in Fig. 2.2).

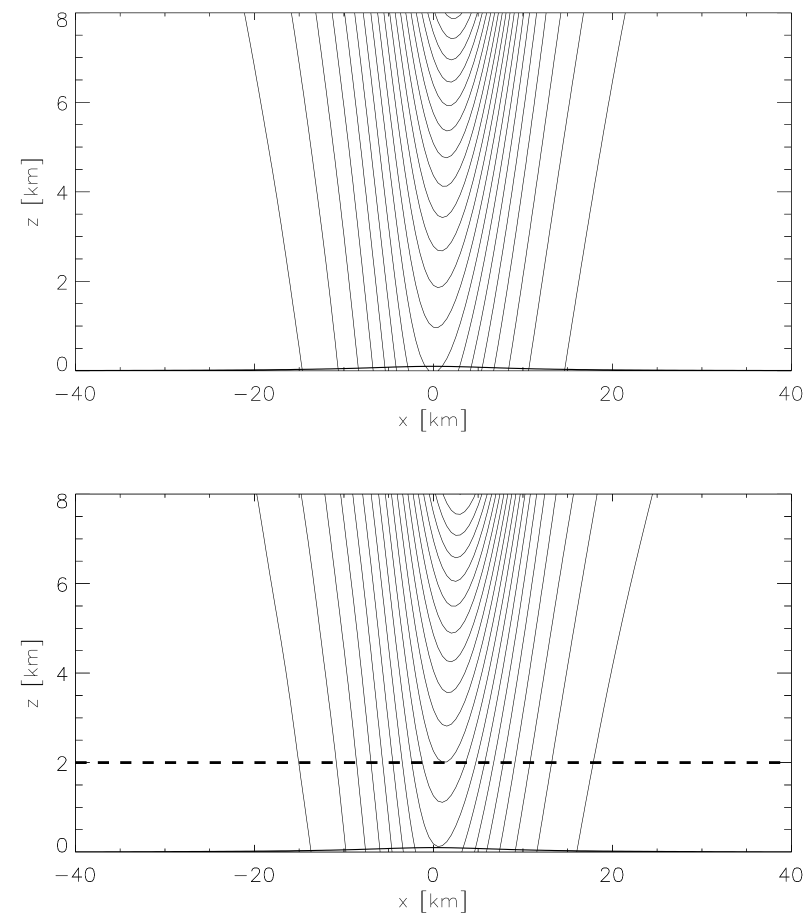

Figure 2.5: $\overline{uw}$ flux calculations for the linear hydrostatic wave case from FT_o (top panel) and FT_w (bottom panel). Contour intervals are $0.02\mathrm{m}^2\mathrm{s}^{-2}$. The hill is superimposed on the bottom of both plots, and the dashed line in the bottom plot indicates the initialization height of FT_w.

Vertical cross-sections for the horizontal momentum flux $\overline{uw}$ calculations are shown for the hydrostatic case in Fig. 2.5 for both FT_h (top panel) and FT_w (bottom panel). There is good agreement between both FT methods in this case. Researchers tend to be more interested in the parameter $\rho\overline{uw}$, as according to linear theory it does not change in the vertical direction as long as there is no critical layer or other cause of momentum exchange between the wave field and the background atmospheric flow. Corresponding plots of $\rho\overline{uw}$ are shown in Fig. 2.6 for FT_h (top panel) and FT_w (bottom panel). $\rho\overline{uw}$ is more constant

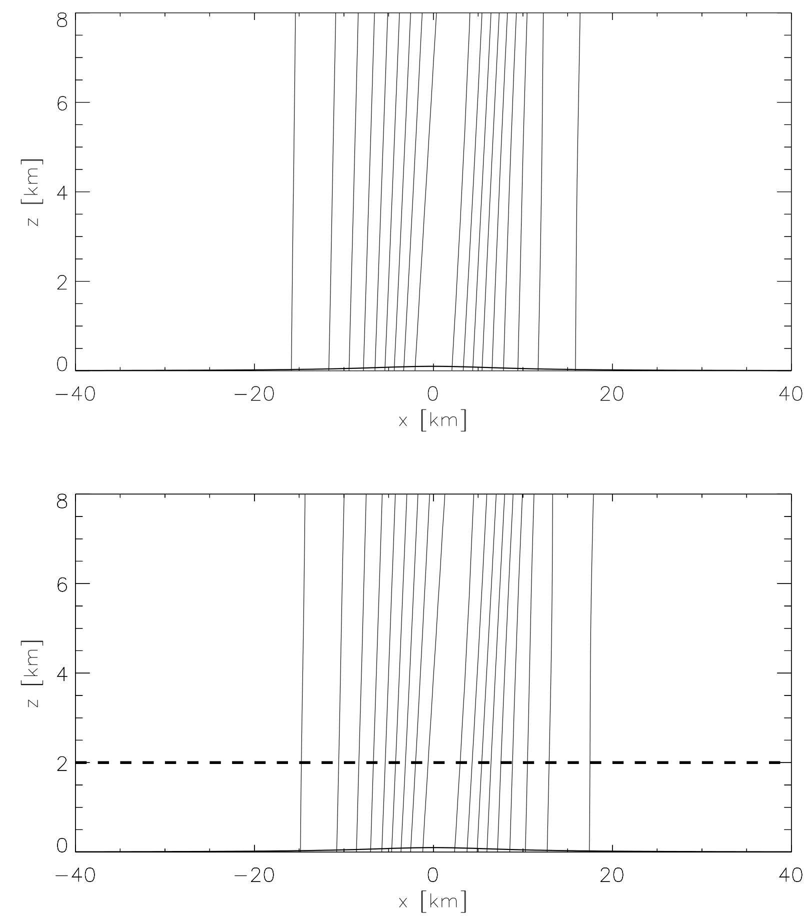

Figure 2.6: $\rho\overline{uw}$ flux calculations for the linear hydrostatic wave case from FT_o (top panel) and FT_w (bottom panel). Contour intervals are $0.02\mathrm{kgm}^{-1}\mathrm{s}^{-2}$. The hill is superimposed on the bottom of both plots, and the dashed line in the bottom plot indicates the initialization height of FT_w.

in the vertical, though for both cases the fluxes are slightly dispersive near the top.

We also calculate the horizontal area averages of the fluxes on all of the vertical levels. We define the area flux average as the sum of $\rho\overline{uw}$ over all of the grid points on a horizontal surface divided by the number of grid points. This is a somewhat arbitrary way to calculate a flux average, though it tells us which FT method has a larger overall wave momentum flux amplitude across the model domain. Since FT is adiabatic and reversible, there is no change in the horizontal flux averages on different horizontal surfaces. In other words, the horizontal flux average is constant with height. For FT_o, the area flux average for $\rho\overline{uw}$ is $-0.0113\mathrm{kgm}^{-1}\mathrm{s}^{-2}$, and for FT_w the flux average is $-0.0112\mathrm{kgm}^{-1}\mathrm{s}^{-2}$. FT_w has a slightly higher average (possibly due to the terrain-following lower boundary of WRF), but both averages are very close to each other. As the flow is well within the linear regime, we would expect similar agreement between both FT methods.

2.4 Remarks

In this chapter we have provided a detailed examination of the WRF and FT models. The WRF model is nonlinear and non-hydrostatic, and uses a terrain-following coordinate system. In addition, the WRF model is a mesoscale meteorological model and is capable of being utilized for simplified, idealized numerical experiments. This, in theory, makes WRF a suitable model for our studies here, as we require that the orography provide the forcing which drives the solutions, given that everything else is in a hydrostatically balanced steady state. We would also like to note that throughout the research conducted here, the WRF model has been (and still is) constantly being updated for bug fixes and new features. This is both advantageous and has its problems. A updated bug fix or a new upper level damping scheme might provide solutions with higher accuracy, but at some point we have to accept a current version of the model as being 'good enough' so as not to delay our research with more and more simulations of the same problem. Thus WRF version 2.2 was chosen for keeps (as of this writing, the current version 2.2.1).

A thorough review of the FT model was also given, and both of its initialization schemes were reviewed. The FT method is used to obtain linear, non-hydrostatic wave field solutions, and has previously been applied to mountain wave problems. When the FT model is initialized with the surface vertical displacement, assumed to be the orography, the solutions obtained are identical with many other linear analytical solutions (such as the one described in section 1.3). For clarity, when using this particular method we denote it as FT_o. A new feature of the FT method is for it to be initialized with a vertical velocity field, which can be done on any horizontal level (and not just at the lower boundary). We hope that this initialization method (denoted as FT$_w$) will make FT more robust, enabling its usage for a wider variety of flow regimes. Thus WRF model solutions are useful for FT$_w$ in two ways: (1) provide a horizontal w initialization field for FT$_w$, and (2) assess the accuracy of the Fourier Transform methods.

A series of comparisons between the WRF, FT$_o$, and FT$_w$ solutions have been shown for the analytical linear solution derived in section 2.3. The FT, WRF, and the analytical solutions are in overall good agreement for the hydrostatic, non-hydrostatic, and evanescent wave regimes in uniform flow for a Froude number of 9.1. Although comparisons between nonlinear models and analytical solutions for this particular case have previously been carried out (Durran and Klemp, 1983; Doyle, 2005), this is, to our knowledge, the first time that a direct comparison has been made with the new FT$_w$ initialization scheme featured in this dissertation.

The following two chapters focus on the next challenge: examining the accuracy of both FT methods in nonlinear flow regimes. The source of flow nonlinearity is the orography, as the flow is kept uniform (i.e. we will not be concerned with atmospheric phenomena such as lee waves and external critical layers). As many of the world's mountain ranges commonly experience at least moderately nonlinear flows, we believe this research can be of use to the mountain wave parameterization community and increase our understanding of gravity wave generation in nonlinear flow regimes induced by the orography.

Chapter 3: Low Froude Number Flows Over a Bell-Shaped Mountain

3.1 Introduction

The Fourier Transform method, explained in chapter 2, has been shown to produce accurate results of mountain wave fields for linear, high Froude number flows. The contour plots in Figs. 2.1 and 2.2, agree very well with their analytical counterparts for both the FT_w and FT_o methods (recall that the subscript w refers to the Fourier initialization scheme involving WRF, and the subscript o refers to the surface initialization scheme using orography as vertical displacement).

One of the major goals of this dissertation is to assess the feasibility of applying FT_w to mountain waves cases in nonlinear flow regimes. Previous studies indicate that the traditional application of the linearized lower boundary condition (surface vertical displacement field) leads to erroneous drag estimates after the transition to a nonlinear flow regime (Bacmeister and Pierrehumbert, 1988; Miranda and James, 1992). In this chapter we attempt a novel approach - initializing FT with the wavefield produced in a nonlinear flow. As outlined in sections 2.2 and 2.3 FT_w is initialized with a horizontal cross-section of w at a given height from WRF. A limiting factor is that the initialization height must be above the lower atmospheric nonlinear processes. This method is also discussed in Lindeman et al. (2008).

We compare the wave field solutions from FT_w and FT_o to the corresponding WRF model results to assess their overall accuracy. The accuracy of FT_w to various height initialization levels is also examined to determine a 'lower bound' at which the FT_w scheme is appropriate. The concept of a 'wave orography' field is introduced in this chapter. The lower boundary vertical displacement η field, which is traditionally assumed to be the orographic height field, can also be computed in the FT_w method by ray-tracing the solution downwards to the surface. Also, the applicability of FT_w to the quasi-steady WRF wave field is assessed for very low Froude number flows. Finally, momentum flux calculations are presented which exemplify the difference in the predictions of FT_o and FT_w.

Much can be learned about low Froude number flow regimes by comparing linear and nonlinear results for the wave field. These results only concern very idealized flows over a single bell-shaped hill, though these restrictions can be relaxed once the dynamics of the simplest flow are better understood.

3.2 The Experiments

Schär and Durran (1997) perform a series of numerical simulations for idealized low Froude number flows. The experiments presented here follow in their manner: we consider uniform (unsheared) flows impinging upon a three-dimensional mountain of the form

$$h(x,y) = \frac{h_m a^3}{(x^2 + y^2 + a^2)^{3/2}}, \tag{3.1}$$

where h_m is the mountain height and $a = 10$km the half-width. Horizontal Cartesian coordinates are (x, y), and the elevation is $h(x, y)$. The initial flow is homogeneous, where $U = 10\mathrm{ms}^{-1}$ and $N = 0.01\mathrm{s}^{-1}$. The two cases presented here are for Froude number flows of 2/3 and 1/3, and so the varying parameter here is $h_m = 1.5$km for $Fr = 2/3$ and $h_m = 3$km for $Fr = 1/3$.

The WRF model is run for 6 hours with 2s timesteps for all of the cases presented in this chapter. The FT_w method is initialized with a horizontal cross-section of WRF's w

velocity field at 6km in all cases except for the sensitivity tests in section 3.3. FT_w is then ray-traced both upwards and downwards to obtain the mountain wave solution. FT_o is initialized with the same orographic data set as WRF.

We use the same domain specifications for all of the simulations presented in this chapter. The horizontal domain is 300×300km, with a grid resolution of 1km. Although the top of the WRF is 30km, the sponge layer occupies the upper half of the domain so that only the lowest 15km are considered for the results. As in Lindeman et al. (2008), there are 150 grid points in the vertical for WRF for the Froude number of 2/3 case, of which 23 are in the sponge layer. The vertical grid spacing increases gradually from about 100m at the ground to 200m at $z = 15$km. In all subsequent cases in this and the next chapter, the total number of vertical levels are increased to 300 so that each vertical grid spacing is roughly 100m. FT can produce horizontal cross-sections of the solution at any height. For the vertical cross-sections shown in this chapter, FT results are taken at every 100m in the vertical.

3.3 Idealized Bell-Shaped Hill - Froude = 2/3

As examined in section 1.4.1, the lower atmospheric flow regime in this case is dominated by a near-surface wind maximum and a hydraulic-type 'jump' with TKE generation on the lee of the hill and in the breaking wave regon. We begin with an x-z cross-sections of the vertical velocity field from WRF, FT_w, and FT_o in the top, middle, and bottom panels of Fig. 3.1, respectively. Overall, agreement between WRF and FT_w is good except in the lowest several kilometers of the domain where the solutions begin to diverge. This discrepancy can be explained in the corresponding WRF vertical cross-section of isentropes and regions of TKE shown in Fig. 3.2. As can be seen in the plot, the squeezed isentropes over the lee slope is indicative of a wind speed maximum just over the surface, and then significant amounts of TKE exists in the 'jump' region over the lee slope. The vertical extent of the

TKE, about 4km, is roughly where the solutions begin to diverge. The vertical velocity below this height is significantly influenced by nonlinear processes. The extent of the TKE in these lower heights is the principal reason of initializing FT_w at a higher level.

The FT_o solution is much different than the other two solutions, indicating that the traditional linearized lower boundary is not appropriate for this case. We then apply divided streamline theory as the lower boundary condition for the FT_o simulation. The resulting hill shape is a modified version of the lower boundary vertical displacement field in the FT_o simulation, where in this case all heights below are set to the divided streamline height of 500m. The resulting FT solution is shown in the vertical cross-section of Fig. 3.3, where the modified orography is denoted by the solid line. As in the FT_o simulation, the w wavefield solution does not resemble the corresponding WRF wavefield.

Horizontal cross-sections at 14km altitude for w are shown in Fig. 3.4 from the WRF model (upper left panel), FT_w (upper right panel) and FT_o (lower panel). As in the vertical cross-sections, there is good agreement between WRF and FT_w, but not FT_o. The WRF wavefield in this case is more characteristic of a non-hydrostatic solution, with the waves extending downstream of the mountain. It is presumed that the wavefield is affected by the lower level wave breaking and TKE generation, which modifies the solution to an extent that smaller wave modes become more dominant.

Next, we back-trace the FT_w solution to 500m to visualize the vertical displacement field. The 500m level, which is the dividing streamline level for this case, was chosen as the height to plot the 'wave orography'. A contour plot of the vertical displacement field near and downstream of the mountain is shown in Fig. 3.5. It can be seen that the vertical displacement contours gradually increase upwind of the mountain to the summit, and then sharply descend in the lee to a minimum. This is most likely indicative of the hydraulic jump features observed in the WRF results, and suggests a different type of flow response to the orography than that predicted by dividing streamline theory. Over a short distance

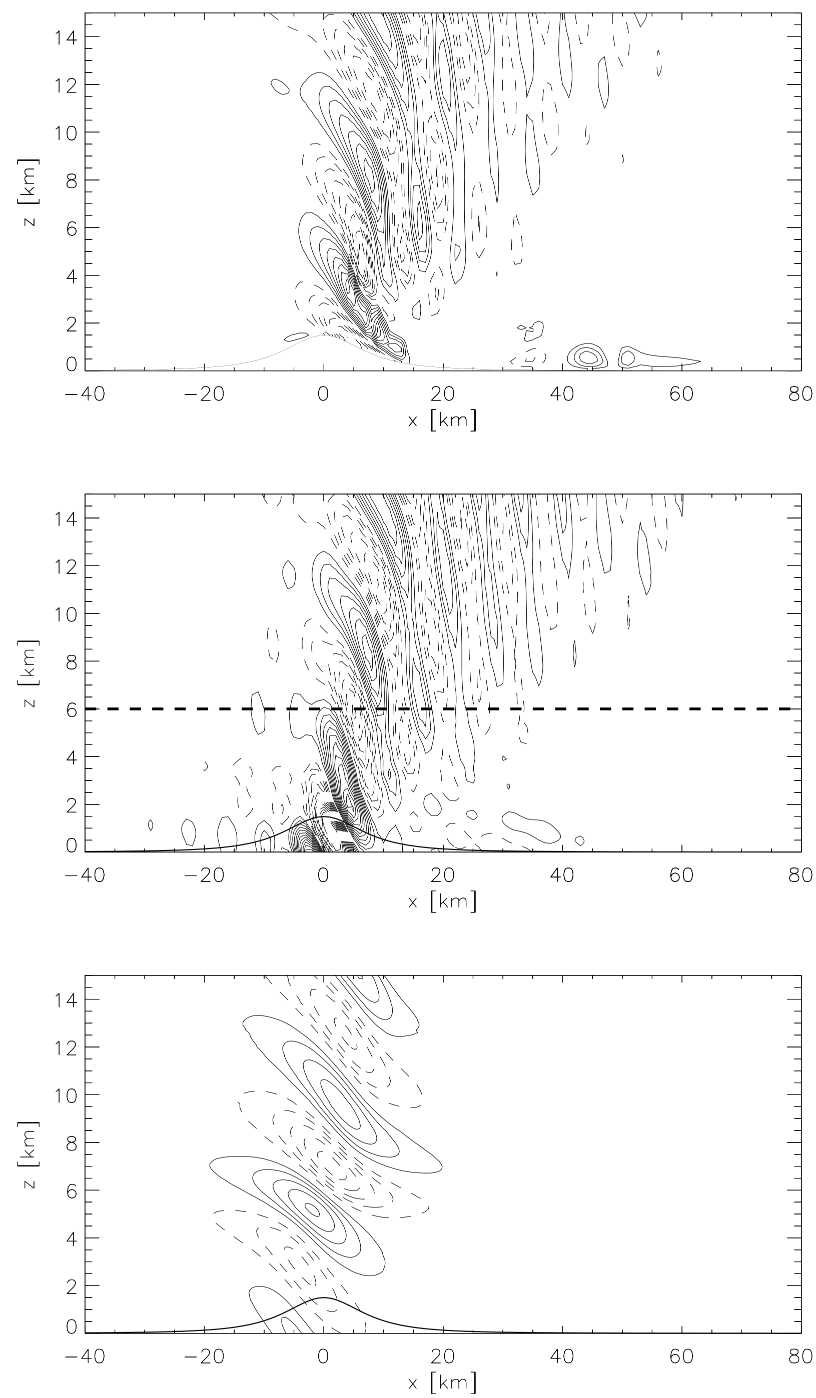

Figure 3.1: Vertical cross-sections for w taken at $y = 0$ (the centerline of the mountain) from WRF (top panel), FT_w (middle panel), and FT_o (bottom panel). The dashed line in the middle panel indicates the initialization height, and the orographic height is shown by the line in both FT solutions. For all plots, w contour intervals are $0.3\mathrm{ms}^{-1}$ and negative contours are dashed. The zero contour is omitted.

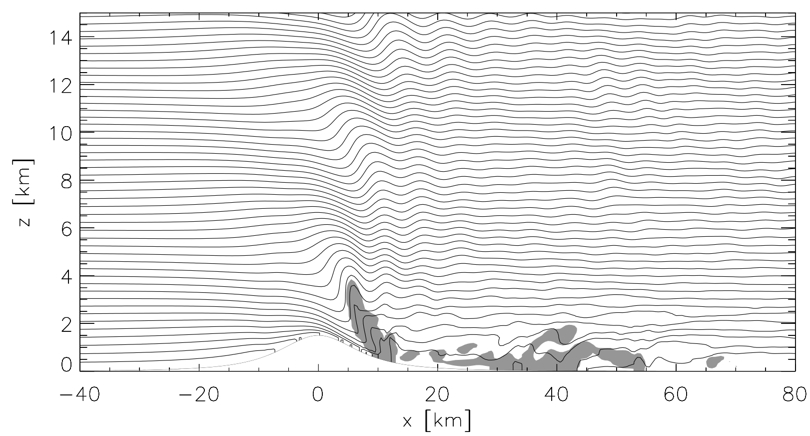

Figure 3.2: WRF vertical cross-section of potential temperature contours and areas of TKE (shaded regions). θ contours are 1K.

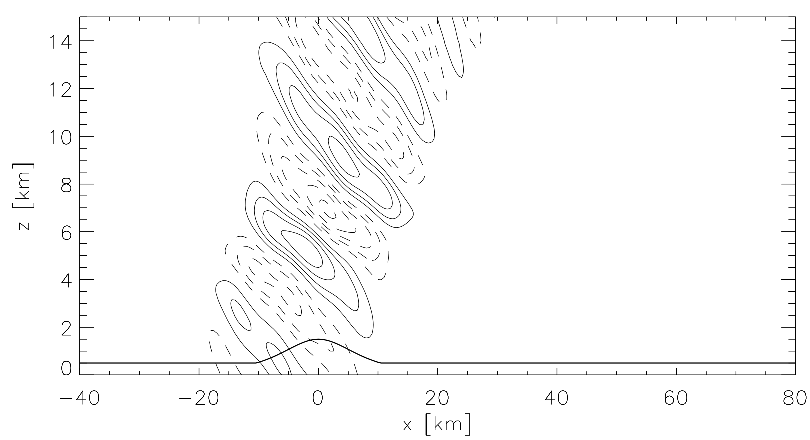

Figure 3.3: x-z vertical cross-sections for w taken at $y = 0$ (the centerline of the mountain) from the Fourier Transform method initialized with the dividing streamline height for the $Fr = 2/3$ case. The orography is similar to the real orography, except that all elevations below 500m are set to that level. Contour intervals are 0.3ms^{-1} and negative contours are dashed. The zero contour is omitted.

from the summit, the vertical displacement changes from a maximum value of 1882m to a minimum of 23m - a total change of 1859m. The vertical displacement field at this level shows that divided streamline theory does not accurately predict the wave response to the

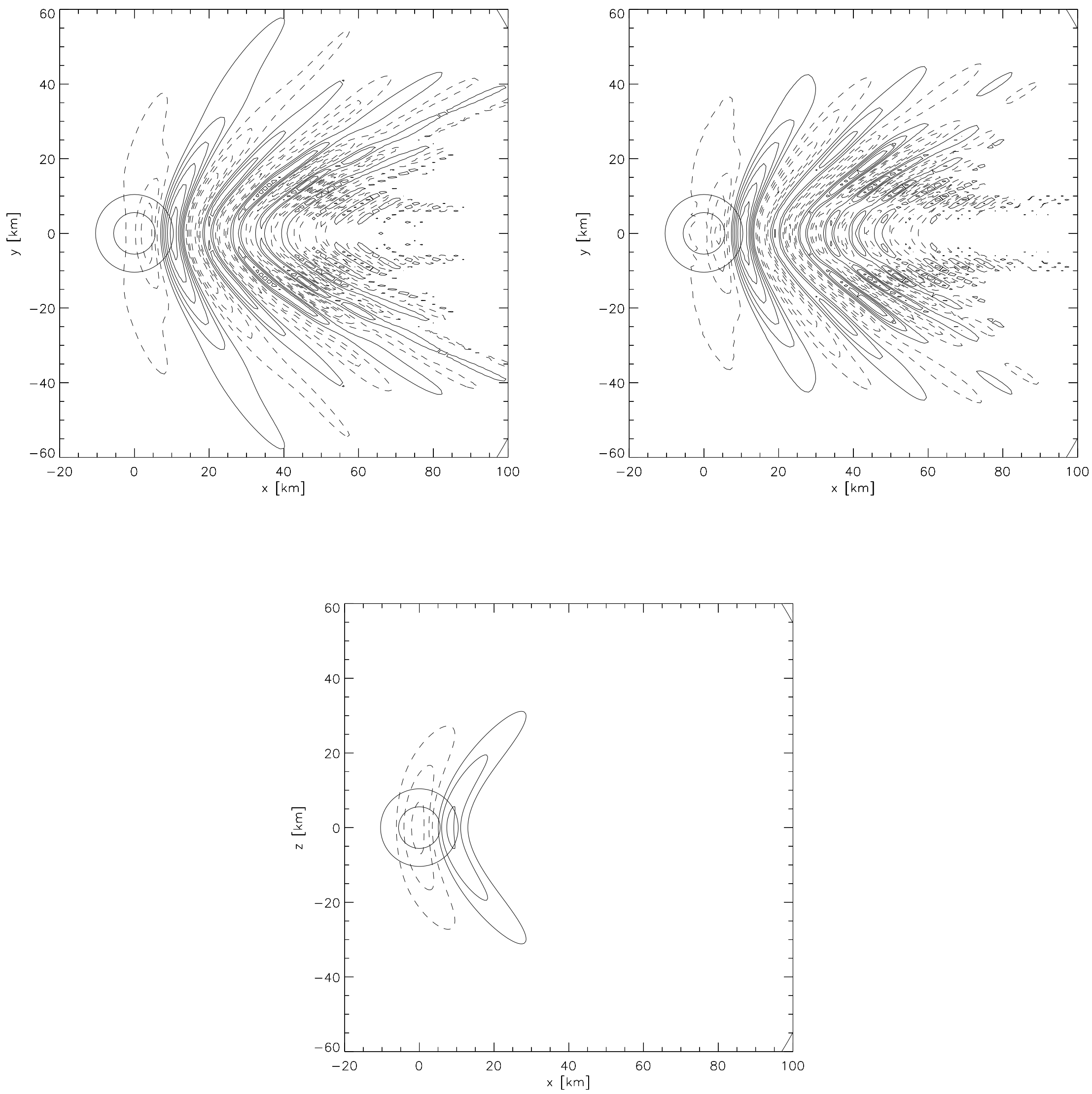

Figure 3.4: Horizontal cross-sections for w taken at 14km from WRF (upper left panel), FT_w (upper right panel), and FT_o (lower panel). For all plots, w contour intervals are $0.3\mathrm{ms}^{-1}$ and negative contours are dashed. The zero contour is omitted.

flow for this particular case. It should be noted that the we are not attempting to predict the dividing streamline height or analyze how the flow at this level crosses the mountain. Instead, we are only inferring wave field characteristics and deriving a linearized lower

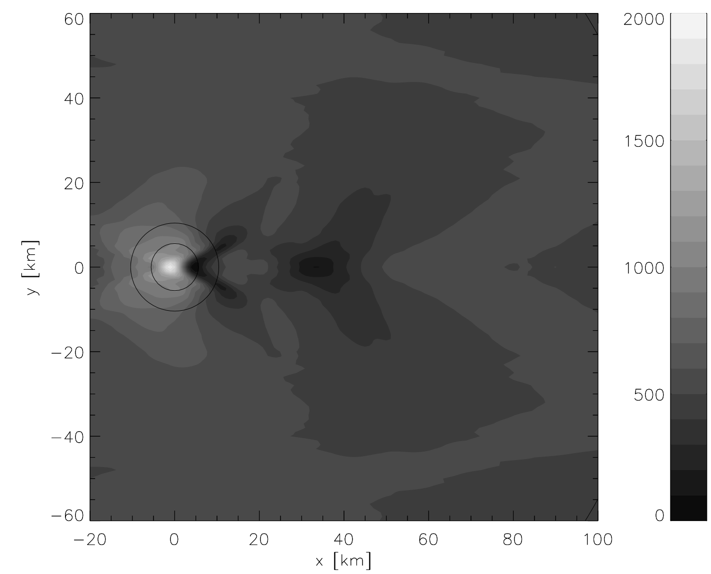

Figure 3.5: Plot of the vertical displacement surface from FT_w at 500m for the $Fr = 2/3$ case. The displacement height corresponds to the divided streamline height predicted by Eqn. (1.25). Orographic contours are 100m.

boundary condition suitable for mountain wave parameterization schemes.

FT_w can accurately reproduce the WRF solution at 6km, but we are also interested in examining the sensitivity of the FT_w solution when initialized at different heights. Fig. 3.6 shows identical wave field vertical cross-sections to those in the middle panel of Fig. 3.1, but this time initialized at 4km (top) and 2km (bottom). Not surprisingly, the FT_w wave field is not as accurate when initialized at 2km. At this level, nonlinear processes such as wave breaking and TKE generation are occurring, and so the application of linear theory will not yield a solution with the same accuracy as one with a higher initialization level. When FT_w is initialized at 4km, the wave field resembles the WRF solution more closely.

This case has shown that the traditional vertical displacement lower boundary used in

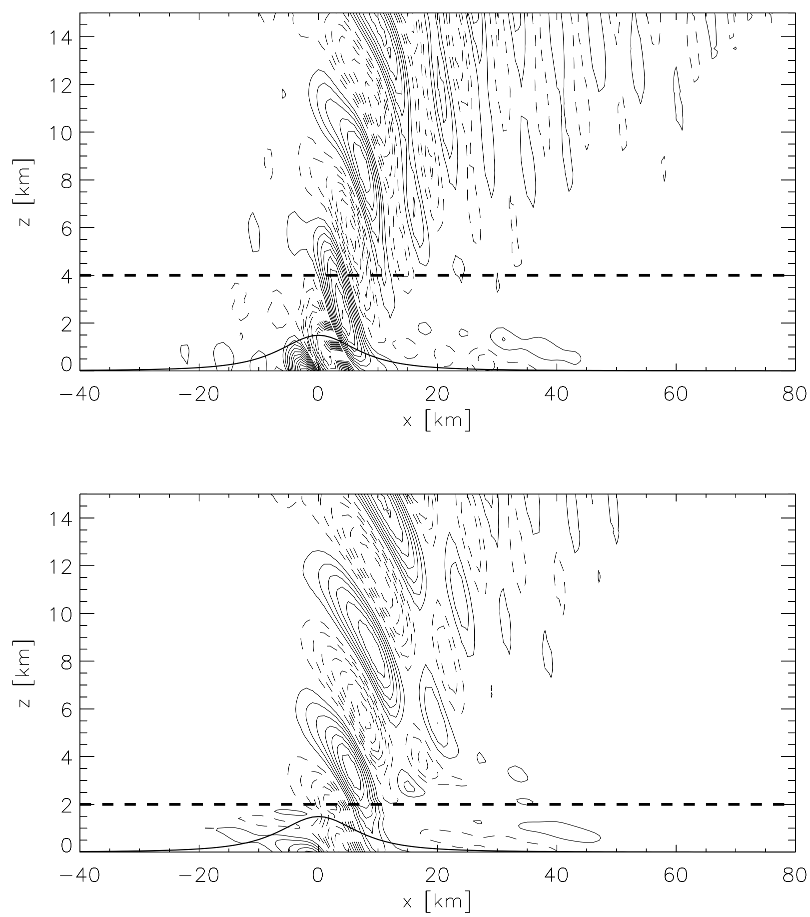

Figure 3.6: x-z vertical cross-sections of w from FT_w when initialized at 4km (top panel) and 2km (bottom panel). The dashed line denotes the level of initialization, and the solid line is the mountain height. w contour intervals are $0.3\mathrm{ms}^{-1}$ and negative contours are dashed. The zero contour is omitted.

linear applications is not suitable for low Froude number nonlinear flows. A more appropriate initialization scheme for the Fourier Transformation method is to initialize the linear model with w results from WRF above the lower level nonlinear flow. This new initialization scheme allows more more accurate predictions of useful linear parameters such as momentum flux and the wave field. The FT_w initialization scheme also shows that the wave field is predominantly linear above the mountain (from the close agreement with the WRF model resutls).

3.4 Idealized Bell-Shaped Hill - Froude = 1/3

Previous research has shown that the lower atmospheric flow in the $Fr = 1/3$ case is very nonlinear (section 1.4.1). There is a significant amount of flow splitting around the mountain, a large lee vortex pair, and upstream flow blocking. Unlike the previous case where the wavefield achieves a quasi-steady state after about 3 hours of model simulation time, some temporal variability is evident in the wave field in the $Fr = 1/3$ case. The unsteady nature of the wave field can be seen in Fig. 3.7, which shows vertical cross-sections of w for 5 hours (top panel) and 6 hours (bottom panel) of WRF simulation time. While the primary wave train above and to the lee of the mountain appears to be consistent for both times, smaller transient waves propagate upwards and away from the mountain. These waves can be seen just to the right of the main wave train. It is beyond the scope of this dissertation to attempt to explain why the wave field here is more transient than in the previous case, so we will just assume that these results are correct when assessing the FT method for this case. In the present WRF simulation, the intense TKE region is confined to within the lowest 5km of the domain, and so FT_w is initialized at 6km.

The transient features in the flow present some difficulties for the FT_w initialization scheme outlined in this dissertation, which assumes a steady state. When FT_w is initialized from WRF, the shorter transient waves will be super-positioned onto the longer, steadier waves. FT, of course, assumes all of these wavelengths are part of a steady-state wave field. WRF-initialized FT_w solutions for 5 and 6 hours are shown in the top and bottom panels of Fig. 3.8 Differences between the wave fields of WRF and FT are evident in the solutions, though the fields are not so different as to render the FT_w method unusable at this low Froude number. Indeed, the solution continues to be more representative of the WRF solution than the solution given by FT_h (bottom panel in Fig. 3.8).

Horizontal cross-sections from WRF and FT_w are shown after 6 hours of WRF model

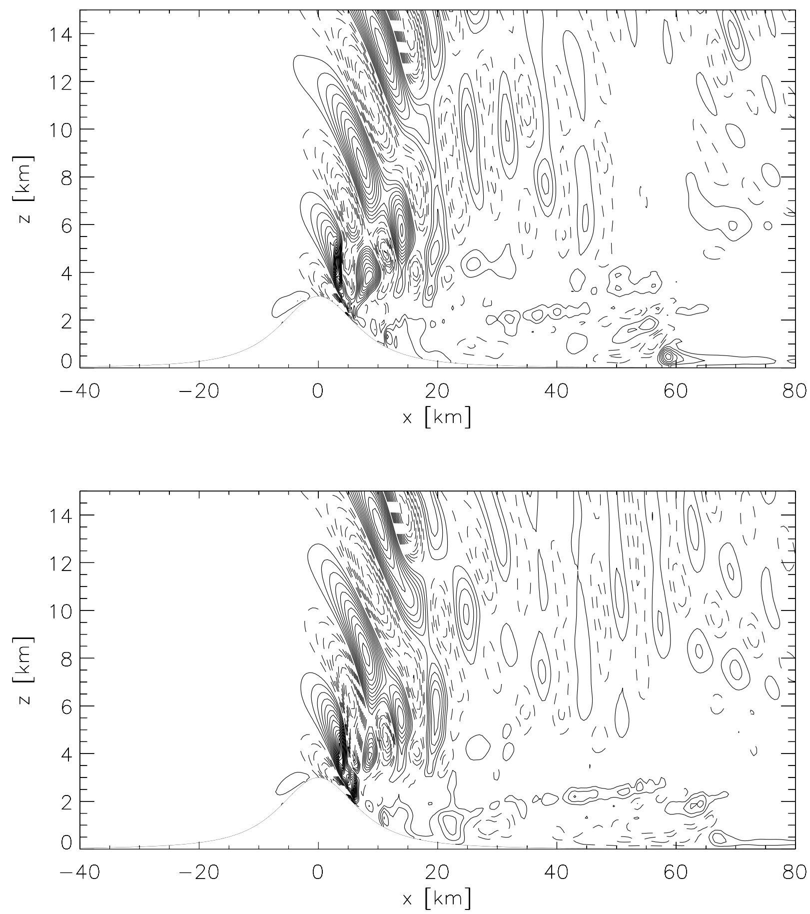

Figure 3.7: x-z vertical cross-sections (at $y = 0$) of the WRF w solution after 5 hours (top panel) and 6 hours (bottom panel). w contour intervals are 0.3ms^{-1} and negative contours are dashed. The zero contour is omitted.

simulation time in Fig. 3.9. It can be seen that despite unsteadiness in the wave field observed in the WRF simulation, the FT_w results continue to be more representative of the nonlinear WRF results than FT_h (bottom panel of Fig. 3.9).

We also plot the vertical displacement surface at 2000m altitude (the divided streamline height) from FT_w after 6 hours of WRF simulation time

The total height change of the vertical displacement surface is 804m, which is much less than in the $Fr = 2/3$ case. It is not completely understood why the height change is

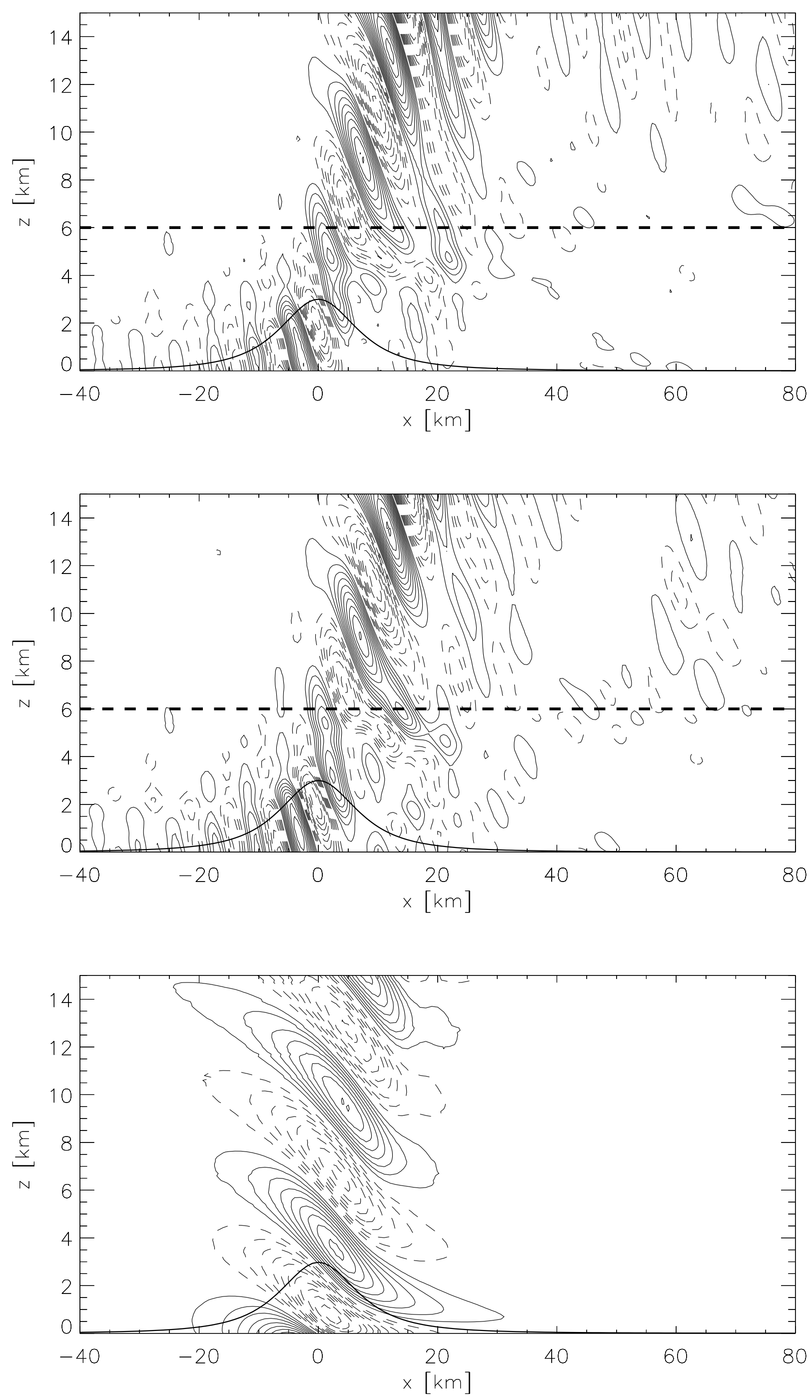

Figure 3.8: x-z vertical cross-sections (at $y = 0$) of the FT_w w solution corresponding to 5 hours (top panel) and 6 hours (middle panel) of WRF simulation time. Bottom panel - corresponding FT_o solution. w contour intervals are $0.3\mathrm{ms}^{-1}$ and negative contours are dashed. The zero contour is omitted.

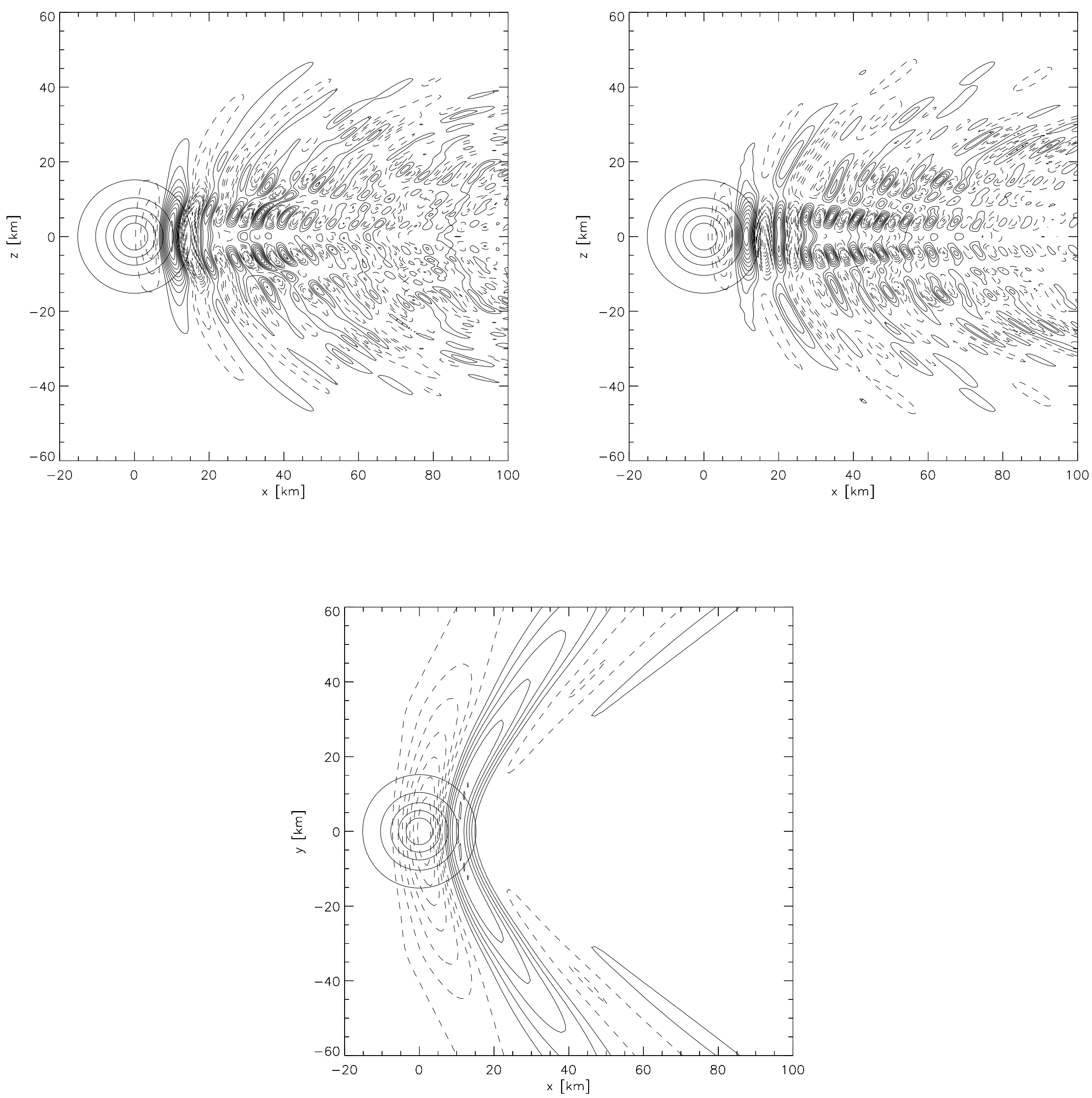

Figure 3.9: Horizontal cross-sections for w taken at 14km after 6 hours of WRF simulation time from WRF (upper left panel) and FT_w (upper right panel). Lower panel - corresponding FT_o solution. For all plots, w contour intervals are $0.3\mathrm{ms}^{-1}$ and negative contours are dashed. The zero contour is omitted.

less for this flow regime, but we would conjecture that the smaller displacement change is related to the prevalent nonlinear features for this case such as flow splitting around the mountain and a large vortex pair in the lee. These types of nonlinear flow processes act

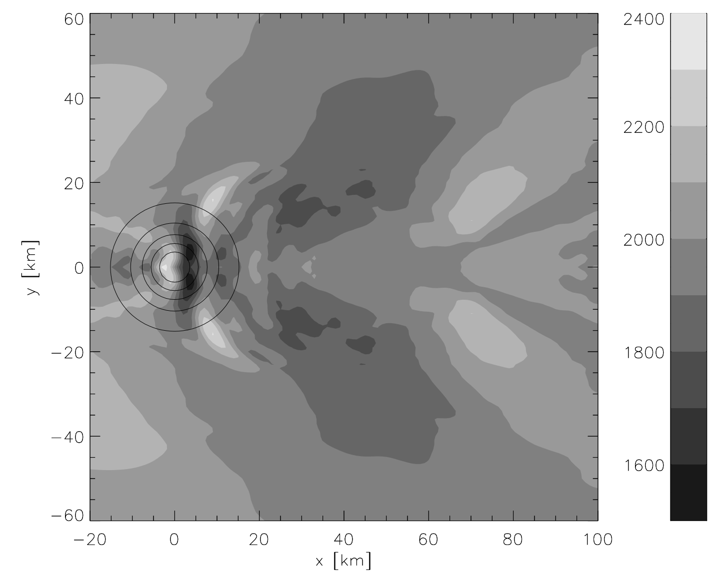

Figure 3.10: Plot of the vertical displacement surface from FT_w at 2km for the $Fr = 1/3$ case. The displacement height corresponds to the divided streamline height predicted by Eqn. (1.25). Orographic contours are 100m.

to decrease the wave amplitude more so than the wave breaking and TKE observed in the $Fr = 2/3$ case. The displacement change for the $Fr = 1/3$ case is more characteristic of what would be expected from dividing streamline theory, and is in qualitative agreement with the reduced mountain wave amplitudes as observed during the PYREX and MAP field experiments (section 1.4.1).

3.5 Momentum Flux Calculations

Momentum flux calculations from the $Fr = 2/3$ case are presented for both the FT_w and FT_o results. Vertical x-z cross-sections of $\rho\overline{uw}$ are shown in Fig. 3.11 for FT_w (top panel) and FT_o (bottom panel). The flux concentrations generally decrease with height due to the

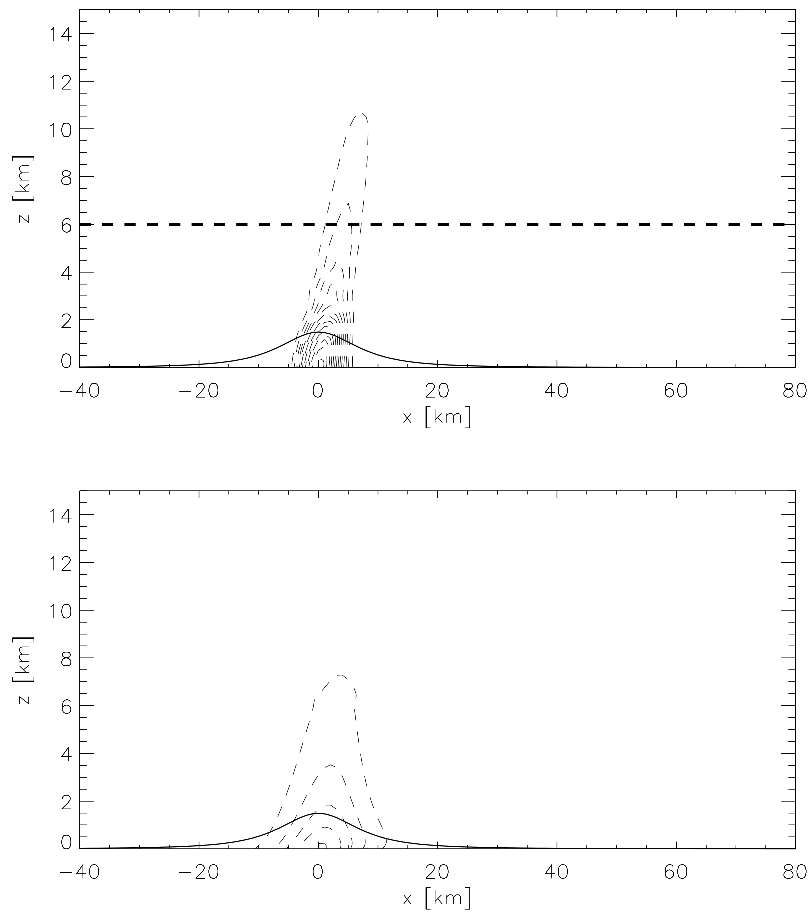

Figure 3.11: $Fr = 2/3$ case: x-z vertical cross-sections (at $y = 0$) of the $\rho\overline{uw}$ solution from FT_w (top panel) and FT_o (bottom panel). Contour intervals are $2\mathrm{kgm}^{-1}\mathrm{s}^{-2}$ and negative contours are dashed. The zero contour is omitted.

dispersive nature of the gravity wave fluxes over a circular shaped hill in a three-dimensional domain. The horizontally averaged density momentum flux is $0.0188\mathrm{kgm}^{-1}\mathrm{s}^{-2}$ for FT_w and is $0.0235\mathrm{kgm}^{-1}\mathrm{s}^{-2}$ for FT_o. This would indicate that usage of the traditional linearized lower boundary leads to a somewhat high momentum flux estimate. The horizontally averaged momentum flux $\rho\overline{vw}$ is negligible in this case.

Horizontal cross-sections of $\rho\overline{uw}$ at 14km are shown in Fig. 3.12 for FT_w (top left panel) and FT_o (top right panel). Corresponding $\rho\overline{vw}$ cross-sections are shown for FT_w (bottom

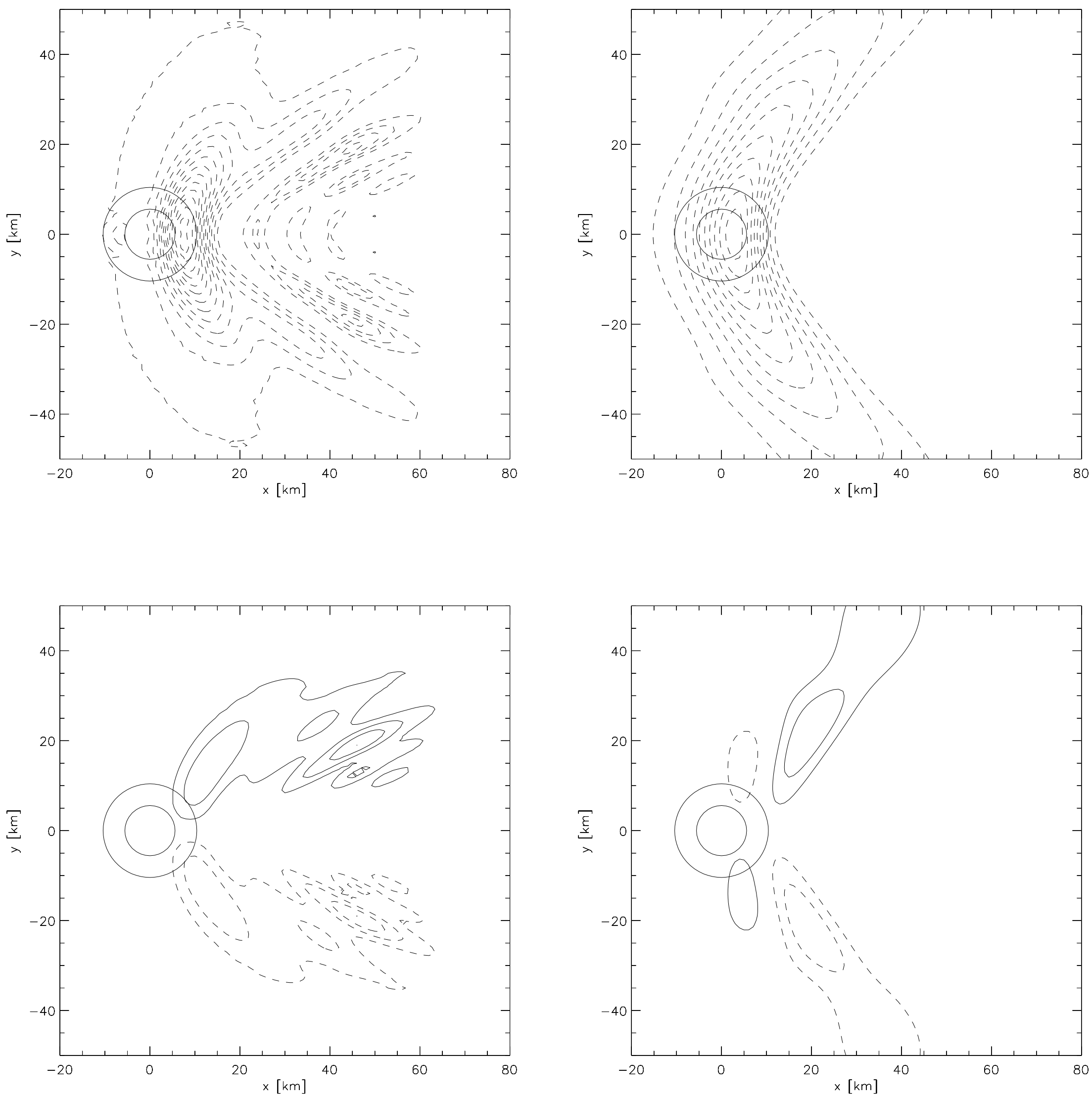

Figure 3.12: $Fr = 2/3$ case: Horizontal cross-sections at 14km of $\rho\overline{uw}$ from FT$_w$ (top left panel) and FT$_o$ (top right panel), and $\rho\overline{vw}$ from FT$_w$ (bottom left panel) and FT$_o$ (bottom right panel). Contour intervals are 0.1kgm^{-1}s^{-2} and negative contours are dashed. The zero contour is omitted.

left panel) and FT$_o$ (bottom right panel). Both $\rho\overline{uw}$ FT results show a lot of activity in the lee of the mountain, with the fluxes in FT$_w$ extending further downstream. Both FT methods produce localized regions of $\rho\overline{vw}$, but the net average is zero in both cases.

Vertical cross-sections of $\rho\overline{uw}$ are shown in Fig. 3.13 for FT_w (top panel) and FT_o (bottom panel) for the $Fr = 1/3$ case. Fluxes are much more evident in the FT_o solution than in FT_w. This is further reflected in the horizontally averaged density fluxes, as the FT_w averaged flux of $-0.016\text{kgm}^{-1}\text{s}^{-2}$ is less than one-fifth the FT_o value of $-0.094\text{kgm}^{-1}\text{s}^{-2}$. Nonlinear processes such as flow splitting, blocking, and the downstream vortices act to decrease the effective mountain height so that waves launched from the mountain are much weaker than linear predictions would otherwise suggest. In section 3.4 we mentioned that the wave field in this case was quasi-steady, which had an effect on the ability of FT_w to predict the wave field exactly. The momentum flux calculations are not very sensitive to the quasi-steadiness of the wave field in this case, as over the course of two hours prior to the results mentioned here the change in the horizontally averaged value is only about 5 percent.

Horizontal cross-sections at 14km of the momentum fluxes in this case are shown in Fig. 3.14, where $\rho\overline{uw}$ results for FT_w is in the top left panel and FT_o in the top right panel, and $\rho\overline{vw}$ results for FT_w and FT_h are shown in the lower left and lower right panels, respectively. The region of maximum $\rho\overline{uw}$ intensity as predicted by FT_w is located in a concentrated area in the lee, while the flux has more broad extent in the FT_o result. $\rho\overline{vw}$ results show some regional variability for both FT_w and FT_h, but the net effect of the fluxes averaged over the horizontal plane is zero..

A comprehensive picture of how the horizontally averaged wave momentum flux contribution varies with the Froude number is shown in Fig. 3.15. A series of WRF simulations are examined where Froude number is varied. These simulations are otherwise identical to the previous $Fr_h = 1/3$ case, except that the mountain height is varied to obtain Froude number values of 1.333, 1.17, 1.0, 0.83, 0.67, 0.50, and 0.33 (all of the WRF simulations use 300 vertical levels). We then calculate corresponding FT horizontal $\rho\overline{uw}$ averages for both FT initialization methods (FT_o is initialized with the surface vertical displacement

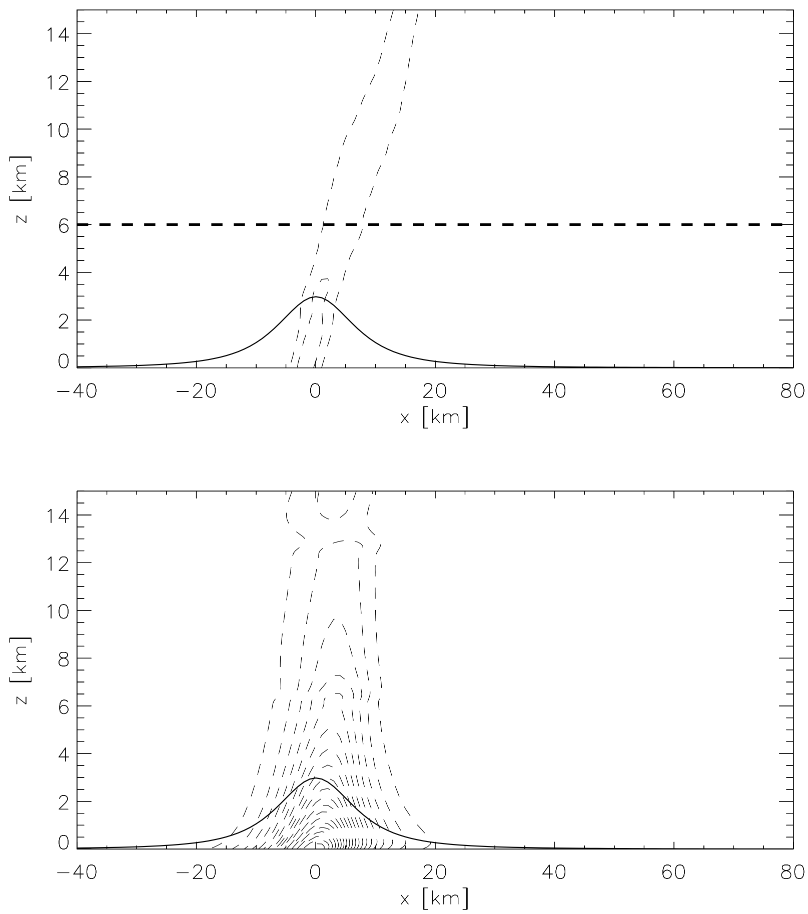

Figure 3.13: $Fr = 1/3$ case: x-z vertical cross-sections (at $y = 0$) of the $\rho\overline{uw}$ solution from FT_w (top panel) and FT_o (bottom panel). Contour intervals are $2\mathrm{kgm}^{-1}\mathrm{s}^{-2}$ and negative contours are dashed. The zero contour is omitted.

and FT_w initialized by WRF at 6km for all cases). In addition, two additional momentum flux averages are calculated. The first is from the FT_o initialization method, but we apply the dividing streamline theory. This method is only applicable for cases where the Froude number is less than unity. All terrain values below the dividing streamline height are set to it so that the effective Froude number is 1. The last horizontal momentum flux average is calculated from the WRF output at 6km. For these results, the perturbation u' values are

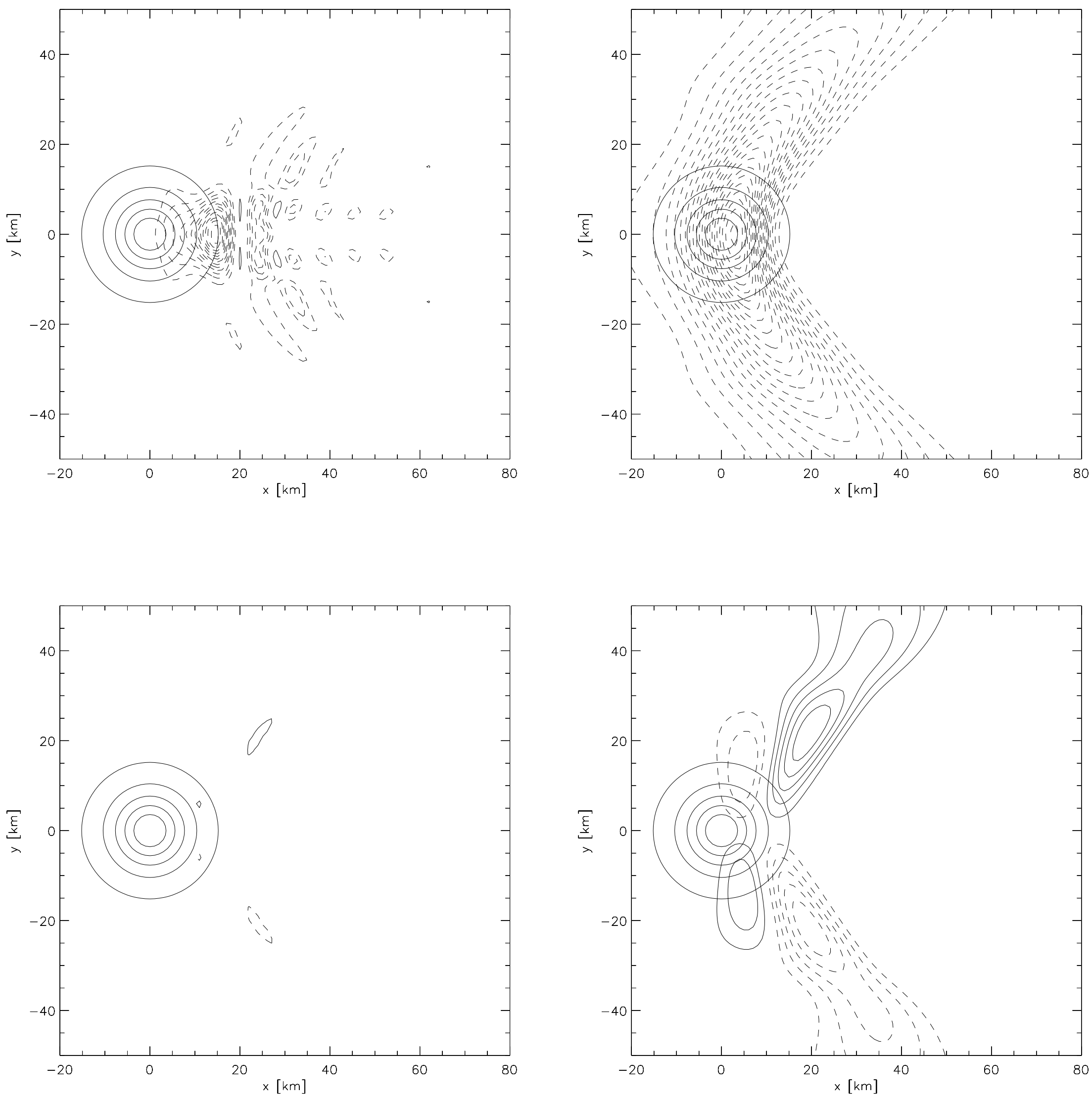

Figure 3.14: $Fr = 1/3$ case: Horizontal cross-sections at 14km of $\rho\overline{uw}$ from FT_w (top left panel) and FT_o (top right panel), and $\rho\overline{vw}$ from FT_w (bottom left panel) and FT_o (bottom right panel). Contour intervals are $0.1\mathrm{kgm}^{-1}\mathrm{s}^{-2}$ and negative contours are dashed. The zero contour is omitted.

obtained by subtracting the WRF u output by the initial u value of $10\mathrm{ms}^{-1}$ (WRF perturbation w' is unchanged from w). We then take the average of the perturbation WRF $u'w'$ over the horizontal area of the domain at 6km, and then multiply it by the mean density at that height. This provides a non-local horizontally averaged momentum flux value which is comparable to the FT horizontally averaged results.

It can be seen in Fig. 3.15 that the $\rho\overline{uw}$ momentum flux averages from FT_w and FT_o are similar for Froude numbers greater than one, but then diverge as Fr_h decreases (note that for convenience absolute values of $\rho\overline{uw}$ are used in the plot). When Fr_h is near or greater than unity, FTw (diamonds) has a slightly larger magnitude than FT_o (squares). This might be from wave amplification in WRF caused by the curvature of its lower boundary (i.e. the hill). There is no appreciable TKE or lee vortices for these particular WRF simulations. As the Froude number decreases below 0.83, TKE and lee vortices appear in the WRF solution, and the vortices grow stronger with decreasing Fr_h. These nonlinear processes act to suppress wave amplitude in the nonlinear WRF simulations, which is also clearly depicted in the FT_w averages (its maximum occurs at $Fr_h = 0.67$. The wave amplitude in the FT_o solutions increases dramatically as the Froude number decreases, which is reflected by the exponential increase of horizontal momentum flux averages.

The FT_o momentum flux averages using the dividing streamline height approximation (triangles) is maximum when Fr_h is near 1, but drops off slightly as Fr_h decreases. Since the effective Froude number is unity for all of the dividing streamline cases, the slight decrease in momentum flux averages is attributed to the change in the mountain shape. The WRF horizontally averaged momentum flux values (X's) closely agrees with the corresponding results of FT_w. This provides further support to the accuracy of the FT_w initialization method, and suggests that the WRF energy fluxes at this height level (6km) are dominated by wave activity. It can also be seen that while the traditional FT_o method greatly over-estimates the momentum flux average in low Froude number nonlinear regime flows, the FT_o method using the dividing streamline height approximation underestimates the average (when compared to the WRF and FT_w results).

4. Remarks

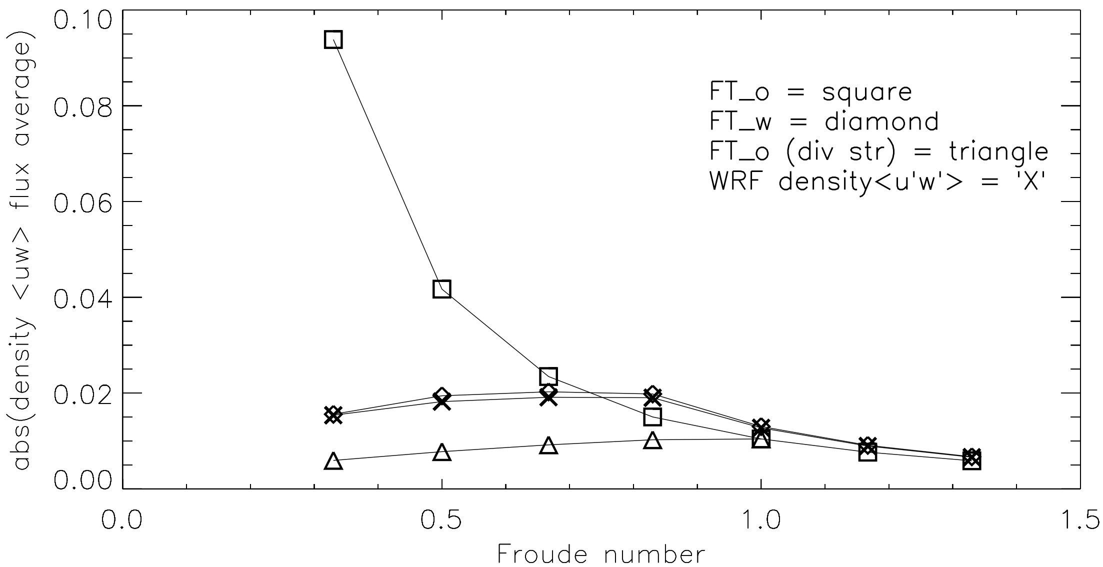

Figure 3.15: A plot of the horizontally averaged $\rho\overline{uw}$ fluxes from FT_o (squares), FT_w (diamonds), WRF (X's), and FT_o initialized with the dividing streamline height approximation (triangles) as a function of the Froude number. All of the cases are identical except for the mountain height, so that the Froude number values of the cases are 1.333, 1.17, 1.0, 0.83, 0.67, 0.50, and 0.33. Absolute values of the average momentum fluxes (units $\mathrm{kgm^{-1}s^{-2}}$) are shown for convenience.

In this chapter we showed that the WRF-initialized FT method provides wave field solutions which are more similar to corresponding WRF results than the traditional linear method of initializing FT with the surface vertical displacement field. Since FT methods are thousands of times faster computationally than mesoscale numerical weather models such as WRF, linearized wave fields can be generated over a large domain in a short period of time. For uniform flows over bell-shaped ridges, we can predict the wave field and associated momentum fluxes in nonlinear flow regimes with more confidence than before.

In addition to ray-tracing wave fields far from the source, the WRF-initialized FT model can also follow the waves back towards the ground. This allows us to obtain a surface vertical displacement field, i.e. the 'wave' orography, which is potentially useful for global weather model parameterization schemes. By testing the FT model in nonlinear flow regimes, we were able to learn much about the dynamical behavior of the flow interacting with the mountain. In the $Fr = 2/3$ case, the wave field above the mountain was found to be well approximated by linear theory above approximately 4km altitude, which coincides with the highest extent of the TKE-intense region associated with the breaking wave.

There was some variability in the wave field in the $Fr = 1/3$ case, but the FT_w solution continues to be substantially more representative of the actual wave field than traditional linear methods. There was only minor temporal variability in the wave momentum fluxes predicted by FT_w, which was negligible compared to the difference of corresponding fluxes predicted by FT_o.

A relatively simple uniform flow regime over a bell-shaped mountain was considered in this chapter. For a more realistic look into atmospheric flows over actual orography, we present several cases of low Froude regime flow over two idealized mountain peaks and the complex orography of Hawaii.

Chapter 4: The Flow Around Hawaii

4.1 Introduction

In the previous chapter, we saw how nonlinear flow around a single bell-shaped mountain can affect the generation of wave fields. This study is extended cases where the orography is increasingly complex. The first two cases consists of two idealized mountains, and the orography used in the latter cases are of the Big Island of Hawaii, which consists of four prominent peaks. A primary motivation in this chapter is to assess how well FT_w (the Fourier Transform model initialized by WRF) performs for low Froude number flows over more realistic orography. If this method performs reasonably well in regions of complex orography, that will be a major step in its robustness and applicability in areas such as mountain wave parameterization schemes.

As was mentioned in chapters 1 and 3, in low Froude number flows, the flow around a single obstacle obstacle becomes very much distorted. The flow upstream of the obstacle decelerates to the point of stagnation and even can become negative. Flow below a certain height (the dividing streamline height) is diverted around the obstacle, instead of passing over it, and a vortex pair forms to the lee. These low level nonlinear processes become stronger and more dominant as the Froude number is decreased.

In the current chapter nonlinear flows around complex orography are examined. In particular, we want to see how the nonlinear flow regime in the vicinity of an obstacle affect the wave generating capability of nearby obstacles. Since the flow field is particularly affected by low Froude number flows, two case studies are examined for Froude number regimes of 0.33 and 0.2. The chapter begins with simulations of an idealized case with two mountain peaks, and then the flow around the Big Island of Hawaii is examined (which has four main peaks). Thus we progress from the simple, one bell-shaped ridge to the complex and real terrain of Hawaii.

4.2 Wave Generation Over Two Mountains

In order to better understand (and subsequently predict) nonlinear flows in regions of complex orography, we begin with a relatively simple case of two idealized circular peaks. The primary peak is identical to the idealized hill in the $Fr = 1/3$ case, but here a secondary, smaller peak is superimposed to the orography. Two cases are examined, one with the secondary peak located 50km downstream of the primary peak, and the other 50km upstream. In the first simulation, the primary peak is centered at 1/3 across the $x-$axis while the second peak is halfway along the $x-$axis. In the second simulation, their locations are reversed (the secondary peak is 1/3 along the $x-$axis). The second peak uses the same Eqn. (3.2) as the primary bell-shaped mountain, but with a mountain height h_0 of 1.5km and a half-width a of 10km. The orography is then formulated as $ht(x, y) = ht_{p1}(x, y)+ht_{p2}(x, y)$, where the subscripts $p1$ and $p2$ denote the primary and secondary bell-shaped orographic profiles, respectively. The amount of vertical levels in these cases is 300 so that the vertical resolution is about 100m. Otherwise, the WRF model is configured in exactly the same way as before, and run for the same amount of time of 6 hours. The atmospheric initial conditions are also the same as in the previous chapter.

Vertical cross-sections for the simulation where the secondary peak is located 50km downstream are are shown in Fig. 4.1 for WRF (top panel), FT_w (middle panel), and FT_o (bottom panel). Perhaps the most striking feature of the figures is that while just one wave train appears in the WRF and FT_w solutions, two wave trains are in FT_o. The FT_o solution, initialized at the surface with the vertical displacement field, is what we might expect if wave generation for both mountains were acting independently of each other, though in this

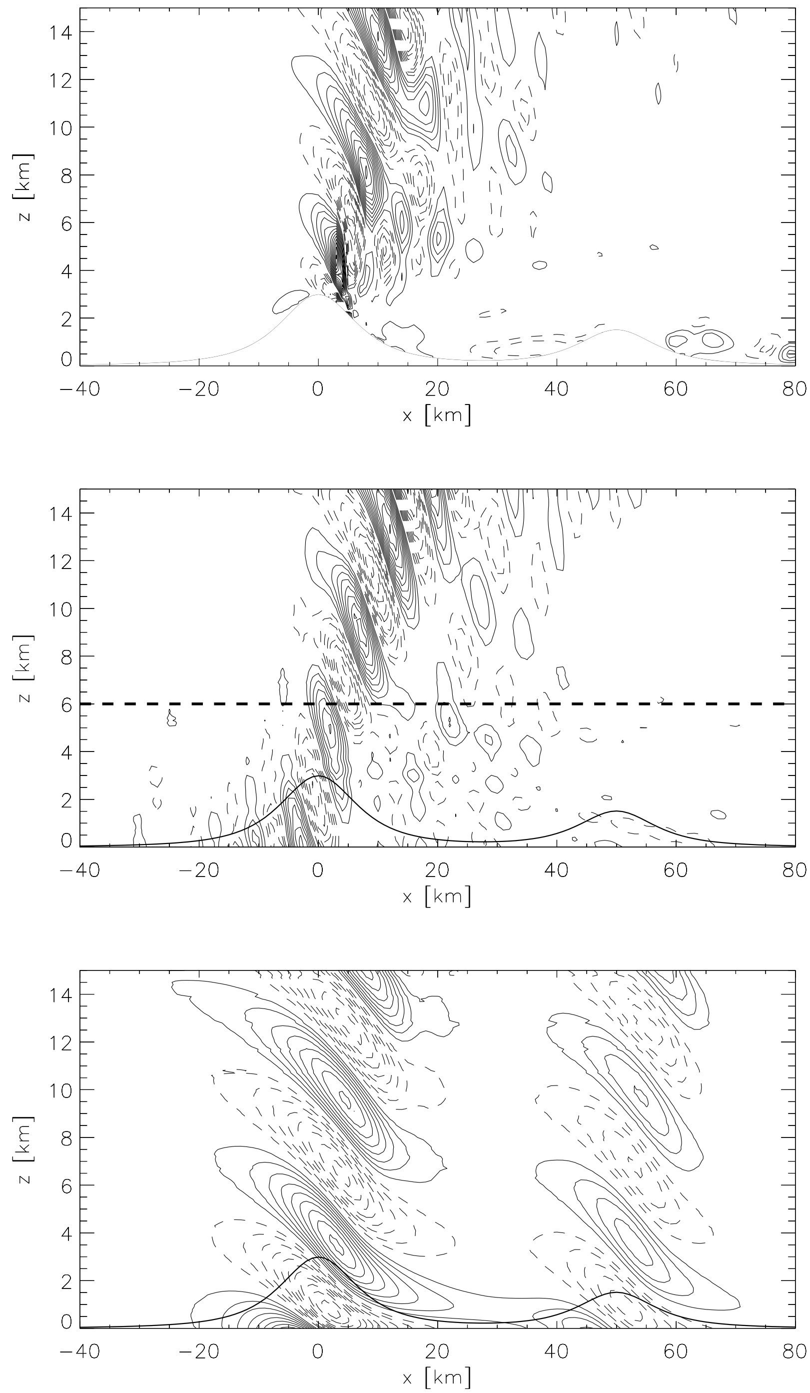

Figure 4.1: x-z vertical cross-sections for w taken at $y = 0$ (the centerline of the mountain) from WRF (top panel), FT_w (middle panel), and FT_o (bottom panel) for the first two mountain case. The dashed line in the middle panel indicates the FT_w initialization height, and the orographic height is shown by the line in both FT solutions. For all plots, w contour intervals are $0.3\mathrm{ms}^{-1}$ and negative contours are dashed. The zero contour is omitted.

case the WRF and FT_w results show that the upstream mountain is affecting (or inhibiting) the wave generating capabilities of the downstream mountain.

The dominant physical features of the lower atmospheric flow are examined more closely in Fig. 4.2. In the top panel, potential temperature contours of 0.5K are displayed along with reversed u flow in the shaded region (where $u < 0\mathrm{ms}^{-1}$). In the bottom panel, surface horizontal velocity streamlines are shown over the surface of the WRF domain. It can be seen that the secondary mountain lies entirely within the wake of the primary mountain, even though they are located 50km apart. An effective critical layer lies above the secondary mountain where u changes from negative to positive, and so any wave generation by the secondary peak is prevented from propagating to higher levels. As is shown by the potential temperature contours, the region above the secondary peak is stably stratified and so wave generation is theoretically possible.

The horizontally averaged $\rho\overline{uw}$ wave momentum flux is $0.109\mathrm{kgm}^{-1}\mathrm{s}^{-2}$ for FT_o, and $0.0174\mathrm{kgm}^{-1}\mathrm{s}^{-2}$ for FT_w, which is a difference of about an order of magnitude. In FT_o each mountain is almost independent of the other, and so the presence of two wave fields compounds the error of the the traditional linear approach. Even with the relatively large distance of 50km between the two peaks, in actuality the nonlinear low level flow has a large impact on the wavefield. The average flux in the FT_w simulation is similar to the corresponding value in in the $Fr = 1/3$ case, which is a further indication that only the primary mountain contributes to the average momentum flux.

Vertical cross-sections of w for the second simulation are shown in Fig. 4.3 for WRF (top panel), FT_w (middle panel), and FT_o (bottom panel). In this case, two wavefields are shown in all of the results. Gravity waves generated over the secondary mountain are not significantly affected by the low level nonlinear processes of the primary peak. This represents a substantial change from the first case, and also has implications for gravity wave parameterization schemes. The orographic generation of gravity waves is significantly

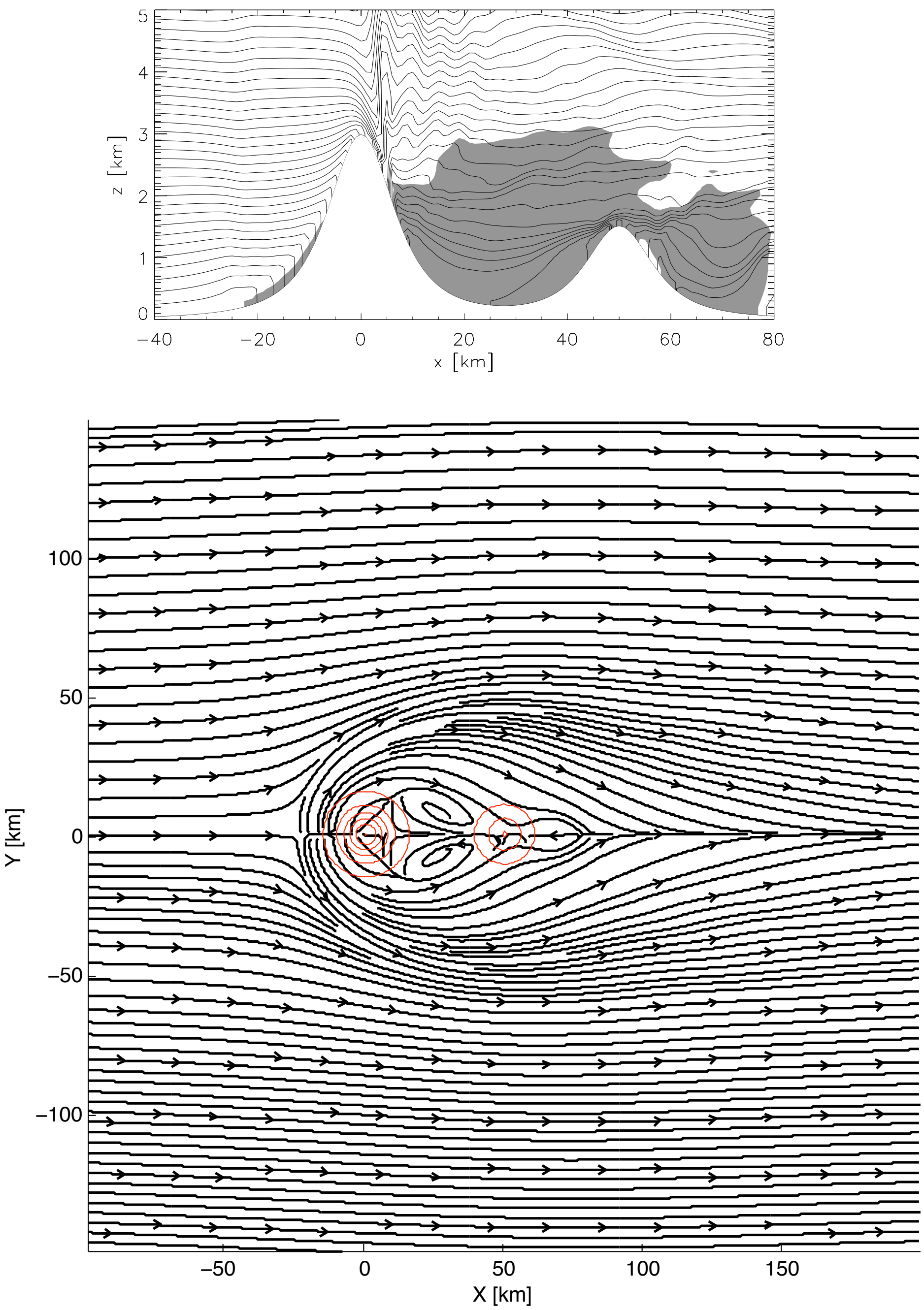

Figure 4.2: Top panel: an x-z vertical cross-section of θ and u from WRF for the two mountain case. Shaded regions are where $u < 0$ ms^{-1} and θ contour intervals are 0.5K. Bottom panel - horizontal velocity streamlines at the surface from WRF. The entire horizontal domain is shown. Orographic contours (in red) are 500m.

affected by the orographic structure as well as the background wind direction (i.e. consider an 180 degree change in the background wind direction for both of the simulations).

The horizontally averaged momentum flux further exemplifies how these differences should be accounted for in parameterization schemes. The averaged $\rho\overline{uw}$ wave flux is $0.109\mathrm{kgm}^{-1}\mathrm{s}^{-2}$ for FT_o, and $0.0257\mathrm{kgm}^{-1}\mathrm{s}^{-2}$ for FT_w. While the FT_o average is the same as before, FT_w experiences a substantial increase. It should be noted that while in this case the average FT_w momentum flux is greater than its corresponding value in the previous case, it still is not as much as the combined momentum flux averages of both the $Fr = 1/3$ and $Fr = 2/3$ cases. This would indicate that the two peaks still do not act independently of each other, and that nonlinear low level processes of one (or both) peaks affect the other peak(s).

These results bring into question the dividing streamline height applicability to wave generation in complex terrain, given that adjacent peaks have the potential to affect one another through low level nonlinear processes. In the first simulation the second peak is located 50km downstream of the first peak, but is nevertheless in the wake region of the primary peak. Wave propagation to the upper atmosphere and any momentum flux contributions from the secondary peak should therefore be considered negligible. Of course this will not be the case if the initial wind direction is from another direction, as the secondary peak might not be affected by the lower atmospheric nonlinear flow around the primary peak. Therefore, the low level nonlinear flow around complex orography affects the wave generation ability of individual peaks, but the initial wind direction is also a contributing factor. We examine these effects in more detail in the next section, where wave generation is studied over the Big Island of Hawaii.

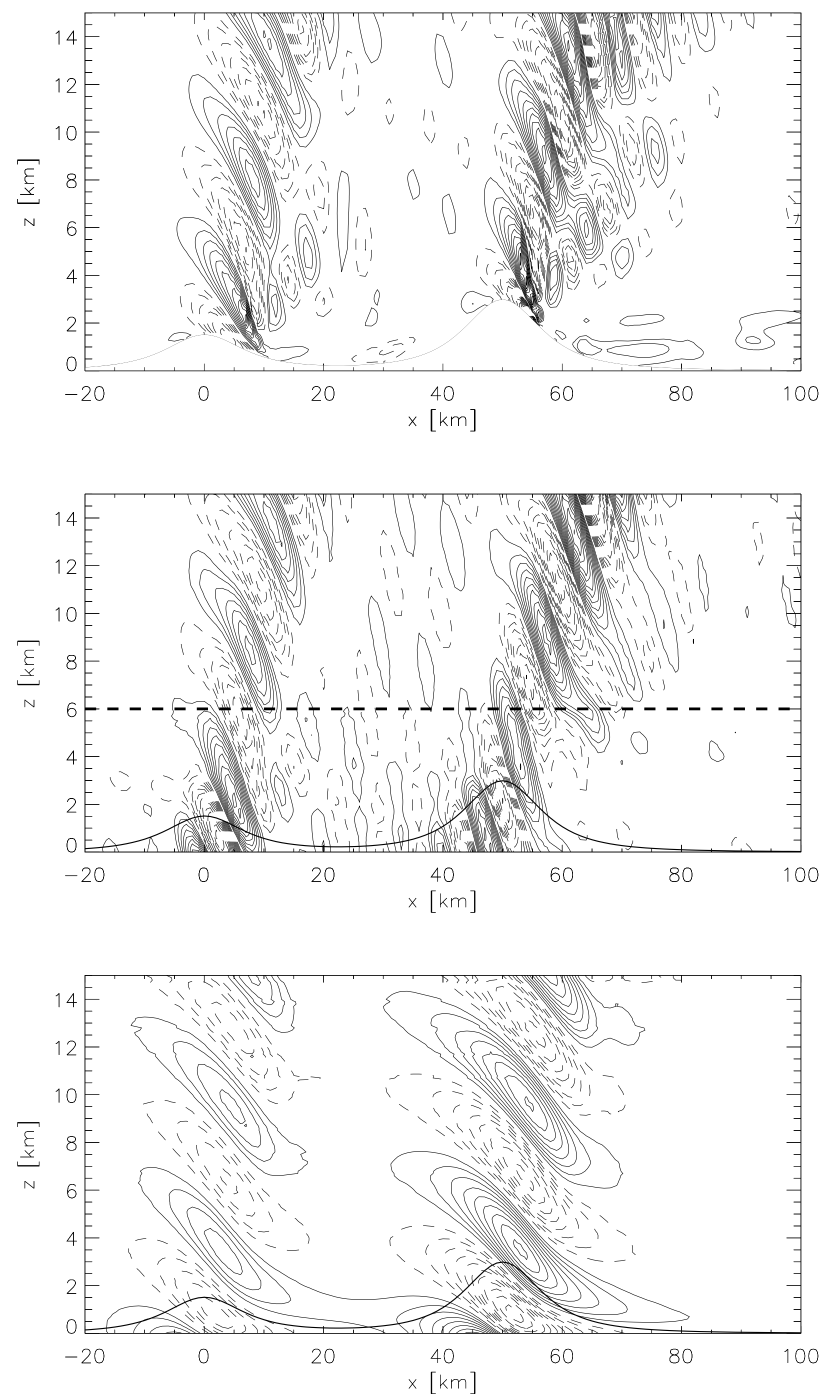

Figure 4.3: x-z vertical cross-sections for w taken at $y = 0$ (the centerline of the mountain) from WRF (top panel), FT_w (middle panel), and FT_o (bottom panel) for the second two mountain case. The dashed line in the middle panel indicates the FT_w initialization height, and the orographic height is shown by the line in both FT solutions. For all plots, w contour intervals are $0.3\mathrm{ms}^{-1}$ and negative contours are dashed. The zero contour is omitted.

4.3 Idealized Simulations of Hawaii

One of the objectives of this dissertation is to assess the viability of FT to reproduce the wavefield in a nonlinear complex orographic flow regime, and so we believe that Hawaii is well suited for this experiment. The big island to Hawaii (hereafter referred to as Hawaii) is a volcanic island with two peaks over 4km, thus creating the potential for frequent low Froude number flow events. The orography around the island is fairly complex, as in addition to the taller peaks there are two lesser peaks theoretically capable of generating wavefields. In addition, Hawaii's location in the trade wind latitudes gives it a fairly consistent and well documented weather pattern.

Fig. 4.4 shows the terrain of Hawaii, in 500m contours. The orography of Hawaii appears to be more reminiscent of complex orographic regions such as the Alps than of elongated large ridges such as the Rockies. We might then suppose that Hawaii would generate the intermittent small-wavelength and reduced amplitude wavefields observed in PYREX and MAP, rather than the large amplitude breaking wave regimes more characteristic over Boulder, CO and Greenland. These considerations must be taken into account when representing the orography numerically - the MAP experiments found that the horizontal resolution is especially important.

Relevant information about Hawaii's climate can be found in Smolarkiewicz et al. (1988) and Rasmussen et al. (1989), where a relatively consistent Froude number of 0.2 is estimated for Hawaii's tallest peaks. The climate of Hawaii does not vary much over the year, with typically east-northeasterly trade winds dominating the flow. Orographically-enhanced precipitation effects have been the focus of several investigations (Rasmussen et al., 1989, 1993; Smolarkiewicz et al., 1988; Hafner and Xie, 2003; Wang et al., 1998, and Chen and Feng, 2001). Other research efforts have analyzed downslope windstorms (Zhang et al., 2005; Wang et al., 1998). The wake region of Hawaii has been studied by Smith and Grubisic

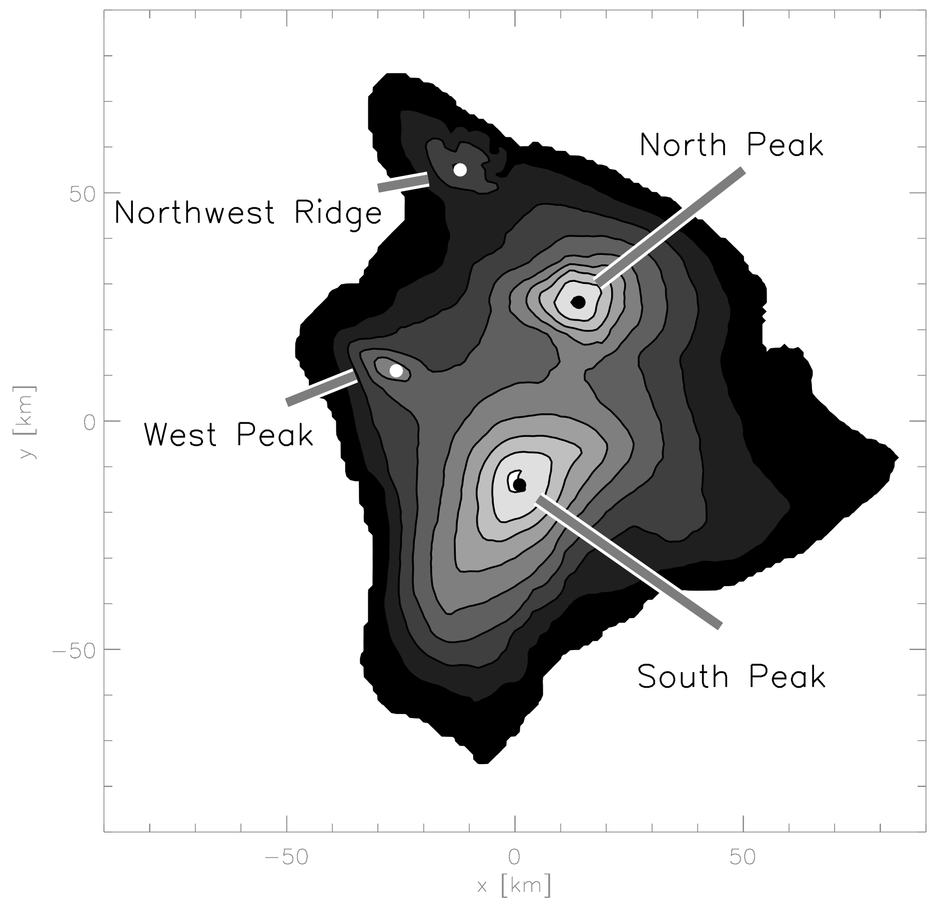

Figure 4.4: Contour plot of Hawaii's Big Island. Intervals are 500m, and the four major peaks are labeled.

(1993), Hafner and Xie (2003), and Xie et al. (2001), who note that Hawaii's wake region affects ocean currents and air-sea interactions as far as 3000km downstream.

Fig. 4.5 is a schematic from Smith and Grubisic (1993) based on observations of the flow field near the surface of Hawaii. A stagnation point is located just upstream of Hawaii near a low-level convergence zone that generates convection and clouds. Zones of accelerated airflow are located near the northern and southern tips of the island, while a large wake region extends downstream of Hawaii. Two main vortices have been observed which are

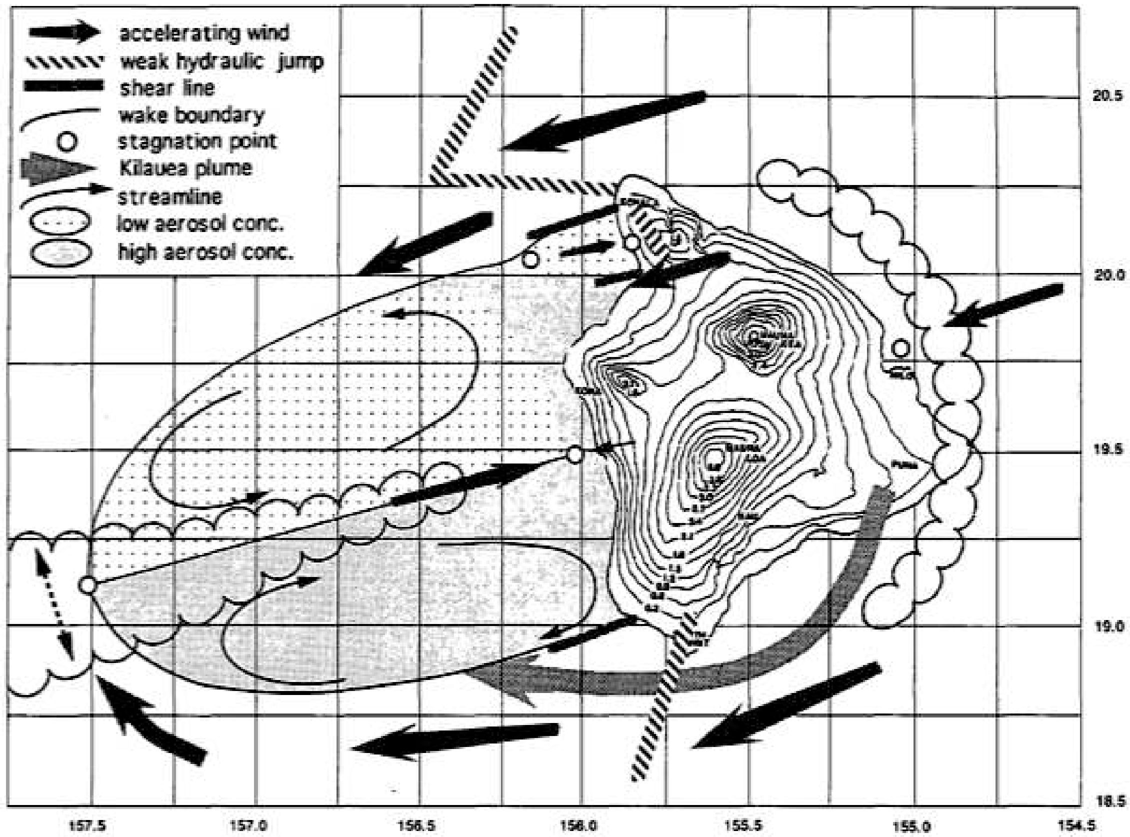

Figure 4.5: Schematic of the low-level flow around Hawaii. Prominently featured are the cloud bands (upstream of the island and between the vortex pair), flow streamlines in the vortices, and accelerating winds and hydraulic jumps concentrated to the north and south of Hawaii. The Kilauea plume is shown by the gray-shaded (and largest) arrow originating at the southeast corner of Hawaii. Ash from this plume becomes concentrated in the southern vortex (from Smith and Grubisic (1993)).

characterized as 'quasi-steady', as they are suspected to dominate the wake. The 'Kilauea plume' arrow is a volcanic dust plume that originates at the beginning of the arrow. The plume is then advected around the island, as shown by the arrow, and then flows into the southern vortex, which has a higher concentration of plume dust than the northern vortex. Weak hydraulic jumps were also observed on the north and south ends of Hawaii. A cloud band located in a low-level convergence zone between the two downstream vortices was also observed.

Given Hawaii's impact on the local, regional, and even global weather and oceanographic systems, it must asked whether Hawaii is adequately represented in global weather and climate models. For example, NCEP's GFS (Global Forecasting System) model has a horizontal resolution of 35km, and the maximum elevation as represented in the model is less than one-tenth of Hawaii's actual summit height. GFS cannot explicitly capture orographic drag effects, the the reduced height means that the low level flow regime effectively is linear with $Fr_h = 2$. Global weather models typically cannot resolve gravity wave drag, and so a quantitative assessment of gravity wave drag is essential in that region.

Many gravity wave drag parameterization schemes are based upon the predictions of linear theory, and as we have seen in section 4.2 nonlinear flows not only have an effect on the gravity wave field, but neighboring mountains can be affected by low-level nonlinear processes. In addition, the prevailing wind direction might play an important role in which mountain peaks generate wave fields. Although Hawaii usually has a consistent wind direction, we examine the wave field sensitivity of the island to the background wind direction. Nonlinear effects on the momentum fluxes are further examined in this section, to analyze the significance of the departure of results from FT_w and corresponding FT_o predictions.

We currently introduce some 'dissertation-speak' to denote the four peaks of Hawaii for convenience, as they will be frequently mentioned in the results. The mountain furthest to the northwest, which is shaped more like a ridge than an actual peak, will henceforth be termed the NW ridge. The two tallest peaks over 4km in height are called the 'north peak' and 'south peak', respectively, and the mountain peak located near the central western edge of the island is called the 'west peak'. See Fig. 4.4 for the locations of each mountain.

4.3.1 Case I - ENE Wind

We attempt to resolve some of these issues with three high-resolution idealized simulations of Hawaii. The initial background wind direction is changed for each simulation, but otherwise everything else is kept the same. As before, the WRF model has a 300 x 300 x 300 grid which is 1km resolution in the horizontal and about 100m resolution in the vertical. The sponge layer begins at $z = 15$km. The model is run for 6 hours with no diabatic or Coriolis effects. The simulation has a characteristic Froude number of 0.2 (for Hawaii's tallest peak), and with $N = 0.01\text{s}^{-1}$, the wind magnitude is 8.3ms^{-1}. For the first case, the wind is east-northeasterly, and so $U = -7.51\text{ms}^{-1}$ and $V = -3.11\text{ms}^{-1}$. FT_w is initialized by WRF at 6km height, above the low-level nonlinear flow field.

A horizontal cross-section of w at 14km from WRF is shown in the upper left panel of Fig. 4.6. Four areas of intense wave activity are highlighted by the boxes. In these boxes w attains magnitudes of at least 2ms^{-1}. Downstream of the boxes, interactions among the wave fields have created large, seemingly random wave patterns of less intensity. The first box is located off the northernmost peak, which is an elongated-ridge structure (denoted as the NW ridge). In this box, the wave field at 14km is almost entirely over the water, in the left upper quadrant of the NW ridge.

The two central boxes are located just downstream of the north and south peaks, which are approximately circular in shape. The last, southernmost box is associated with the ridge which extends southward from the south peak. All of the wave fields in the boxes share similar characteristics in terms of their wavelengths and wave amplitudes. The wavelengths are in the range of $10 - 15$km, which is similar to the wavelengths observed over the Alps in the MAP field experiments (section 1.4.2). Perhaps of equal interest is the lack of a wave field over the west peak, as in for this particular flow regime it is located in the lee of the north peak. A one-dimensional vertical profile of the horizontal wind components

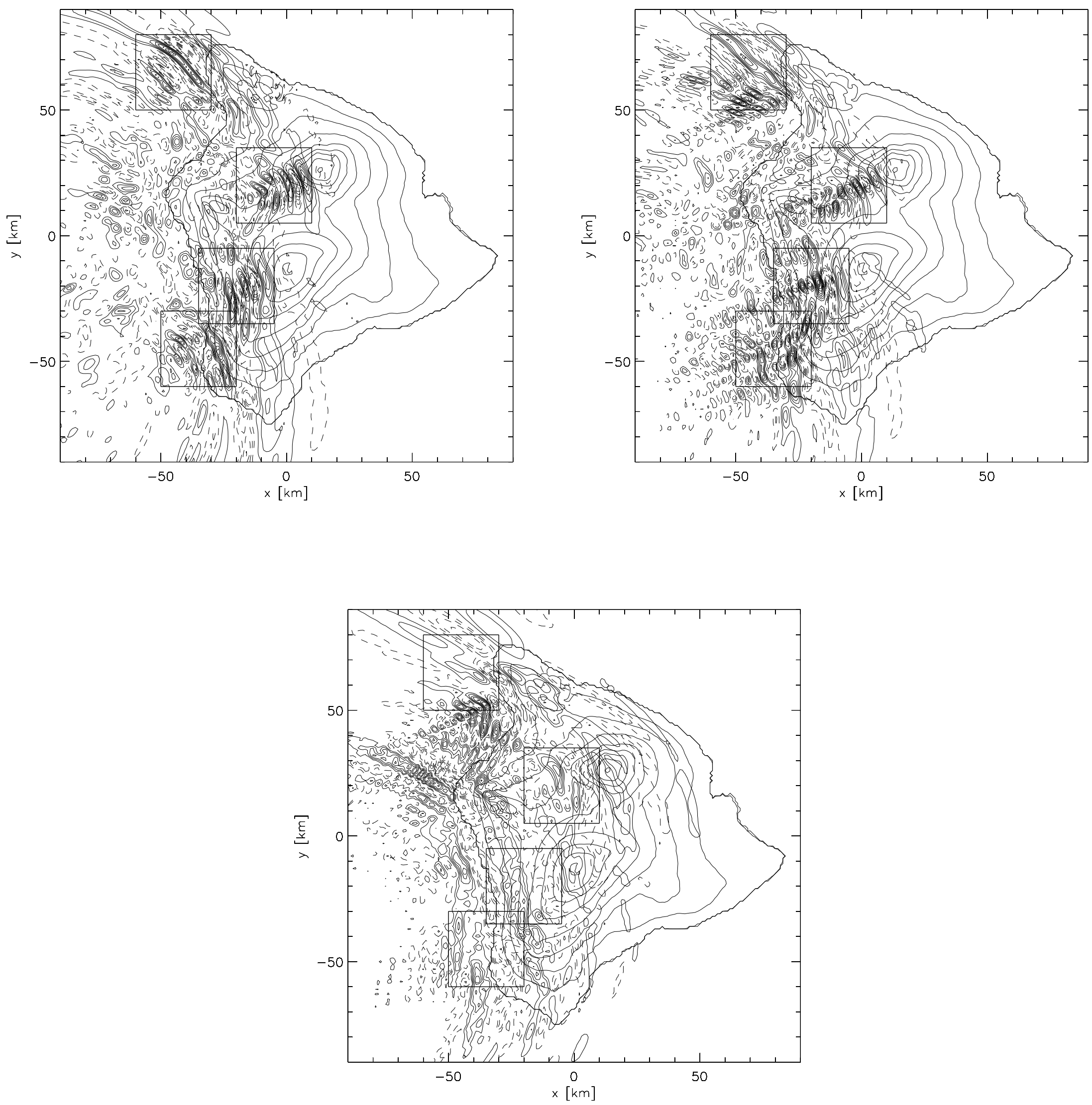

Figure 4.6: 14 km horizontal cross-section of w over Hawaii from WRF (upper left panel), FT_w (upper right panel), and FT_o (lower panel) for the ENE Case. Areas of intense w wave activity as predicted by WRF are located within the boxes. Contour intervals are $0.3ms^{-1}$, negative contours are dashed, and the zero contour is omitted.

above the west peak is shown in Fig. 4.8. The relatively weak velocity magnitudes in the lowest kilometer, and their subsequent increase at higher altitudes, suggests that any wave generation is likely to be trapped.

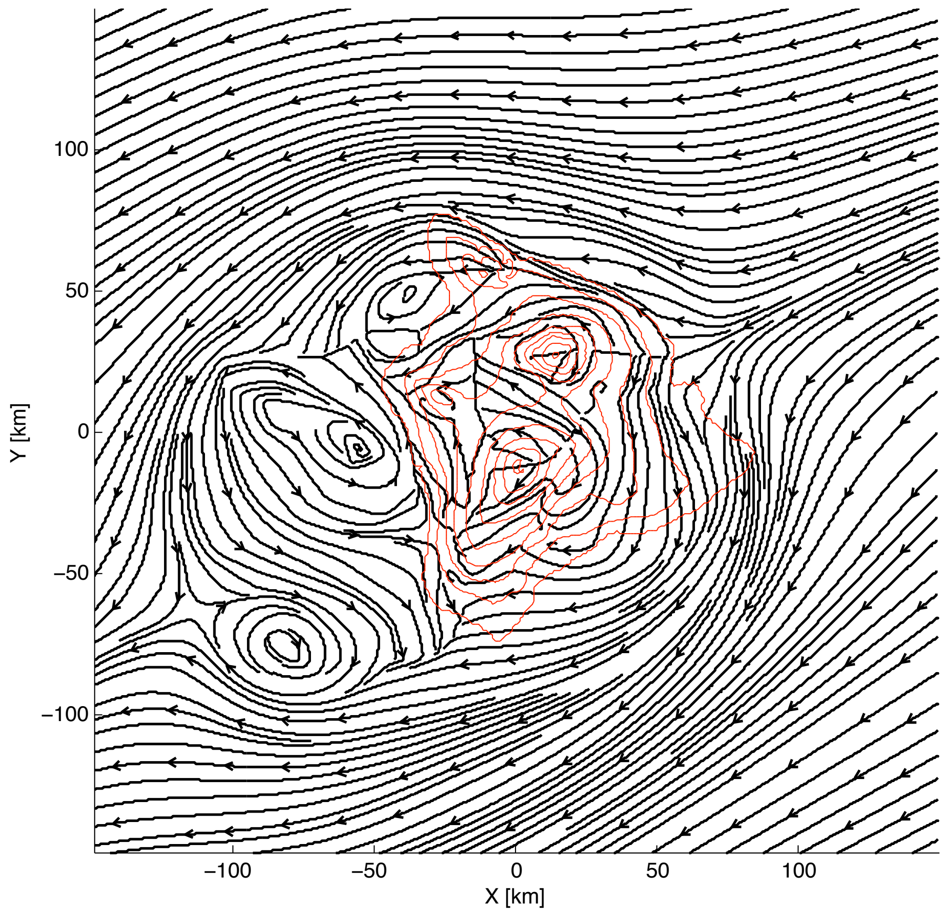

Figure 4.7: Horizontal velocity streamlines along the surface from WRF for the ENE Winds case. Orographic contours (in red) are 500m.

A plot of the surface horizontal streamlines is shown in Fig. 4.7. The surface flow is in general qualitative agreement with the schematic in Fig. 4.5 of Smith and Grubisic (1993). The upstream flow splits around Hawaii, and vortices are evident in the lee of the island. The streamlines are also in agreement with the volcanic plume trajectory around the southern portion of Hawaii. The surface streamlines follow the valley between the northwest ridge and the northern peak. A major difference is that the lee vortex pair does not extend as far as depicted in the schematic, but that is due to the fact that the model was only run for 6 hours. If the WRF model were run over a longer time, the vortices would continue their

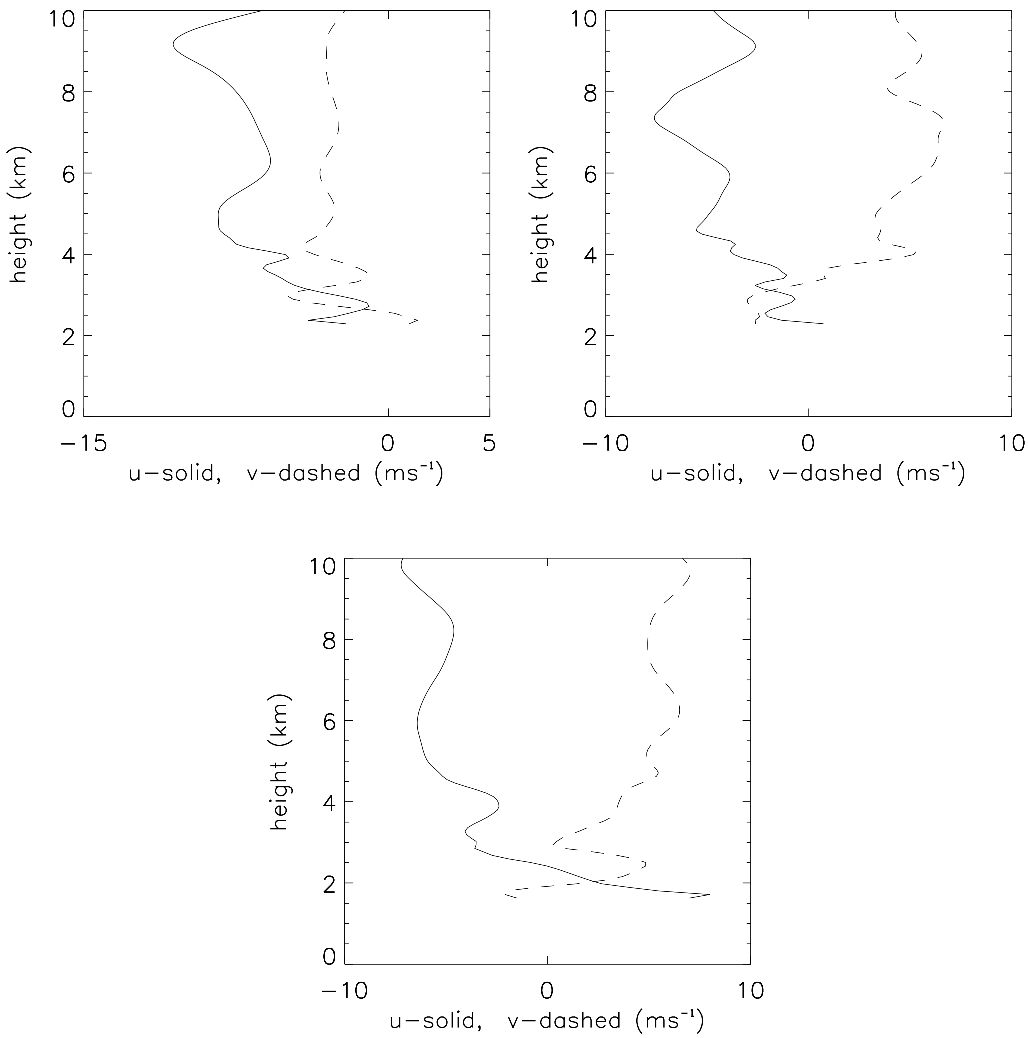

Figure 4.8: 1D vertical profiles of the horizontal wind components over the west peak for the ENE case (upper left panel), the west peak for the SE case (upper right panel), and the northwest ridge for the SE case (lower panel).

march on their west-southwest trajectory, eventually reaching the model lateral boundaries. It is also unclear if the lee of the island would be dominated by two primary vortices, or be more characteristic of the alternating vortex structure shown in Fig. 1.6 off Galapagous island.

FT_w initialized at 6km is shown in the upper right panel of Fig. 4.6. The dominant wavefields closely resemble those from WRF. The geographical areas of the most intense wave activity predicted by FT_w are also located in the boxes. Their wavelengths and amplitudes are similar to those from WRF. Waves are absent in the west peak, as is consistent with the WRF solution. The corresponding w solution from FT_o at 14km is shown in the lower panel. The placement of the overall wave field is much different from WRF and FT_w. The most intense wave activity is off the west coast of Hawaii, particularly over the northern half. Wave activity located close to the west peak in FT_o is not reproduced by the other two solutions, and waves are largely absent from the southern two boxes. Interestingly the dominant wavelengths and amplitudes in FT_o are similar to the other two solutions - the placement of those waves is off, however.

The wavefield near the NW peak is presently examined in more detail, as we are interested to see whether the wave generation from the peak is independent of the low level nonlinear behavior caused by the island as a whole. A close-up of w over the NW peak from WRF is shown in the upper left panel of Fig. 4.9 An additional idealized WRF simulation was then conducted to find out whether a similar wave pattern can occur with an isolated ridge as the wave generating mechanism. The set-up of this particular WRF simulation was identical to the others, except that the orography of Hawaii was replaced with an idealized ridge of the shape:

$$h(x,y) = \frac{h_m}{(1 + ((x - x_0)/a)^2 + ((y - y_0)/b)^2)^{3/2}}. \tag{4.1}$$

Here, the idealized ridge height h_m is 1.5km (same as the actual ridge height), $a = 7.5$km, $b = 17$km, and the ridge is rotated 55 degrees to the left from its north-south orientation. The corresponding w field from the idealized WRF simulation, shown in the bottom panel of Fig. 4.9, is in good qualitative agreement with the wave field over the NW ridge. This

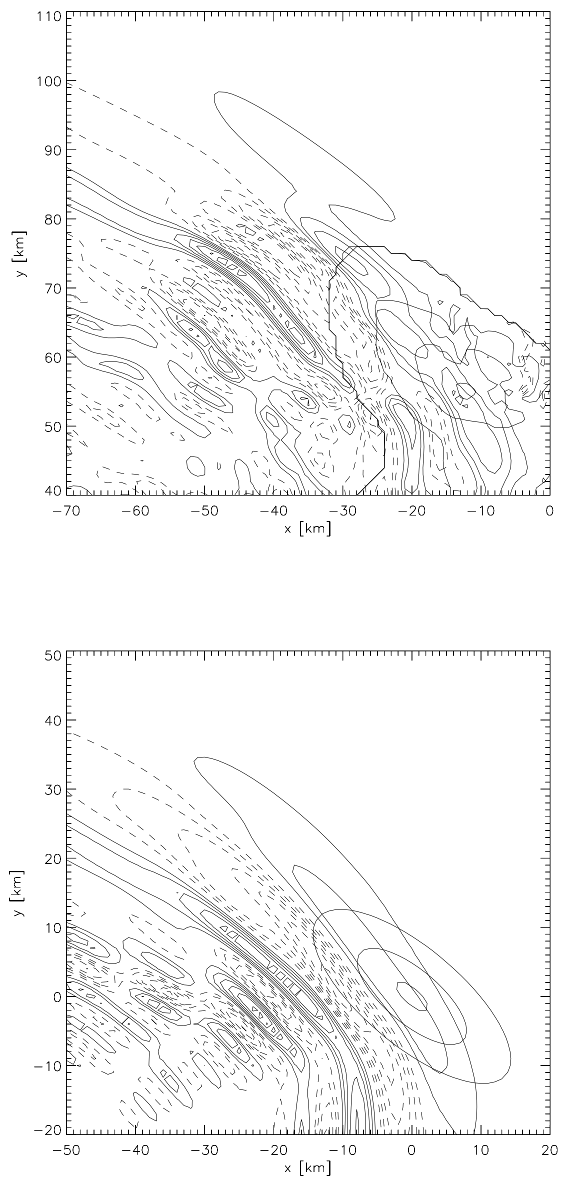

Figure 4.9: Top panel - Close-up of Fig. 4.6 over the NW ridge, showing the WRF w field at 14km. Bottom panel - WRF w solution at 14km for the idealized ridge that is meant to resemble the NW ridge. Contour intervals are $0.3\mathrm{ms}^{-1}$, negative contours are dashed, and the zero contour is omitted.

would indicate that wave generation over the ridge is acting independently of Hawaii as a whole.

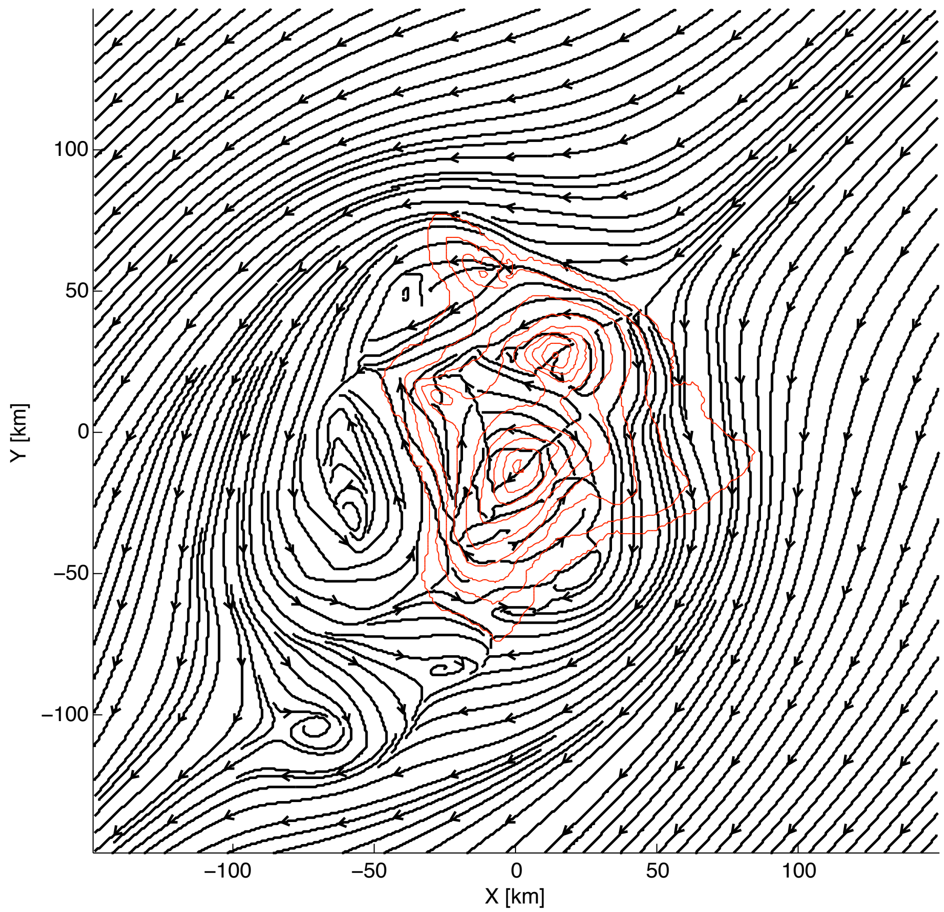

Figure 4.10: Horizontal velocity streamlines along the surface from WRF for the NE Winds case. Orographic contours (in red) are 500m.

4.3.2 Case II - NE Wind

The sensitivity of the wave field to the wind direction is shown for this next case when the prevailing wind direction is from the northeast - a change of 22.5 degrees. Surface horizontal streamlines from WRF are shown in Fig. 4.10. There is no significant departure in the overall streamline field from the previous case.

The same thing cannot be said of the w field over Hawaii, however. A horizontal cross-sections at 14km from WRF is shown in the upper left panel of Fig. 4.10. As in the previous case, areas of significant wave activity are highlighted in the boxed areas. In contrast to the previous case, gravity wave generation is occurring over the west peak. Wave generation continues to occur over the north peak and the northwest ridge. There also appears to be some phase alignment between the two mountains, as the upstream flow is impinging on a more normal direction to them. No significant wave activity is evident over the south peak or its associated ridge. This might be due to the deflection of the flow around the north peak, which substantially weakens the ability of the south peak to generate wave activity.

Another interesting feature of the wave field over Hawaii is the wave-intense region over the southeast coast. This does not appear to be associated with any of the peaks, but is probably due to the flow splitting around Hawaii. As can be seen in the surface stream plot in Fig. 4.10, the surface streamlines impacting the northern peak are deflected to the left and right. The leftward-deflected streamlines flow over the northeast region of Hawaii before descending $1-1.5$km back towards the ocean. Gravity waves are generated over this descending region of air. The surface streamlines indicate that low level forcing is more intense for this case than in the ENE case.

Corresponding plots of FT_w and FT_o are shown in the upper right and lower panels of Fig. 4.11, respectively. As before, FT_w manages to recreate the wave field at 14km remarkably well, with the most intense wave activity appearing in the 4 boxes. The wave field result from FT_o does not resemble the WRF solution so much, however. Although FT_o captures the wave field over the NW ridge and the west peak, only weak wave activity is apparent over the northern peak, and almost no wave activity is detected in the boxed region over southeast Hawaii. The lack of wave activity over the southern peak is in agreement with WRF, but most likely is due to the relatively gentle slope to the southwest of that particular peak which would not create large w values at the lower boundary. These results further emphasize the importance of lower atmospheric nonlinear processes on wave generation. Additionally, the sensitivity of the wave field to minor changes in the wind direction is also important to consider with respect to gravity wave parameterization schemes.

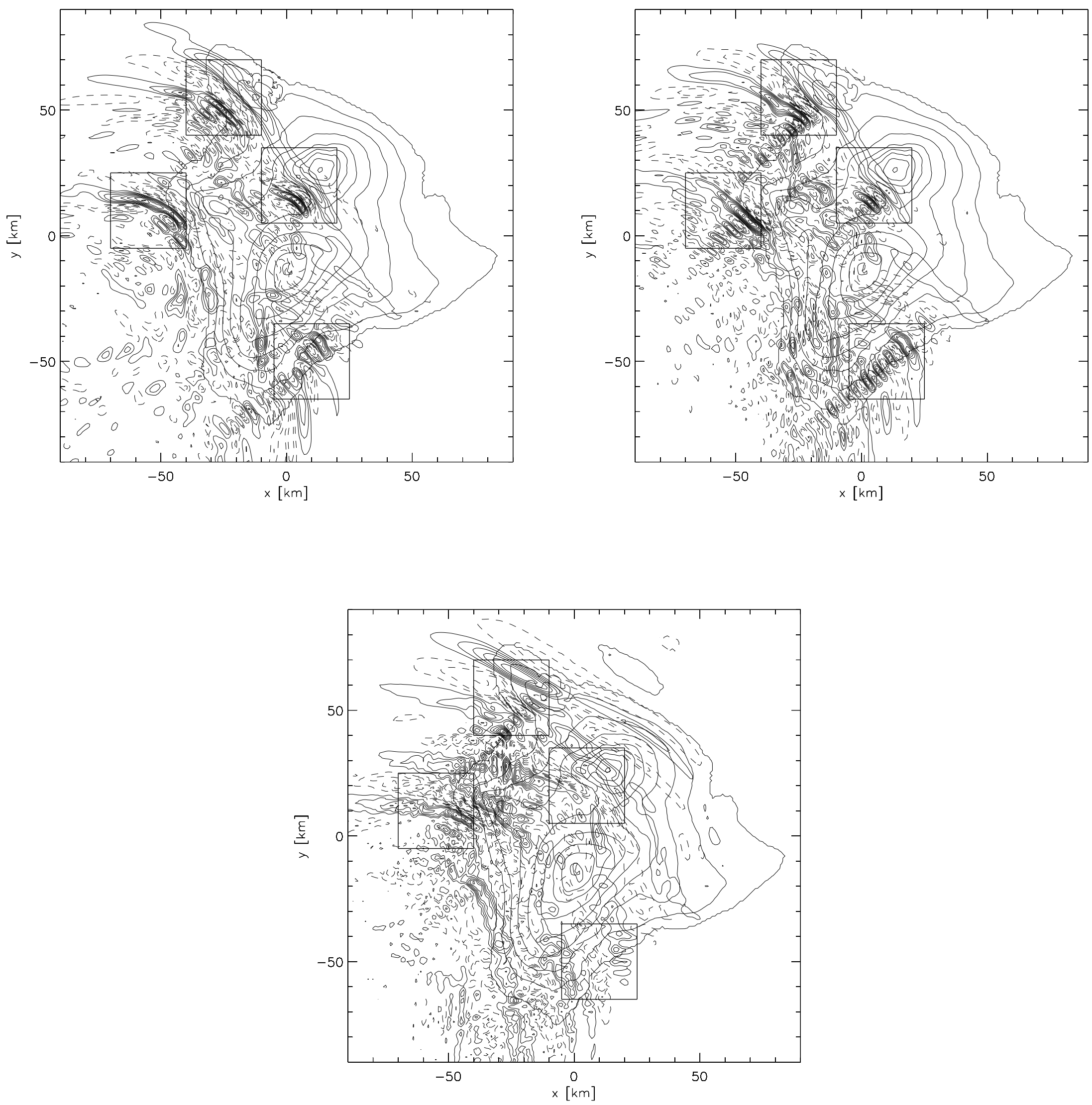

Figure 4.11: 14 km horizontal cross-section of w over Hawaii from WRF (upper left panel), FT_w (upper right panel), and FT_o (lower panel) for the NE Case. Areas of intense w wave activity as predicted by WRF are located within the boxes. Contour intervals are $0.3\mathrm{ms}^{-1}$, negative contours are dashed, and the zero contour is omitted.

As a continuation of our idealized experiment on the NW ridge, an additional WRF simulation was done with the terrain shape from Eqn. (4.3.1) and the northeasterly background wind flow. The w field around the NW ridge and the idealized ridge is shown in the

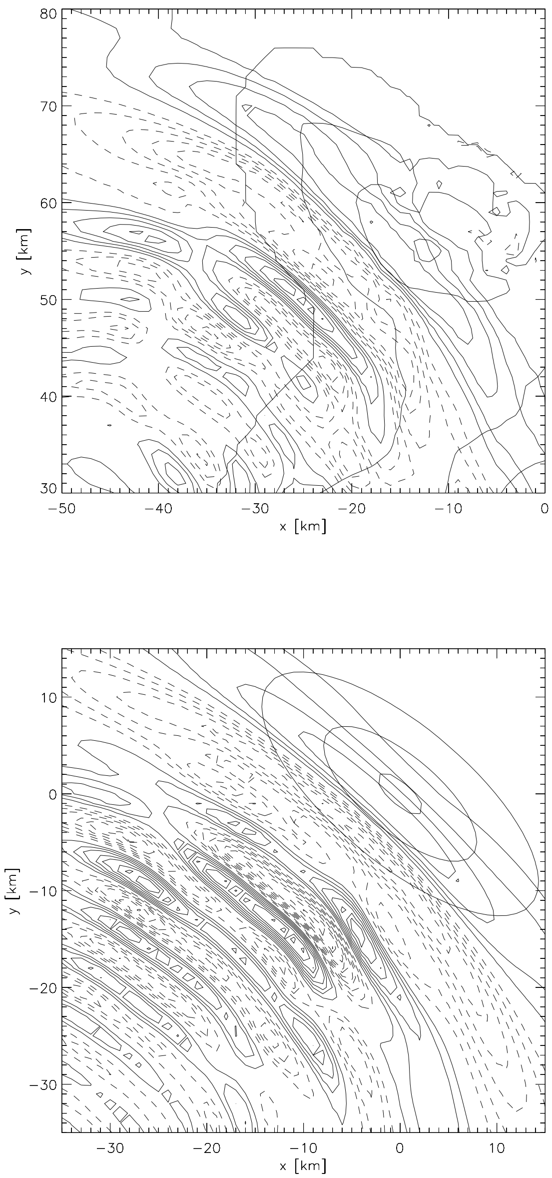

Figure 4.12: Top panel - Close-up of Fig. 4.11 over the NW ridge, showing the WRF w field at 14km. Bottom panel - WRF w solution at 14km for the idealized ridge that is meant to resemble the NW ridge. Contour intervals are 0.3ms^{-1}, negative contours are dashed, and the zero contour is omitted.

top and bottom panels of Fig. 4.12. The wave field from the idealized ridge appears similar to the corresponding wave field in the WRF simulation, but not so much as in the east-northeasterly case. Hence, there could be some low level processes associated with other parts of Hawaii affecting wave generation. Therefore, the idea that the ridge is a single mountain shape unaffected by Hawaii might lose some of its merit when the prevalent wind direction is from the northeast.

4.3.3 Case III - SE Wind

The initial background wind direction is from the southeast for this final case study. Horizontal cross-sections of w at 14km are shown in Fig. 4.13 for WRF (upper left panel), FT_w (upper right panel), and FT_o (lower panel). In the WRF result, much of the wave activity occurs over the north and south peaks. The areas of most intense wave activity, located just to the northwest of the tallest peaks, are boxed-in. In contrast, no wave activity is seen over the west peak or the northwest ridge, which are both located directly downstream of the north and south peaks. As can be seen in the surface horizontal streamline plot in Fig. 4.14, the lee vortices in this case extend to the northwest and have a large impact on the ability of the two smaller peaks to generate gravity waves.

One-dimensional vertical profiles of the horizontal wind components are shown in Fig. 4.8 for the west peak (upper right panel) and the northwest ridge (lower panel). In both plots, it can be seen that the u and v wind components change sign with altitude. This is indicative of a critical level which would absorb any waves being generated from either peak.

Both FT solutions are consistent with the earlier cases, with FT_w more accurately resembling the WRF solution. FT_o predicts wave activity associated with the two lesser peaks, which in reality is nonexistent. FT_o also erroneously predicts wave activity near the southeast coast. For this case in particular, FT_o seems to over-predict wave activity that, in reality, is not being generated because of low-level nonlinear processes.

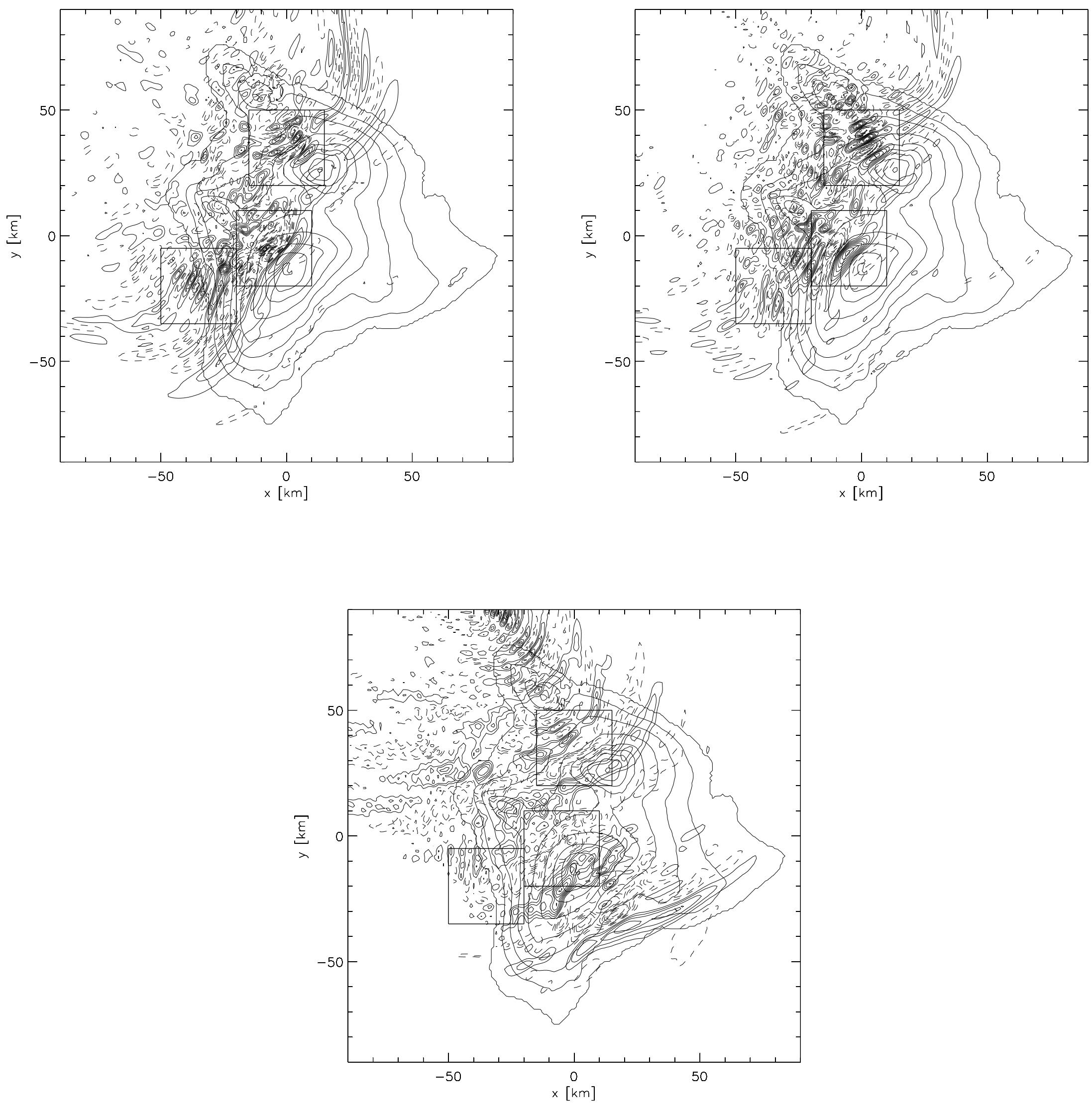

Figure 4.13: 14 km horizontal cross-section of w over Hawaii from WRF (upper left panel), FT_w (upper right panel), and FT_o (lower panel) for the SE Case. Areas of intense w wave activity as predicted by WRF are located within the boxes. Contour intervals are $0.3\mathrm{ms}^{-1}$, negative contours are dashed, and the zero contour is omitted.

This last case, along with the two mountain case in section 4.2, raise an important issue concerning global weather modeling efforts. The distance between the upstream and downstream peaks in the Hawaii SE winds case is about 40km, which is a greater distance than

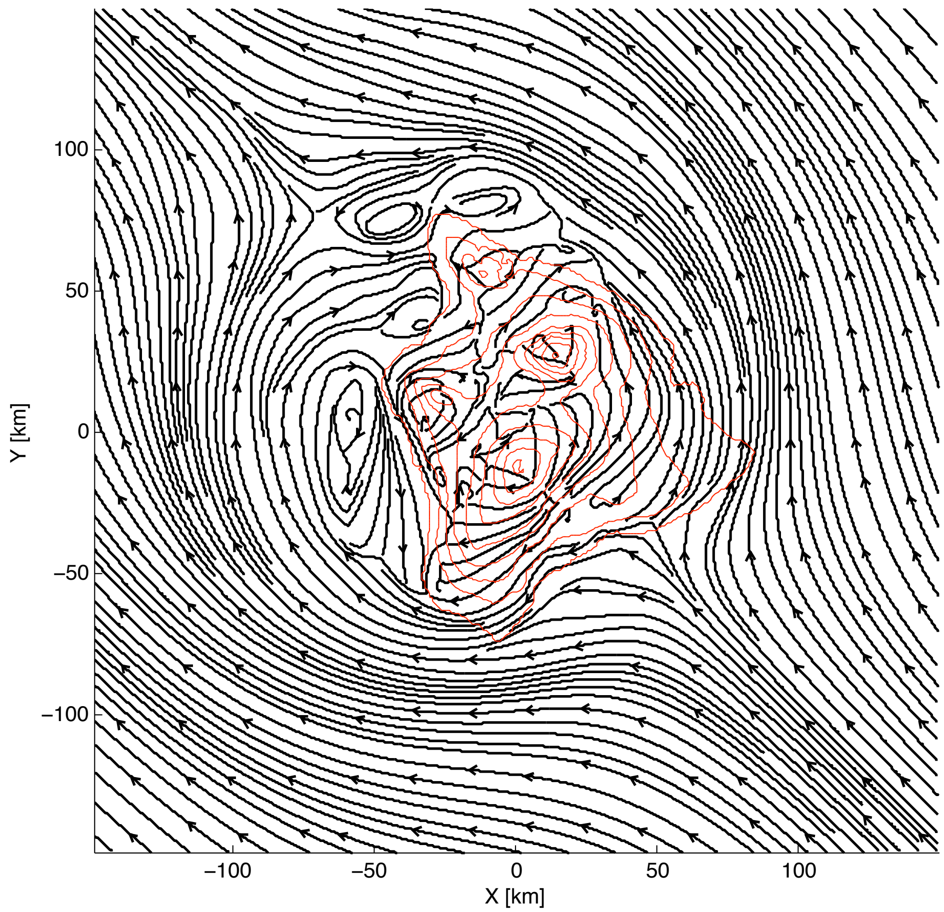

Figure 4.14: Horizontal velocity streamlines along the surface from WRF for the SE Winds case. Orographic contours (in red) are 500m.

the horizontal resolution of some of today's global weather models. The lower atmospheric effects (lee vortex shedding) would effectively extend over several grid points of a weather model, but would not be resolved and instead predict a linear flow regime over Hawaii. Nonlinear effects being generated over one region will have to be accounted for in another region of a global model, so that sub-grid scale processes in the grid points are no longer independent of each other.

All of the Hawaii cases have also exemplified the sensitivity of wave generation to wind direction. In the three cases shown, where the total change in the wind direction was just 90 degrees, wave generation off the peaks was primarily dependent on whether or not the peak was located within the wake of another peak. The west peak, for instance, only generated waves in one of the cases while waves were generated by the north peak in all three cases.

4.4 Momentum Fluxes for the Hawaii Cases

The wave momentum fluxes $\rho\overline{uw}$ and $\rho\overline{vw}$ are calculated for each of the Hawaii cases. There are three main issues to be addressed in this section: (i) by how much do the horizontally averaged momentum fluxes in FT_w differ from those calculated by FT_o, (ii) is there any sensitivity to the averaged momentum fluxes to the initial background wind direction, and (iii) where are the fluxes most likely to be concentrated for each of the cases. For all of these cases, the horizontally averaged momentum flux is independent of the vertical level. This is the same as in the previous results, and is consistent with linear theory.

Horizontal cross sections at 14km of the wave momentum fluxes for the ENE case are shown in Fig. 4.15 for $\rho\overline{uw}$ predicted by FT_w (top left panel), FT_o (top right panel), and for $\rho\overline{vw}$ from FT_w (bottom left panel) and FT_o (bottom right panel). Note the difference in scaling between the FT_w and FT_o results, where FT_w contours are 1/5 as large in magnitude as FT_o. Much of the wave flux activity in both results is well correlated in the same regions of significant w values. For both FT methods the regions of intense wave flux activity are localized, and only affect relatively small areas of the horizontal domain.

The horizontally-averaged wave $\rho\overline{uw}$ flux for FT_w is around $0.051\mathrm{kgm}^{-1}\mathrm{s}^{-2}$, while in FT_o it is $0.63\mathrm{kgm}^{-1}\mathrm{s}^{-2}$. The corresponding averaged $\rho\overline{vw}$ flux is $0.020\mathrm{kgm}^{-1}\mathrm{s}^{-2}$ for FT_w and $0.13\mathrm{kgm}^{-1}\mathrm{s}^{-2}$ for FT_o. Low level nonlinear processes are a very significant factor in the wave flux magnitudes as the discrepancy between the FT methods is by an order of magnitude. Nonlinear processes such as flow splitting and lee vortex formation are causing the effective amplitude of the mountains to be reduced, thereby reducing wave momentum flux contributions.

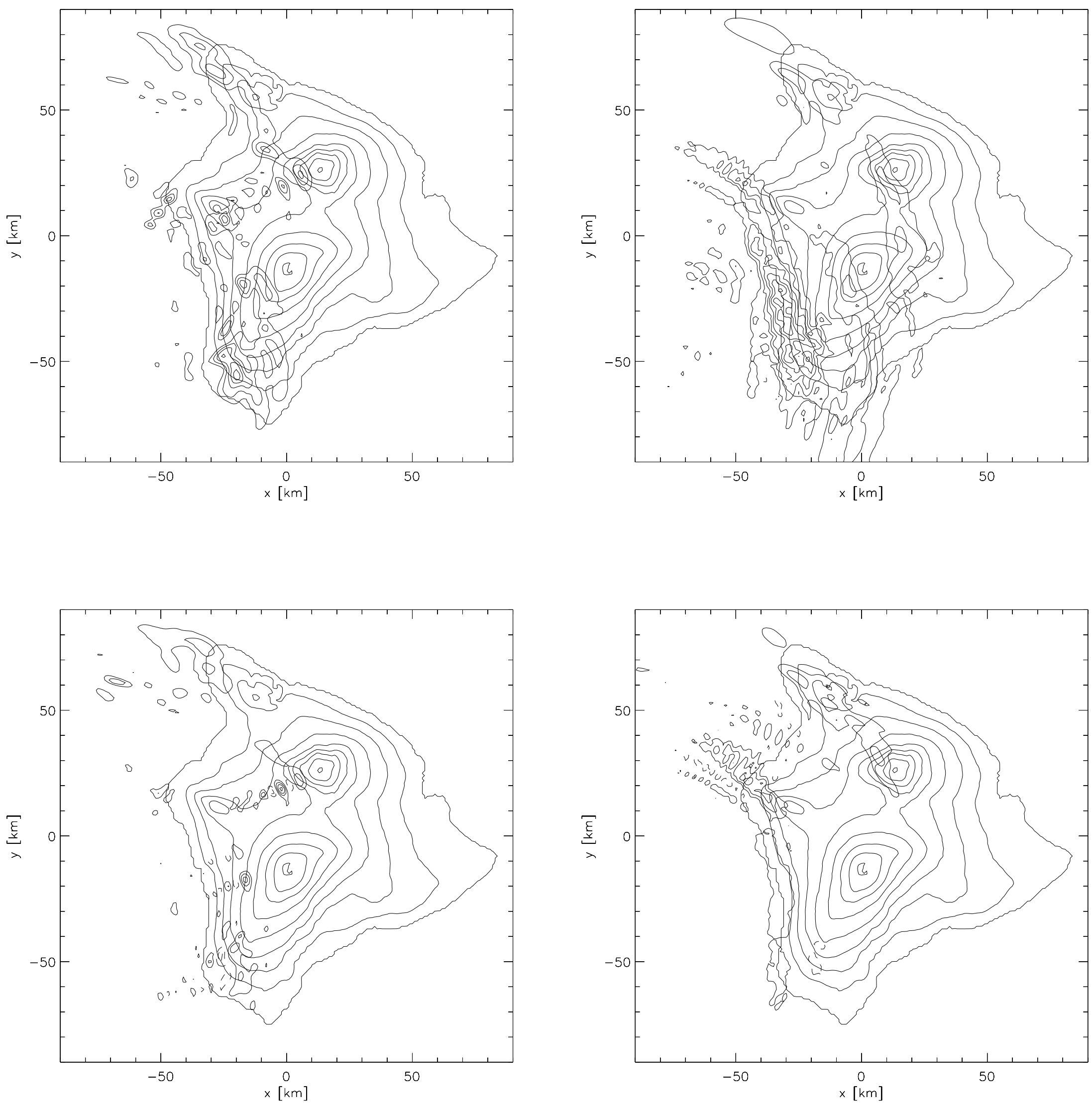

Figure 4.15: Hawaii ENE case: Horizontal cross-sections at 14km of $\rho\overline{uw}$ from FT$_w$ (top left panel) and FT$_o$ (top right panel), and $\rho\overline{vw}$ from FT$_w$ (bottom left panel) and FT$_o$ (bottom right panel). For the FT$_w$ fluxes, contour intervals are 0.4kgm^{-1}s^{-2}, while for the FT$_o$ fluxes, contour intervals are 2kgm^{-1}s^{-2}. Negative contours are dashed, and the zero contour is omitted.

Corresponding results for the NE and SE cases are shown in Figs. 4.16 and 4.17, respectively. Results are fairly consistent with the ENE case in terms of the placement of

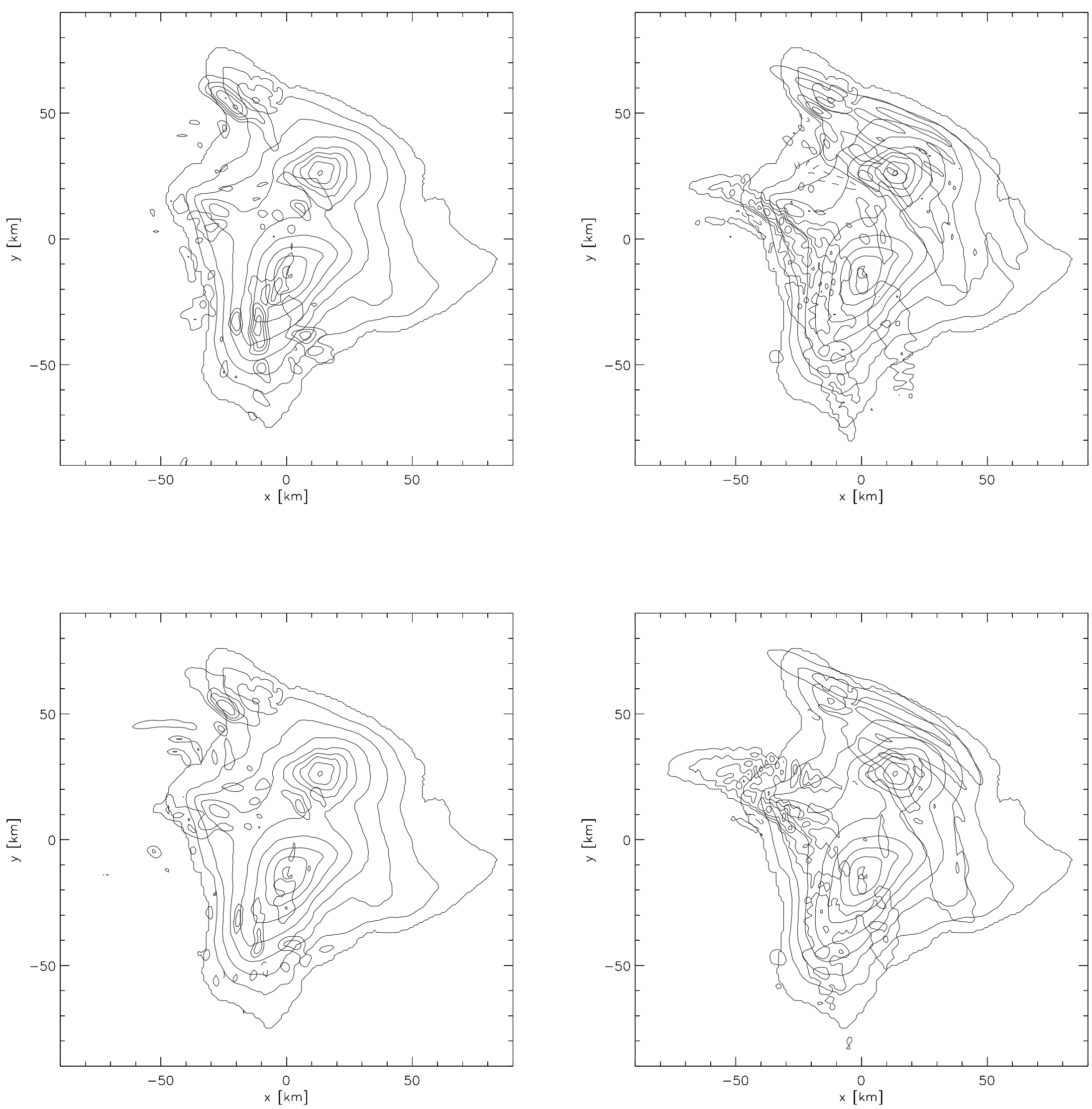

Figure 4.16: Hawaii NE case: Horizontal cross-sections at 14km of $\rho\overline{uw}$ from FT$_w$ (top left panel) and FT$_o$ (top right panel), and $\rho\overline{vw}$ from FT$_w$ (bottom left panel) and FT$_o$ (bottom right panel). For the FT$_w$ fluxes, contour intervals are 0.4kgm^{-1}s^{-2}, while for the FT$_o$ fluxes, contour intervals are 2kgm^{-1}s^{-2}. Negative contours are dashed, and the zero contour is omitted.

the wave fluxes, which are generally located in regions where w activity is most significant.

The flux magnitudes also similar in that the FT$_w$ magnitudes are much smaller than those

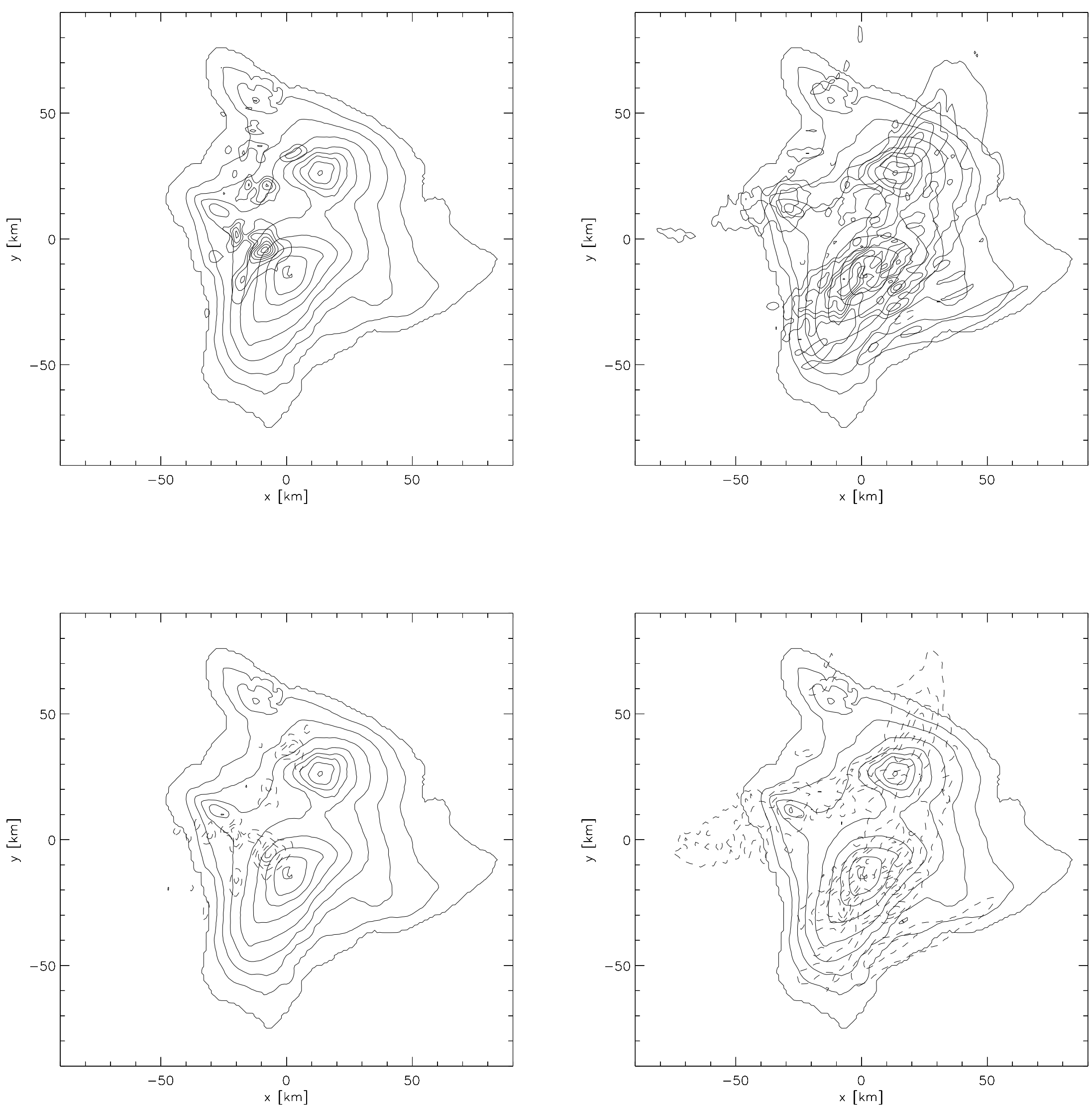

Figure 4.17: Hawaii SE case: Horizontal cross-sections at 14km of $\rho\overline{uw}$ from FT_w (top left panel) and FT_o (top right panel), and $\rho\overline{vw}$ from FT_w (bottom left panel) and FT_o (bottom right panel). For the FT_w fluxes, contour intervals are $0.4\mathrm{kgm}^{-1}\mathrm{s}^{-2}$, while for the FT_o fluxes, contour intervals are $2\mathrm{kgm}^{-1}\mathrm{s}^{-2}$. Negative contours are dashed, and the zero contour is omitted.

predicted by FT_o.

The horizontally averaged $\rho\overline{uw}$ flux in the NE case is $0.042\mathrm{kgm}^{-1}\mathrm{s}^{-2}$ for FT_w and

0.45kgm^{-1}s^{-2} for FT$_o$. For $\rho\overline{vw}$, FT$_w$ is 0.043kgm^{-1}s^{-2} and FT$_o$ is 0.33kgm^{-1}s^{-2}. Both $\rho\overline{uw}$ and $\rho\overline{vw}$ are very close in magnitude for FT$_w$, while $\rho\overline{uw}$ is somewhat larger than $\rho\overline{vw}$ for FT$_o$. As is consistent with the ENE case, there is about an order of magnitude of discrepancy between the two FT methods.

For the SE case, the FT$_w$ horizontally averaged momentum fluxes are smaller in magnitude than previously: $\rho\overline{uw}$ is 0.024kgm^{-1}s^{-2} and $\rho\overline{vw}$ is -0.020kgm^{-1}s^{-2}. These smaller values are probably due to the decreased amount of wave activity at 14km. This result would also indicate that the average horizontal flux magnitude is dependent on the wind direction, even when the Froude number, background stability, and orography remain the same. The wave momentum fluxes are affected by reduced effective mountain amplitudes and the nonlinear processes inhibiting wave generation of the downwind peaks. The FT$_o$ horizontally averaged fluxes do not show any signs of a decrease in magnitude from the previous cases: $\rho\overline{uw}$ is 0.55kgm^{-1}s^{-2} and $\rho\overline{vw}$ is -0.43kgm^{-1}s^{-2}.

We can now answer the three questions stated at the beginning of this section: (i) the horizontally averaged FT$_w$ fluxes are about an order of magnitude smaller than the FT$_o$ flux averages. This result is consistent with the results in Chapter 3 and in section 4.2 of a greater reduction in flux magnitude as the Froude number decreases compared to predictions from traditional linear theory. For (ii), the horizontally averaged fluxes are sensitive to the wind direction, and (iii) flux activity is generally localized and confined to regions where corresponding w values are large.

4.5 Concluding Remarks

The principal objective of this chapter is to demonstrate how for a nonlinear flow regime, the presence of complicated orography greatly affects the wave field. In the first (and simplest) example, it was shown how the location of a secondary mountain peak leads to a reduction in the horizontally averaged momentum flux. Wave generation is completely cut-off when the secondary peak is located in the wake region of the first mountain. When the secondary peak is located upstream of the primary peak, waves are generated from both peaks but the horizontally averaged momentum fluxes are reduced when compared to the peaks independently generating waves in different simulations.

Hawaii was the focus for the remainder of the chapter because of its complex (yet not too complex) orographic structure. The Big Island of Hawaii is dominated by two volcanic peaks towering over 4km and also has two lesser peaks which have heights of 1.5km and 2km. Due to its location in the tropics, Hawaii is dominated by the trade winds, which are light east-northeasterly winds that result in an effective Froude number of 0.2 (for the two taller peaks).

Our objectives for the Hawaii simulations are threefold: (1) analyze how the upstream orography affects mountain wave generation of the downstream orography, (2) determine the extent that variations in the initial wind direction affect the wave field and momentum fluxes over the dominant peaks, and (3) observe characteristics of the wave field such as the dominant wavelengths, intensities, etc. The solutions from WRF are then compared to corresponding FT_w and FT_o wave field solutions to assess their overall accuracy.

With a typical east-northeasterly trade wind, the north and south peaks and the northwest ridge are the dominant wave generating terrain features. There is no significant wave activity over the west peak. FT_w is able to reproduce the locations of the waves, while FT_o erroneously places much of the wave activity off of the west coast. These features are also prevalent in the FT momentum flux calculations, where the majority of fluxes are in the same region as the wave activity represented by w.

In the northeast wind case, the northwest ridge and the west and north peaks generate wave activity, while lesser amounts of activity is generated by the south peak. In addition, there is some wave activity near the southeast coast which is associated with deflected flow descending towards the coast. As before, FT_w captures this wave activity with reasonable accuracy, while FT_o does not. In the last case, where the initial wind flow is from the southeast, the north and south peaks generate wave activity but no mountain waves are generated off of the west peak or northwest ridge. These two mountains are in the vortex shedding region of the first two peaks, and so any wave propagation will be limited by critical levels.

The horizontally wave averaged momentum fluxes $\rho\overline{u'w'}$ and $\rho\overline{v'w'}$ are calculated for all of the cases in this chapter, and the FT_w magnitudes are substantially smaller than the results with FT_o. This is also consistent with the bell-shaped hills in Chapter 3 where nonlinear effects are important as well. Thus for all of these cases, larger momentum flux discrepancies between FT_w and FT_o coincide with lower Froude number flows. For the Hawaii case with a Froude number of 0.2, the FT_w momentum flux averages are about one-tenth the magnitude of the corresponding FT_o averages. The FT_w flux averages are also decreased in the presence of complex orography, where low level nonlinear effects from adjacent peaks affect the wave generation capabilities of the peaks.

It should be noted that there is often vertical wind shear and a zero-wind surface in the upper troposphere or stratosphere over Hawaii - a direct result of the Hadley circulation. This means that critical levels are present at those levels, and mountain wave propagation through the stratosphere is probably rare. By observing the wave fields and their associated wave momentum fluxes, we can qualitatively obtain a picture of relatively small pulses of wave activity over the peaks propagating vertically until encountering the critical layer. The momentum flux estimates also allow for quantitative predictions of drag in the shear layer.

Chapter 5: Conclusion

5.1 A Brief Overview

Throughout this dissertation we examine how nonlinear flow regimes in mountainous regions affect gravity wave generation and propagation. The dissertation begins with an examination of linear gravity wave theory, which forms the basis of many mountain wave parameterization schemes and one of the numerical models employed here. By doing so, in the course of research we examine at which points linear theory is still applicable in highly nonlinear flows. In order to understand these processes, we compare the results of a fully nonlinear numerical model to a corresponding linear wavefield model.

The WRF model, which is non-linear, non-hydrostatic, and fully compressible, has been used extensively throughout the research in this dissertation. The FT model, a linear semi-analytical nonhydrostatic model, solves a dispersion relation (Eqn. 2.4) to calculate the wave field on horizontal levels. By comparing corresponding results of WRF and FT, we can then determine which regions of a nonlinear solution in WRF behaves approximately linear.

This dissertation begins with a review of linear gravity wave theory, and its predictions of mountain wave behavior. In traditional linearized solutions of the mountain wave problem, analytical models assume the surface vertical displacement field is the orography (i.e. the mountain), and then parameters such as w and the momentum fluxes are calculated at various heights above the surface. The one prerequisite for linear theory is, of course, that the flow regime has to exhibit approximately linear behavior. A commonly used parameter to assess the linearity of a flow regime is the Froude Fr_h number. When $Fr_h > 1$, the flow is assumed to behave in a linear fashion, while when Fr_h is near or below unity, nonlinear processes become important.

In section 1.3 analytical linear mountain wave solutions are shown for hydrostatic, non-hydrostatic, and evanescent wave regimes for a Froude number of 11. These results are then compared to corresponding WRF and FT simulations, all of which have similar results. In this instance (section 2.3), linear wave theory provides a good approximation to the mountain wave field, and the traditional lower boundary used in FT_o (the Fourier Transform method initialized with the surface vertical displacement) is adequate. We then introduce an alternative approach to the linear mountain wave method - instead of applying the vertical displacement as the lower boundary, a horizontal cross-section of w from WRF taken at an arbitrary height is used the initialization of FT where the wavefield solution is determined both above and below the height level. This new method, FT_w, also compares favorably to the linear analytical solutions. For this particular case, the WRF nonlinear wave field at the height of initialization behaves in an approximately linear fashion.

For the linear case presented here, WRF and the two FT methods produce similar results. As nonlinear processes become more dominant in a mountainous region, the orographic generation of gravity wave fields becomes a considerably complex issue that does not conform easily to the predictions of linear theory. In section 1.4 we discuss relevant numerical simulations and field experiments of the low level atmospheric flow and gravity wave generation for low Froude number regimes. Perhaps the simplest theory describing flow around a circular hill is the Dividing Streamline concept, which uses energy arguments to show that the flow at lower levels is deflected around a mountain and therefore does not contribute to wave generation. According to this theory, the effective Froude number (or Fr for the portion of the flow which affects wave generation) cannot be less than 1. Numerous laboratory tank-flow experiments generally support this notion, though an additional constant has often been appended to the equation to account for internal drag and pressure acceleration.

A series of numerical experiments of uniform flow over a circular-shaped hill have provided some insight into how the flow around mountains are affected as Fr is decreased. U and N are initially constant throughout the model domains, and Fr is determined by the hill height.

The nonlinear wave field solution appears entirely different from its linear counterpart when $Fr = 0.67$. This flow regime is dominated by low level wave breaking just to the lee of the hill, convectively generated by the overturning of streamlines. Low level flow splitting is also evident, and lee vortices begin to take shape. Downslope velocity maximums near the surface and intense TKE in the breaking wave region are also observed in the numerical simulations. Hence the nonlinear WRF solution departs significantly from the traditional linear wave solution of FT_o. The WRF solution is dominated by shorter horizontal wavelengths and has characteristics of a non-hydrostatic wavefield (the linear solution depicts a hydrostatic wavefield). The linear FT_w wavefield, on the other hand, is shown to exhibit considerable agreement with the corresponding WRF solution. This is particularly the case when FT_w is initialized above the low-level nonlinear flow. Numerical experiments show that as the initialization level of FT_w is dropped into the intense TKE region, the FT_w wavefield diverges from the WRF solution.

We then examine the wavefield for the case when $Fr = 1/3$. In this regime, flow splitting and lee vortices dominate the flow. Gravity wave breaking occurs above the lee slope, though it is less intense than in the previous case. As before, the FT_w solution compares more favorably with the corresponding WRF solution than FT_o. The WRF wavefield solution appears to show some temporal variability in this case, which presents a small problem for the steady state FT solutions. Even so, FT_w continues to represent a substantial improvement over FT_o in the representation of the wavefields generated by nonlinear flows.

It has been shown that FT_w represents an improvement over FT_o for isolated bell-shaped ridges for Froude numbers as low as 1/3. In the next major research topic of this dissertation, we want to examine the extent this remains valid for realistic orography. Field experiments in mountainous regions where low-level nonlinear flows are predominant indicate that the wavefield might be substantially modified by low level nonlinear effects.

Two types of nonlinear flow regimes have been extensively studied in mountain wave experiments: the large amplitude breaking wave over a two dimensional ridge such as in Colorado, 1972 or Greenland in FASTEX, and wavefields in regions of complex orography, such as the Pyrenees (PYREX) or the Alps (MAP). In the former case, a large amplitude breaking wave occurs over a quasi-two dimensional ridge. Downslope windstorms and intense TKE throughout the troposphere also occur. This type of flow regime has been compared to a hydraulic jump.

In the latter case, the orography is complex with many singular peaks and valleys. Hence lower-atmospheric nonlinear effects have been found to be very influential in wavefield generation. Flow blocking, flow splitting, and stagnant boundary layers in the mountainous regions are generally thought to reduce the effective mountain height, and therefore reduce the occurrence and intensity of gravity wave propagation and low level breaking. Upstream air parcels near the surface will typically flow around the mountains rather than over them. When upstream forcing became more intense, channel or valley flows can occur, and spotty wave generation has been observed in regions where air flows over descending terrain. Instances of a stagnant boundary layer also has the effect of absorbing downwards propagating gravity waves, which then effectively cuts-off the horizontal propagation of trapped lee waves.

As we extend our research to flows in regions of complex orography, two simulations are examined where a secondary peak is placed either downstream or upstream of the primary peak, which has a Froude number of 1/3. The wavefield is found to be significantly modified when the secondary peak is located in the wake of the primary peak. Only the primary peak generates waves, and the horizontally averaged momentum flux calculated by FT_w is very similar to the $Fr = 1/3$ case. When the secondary peak is located upstream of the primary peak, both peaks generate mountain waves. The horizontally average momentum flux in this simulation is less what might be expected if we assume that each peak is independent of the other. Low level nonlinear processes in the vicinity of the two peaks act to reduce mountain wave activity. These results also suggest that horizontally averaged momentum fluxes are dependent on the background wind direction.

We keep these findings in mind in our subsequent analysis of the wavefield over the Big Island of Hawaii, which has complex orography dominated by four peaks. Hawaii's climate is fairly consistent year-round, and is dominated by the east-northeasterly trade winds. Three WRF simulations are conducted here that assume a Froude number of 0.2 (for the highest peak), with a different background wind direction in each simulation. The main objective is to examine the sensitivity of the wavefield to the ambient wind direction, and also to assess the accuracy of both FT methods to such a low Froude number regime. Since Hawaii almost always has vertical shear in the stratosphere as the mean wind reverses direction (from east to west), we also investigate the location and intensity of the dominant momentum fluxes as wave drag might be an important and consistant feature.

In the first case, with an east-northeast background wind direction, wavefields are generated by three of the four peaks. The fourth peak is located downstream of one of the wave generating peaks, and the wake caused by the upstream peak effectively cancels wave generation over the downstream peak. The WRF results are more characteristic of the wavefields observed in complex orographic regions such as the Alps, rather than the large amplitude mountain waves found over Greenland. The wavefields are very localized, with short dominant wavelengths of around 10km. FT_w manages to approximately re-create the WRF results, while the FT_o inaccurately places a significant amount of wave activity off the west coast and over the peak where no wave generation is present. Similar results are found in the $\rho\overline{uw}$ and $\rho\overline{vw}$ wave flux calculations. Both FT methods place much of the flux activity in the immediate vicinity of large w values, and its horizontal extent is limited and localized.

The horizontally averaged momentum flux values provide further evidence that low level nonlinear processes are limiting the effective amplitude of the orography, and thus limiting the amount of drag which impacts the background flow at high altitudes. Horizontally averaged fluxes from FT_w are consistently about an order of magnitude smaller than corresponding FT_o results for all of the Hawaii cases. This would indicate that the use of the traditional lower boundary to calculate the momentum fluxes leads to an overestimation of the wave drag contribution to the flow.

The second and third Hawaii cases exemplify the extent at which even minor variations in the upstream wind direction can affect wave generation. When the wind is from the northeast, wave generation off the west peak becomes significant (it had been negligible in the previous case). The two northernmost peaks also are generating waves, while the south peak's ability for wave generation is very limited (it is in the wake of the north peak). Also of interest is that wave generation occurs over the southeast coast. This is not associated with any of the peaks, but is due to flow being deflected around the north peak and subsequently descending towards the coast. The results from FT_w and FT_o are similar as before, with FT_w producing a wave field more characteristic of WRF.

In the southeasterly upstream wind case, the two tallest peaks are the main wave generators. The west peak and northwest ridge are in the wake of the two tall peaks, and so no waves are generated over them in the WRF simulation. As before, the FT_w solution is more similar to WRF than FT_o. The horizontally averaged momentum flux magnitudes from FT_w in this case are about half of the Hawaii case where the incident wind is from the northeast. This is most likely the result of wave suppression in the lee of the taller peaks.

Therefore, the initial wind direction also is an important factor to consider when assessing momentum flux transport in the upper atmosphere.

Our research concludes with the complex orography of Hawaii. Nonlinear flow regimes caused by sufficiently tall orography have a profound effect on wave generation, and must be taken into account in mountain wave parameterization schemes. The incident wind direction must also be considered when the orography is complex. We have shown that low level nonlinear processes not only influence wave generation over a region of complex orography such as Hawaii, but also on simple isolated hills. We also presented an alternative to the traditional linear approach of the mountain wave problem. Instead of initialization of the lower boundary with the vertical displacement, we have shown that the initialization of a linear model outside of the low level nonlinear processes lead to greater accuracy of wavefield predictions in areas where the flow can be approximated by linear theory.

5.2 Future Research Directions

There is a considerable amount of work that can be done for the improvement of the Fourier Transform method to predict mountain wave fields in nonlinear flow regimes. With our assumption of a vertically uniform background flow, we have only begun to scratch the surface of possibilities to test FT capabilities. Most characteristics of the real atmosphere have been neglected thus far: no horizontal or vertical variation in the background flow, no Coriolis force, no diabatic effects, and no surface friction. Only after gradually testing these parameters can we determine how much the FT method can be generalized.

One of the first tests to expand the applicability of FT is to predict wave breaking due to vertical density variations. This is a relatively straightforward first step as it can be tested with a uniform atmosphere, and efforts in this direction are currently underway at NRL. Another possible direction is to assess the ability of FT_w to simulate a trapped wave field due to a vertical variation of the background wind speed. This has already been successfully accomplished with FT_o (Broutman et al., 2003). FT_o also performs well in some instances with vertically varying wind direction and stability (Eckermann et al., 2006a), and so this is another logical step in the development of FT_w.

The situation becomes considerably more complex with the introduction of an external critical level. Upwards propagating gravity waves are then reflected or absorbed into the mean flow, sometimes resulting in intense TKE generation. Another possibility to consider is deflection due to the Coriolis force, though perhaps that might only be important for large hydrostatic wavelengths.

There is much literature concerning diabatic effects such as radiational heating and latent heat release on the low level flow field in mountainous regions. Studies since Braham and Draginis (1960) have demonstrated the importance of heating on mountain slopes, and Reisner and Smolarkiewicz (1994) create a nondimensional parameter analogous to the Froude number to estimate the importance of thermal forcing on a slope. We have already noted that a stagnant boundary layer affects wave generation and propagation, and the amount of surface friction can also greatly affect the boundary layer (i.e. trees versus grass). These topics are beyond the scope of this dissertation, but might warrant an investigation eventually.

In addition to the additional effects just mentioned, the importance of model resolution should be investigated at some point. The Alps field experiments showed that the dominant horizontal wavelengths can be very short, and so our current horizontal resolution of 1km is probably not fully adequate. There should probably also be a closer examination on how lee vortex shedding affects the wave field, so that the amount of variability in the wave field can be more accurately quantified.

This work is motivated by the search for more accurate mountain wave parameterization schemes, and also to develop a greater understanding of the physical characteristics of mountain waves in low Froude number flow regimes. The research in this dissertation forms just a small subset of the continuously evolving and expanding area of mountain wave research. What began decades ago with analytical mountain wave solutions for simplified flow regimes has evolved into multinational field campaigns and complex numerical simulations using state-of-the-art weather models and super computers. It is unlikely that mountain wave research will abate any time soon.

Appendix A: WRF Model Description

The following is a detailed description of the Weather, Research, and Forecasting (WRF) model. The equations are adapted specifically for the idealized simulations presented in this dissertation (i.e. variables such as water vapor, surface friction, and the Coriolis force are neglected). Refer to Skamarock et al. (2005) for a full technical explanation of WRF.

A.1 The Governing Equations

This section details the governing equations discretized and integrated in WRF. The compressible non-hydrostatic Euler equations in flux-form are formulated in a terrain-following coordinate system, and so it is appropriate to first describe how the hydrostatic terrain-following vertical coordinate η is defined:

$$\eta = (p_h - p_{ht})/\mu, \qquad \text{where } \mu = p_{hs} - p_{ht}.$$

p_h is the hydrostatic pressure component, while p_{hs} and p_{ht} are pressure levels at the terrain-following surface and top boundary, respectively. η is called a mass vertical coordinate, and varies from 1 at the surface to 0 at the upper boundary. The flux-form variables are now denoted as

$$\mathbf{V} = \mu\mathbf{v} = (U, V, W), \qquad \Omega = \mu\dot{\eta}, \qquad \Theta = \mu\theta.$$

$\mathbf{v} = (u, v, w)$ are the covariant variables in the horizontal and vertical directions, and $\omega = \dot{\eta}$ is the contravariant vertical velocity. θ is the potential temperature. Non-conserved variables include the geopotential $\phi = gz$, pressure p, and $\alpha = 1/\rho$ the inverse density. The flux-form Euler equations now take the form

$$\frac{\partial U}{\partial t} = -\frac{\partial Uu}{\partial x} - \frac{\partial Vu}{\partial y} - \frac{\partial \Omega u}{\partial \eta} + \frac{\partial p(\partial \phi/\partial \eta)}{\partial x} - \frac{\partial p(\partial \phi/\partial x)}{\partial x} + F_U \tag{A.1}$$

$$\frac{\partial V}{\partial t} = -\frac{\partial Uv}{\partial x} - \frac{\partial Vv}{\partial y} - \frac{\partial \Omega v}{\partial \eta} + \frac{\partial p(\partial \phi/\partial \eta)}{\partial y} - \frac{\partial p(\partial \phi/\partial y)}{\partial y} + F_V \tag{A.2}$$

$$\frac{\partial W}{\partial t} = -\frac{\partial Uw}{\partial x} - \frac{\partial Vw}{\partial y} - \frac{\partial \Omega w}{\partial \eta} + g(\frac{\partial p}{\partial \eta} - \mu) + F_W \tag{A.3}$$

$$\frac{\partial \Theta}{\partial t} = -\frac{\partial U\theta}{\partial x} - \frac{\partial V\theta}{\partial y} - \frac{\partial \Omega\theta}{\partial \eta} + F_\Theta \tag{A.4}$$

$$\frac{\partial \mu}{\partial t} = -\frac{\partial U}{\partial x} - \frac{\partial V}{\partial y} - \frac{\partial \Omega}{\partial \eta} \tag{A.5}$$

$$\frac{\partial \phi}{\partial t} = -\mu^{-1}\left(U\frac{\partial \phi}{\partial x} + V\frac{\partial \phi}{\partial y} + \Omega\frac{\partial \phi}{\partial \eta} - gW\right) \tag{A.6}$$

F_U, F_V, F_W, and F_Θ represent forcing terms from model physics and turbulent mixing. Diagnostic relations for the inverse density and the equation of state take the form $\partial\phi/\partial\eta = -\alpha\mu$ and $p = p_0(R_d\theta/p_0\alpha)^y$, respectively. R_d is the gas constant for dry air, p_0 is a reference pressure (usually 10^5 Pascals), and $y = c_p/c_v = 1.4$ is the ratio of the heat capacities for dry air. Moisture, Coriolis, and Curvature terms can be used in the WRF model, though are not described here because they are beyond the scope of this research.

The Euler equations are cast into perturbation form before being discretized in the WRF model. This is advantageous as perturbation variables reduce truncation errors in the horizontal pressure gradient, and reduce machine rounding errors in the vertical pressure gradient and buoyancy calculations. It is assumed that the perturbations are deviations from a hydrostatically-balanced reference state, and the reference state variables are defined as satisfying the governing equations of the atmosphere at rest and are only a function of height. In this case, $p = \overline{p}(z) + p'$, $\phi = \overline{\phi}(z) + \phi'$, $\alpha = \overline{\alpha}(z) + \alpha'$, and $\mu = \overline{\mu}(x, y) + \mu'$. The vertical coordinate η, the variables $\overline{p}$, $\overline{\phi}$, and $\overline{\alpha}$ are a function of (x,y,η) since η coordinate surfaces can vary in the vertical direction. Substituting these new definitions into Eqns. (A.1) to (A.6), the perturbation Euler equations take on the following form (after some manipulation of the geopotential terms with its diagnostic relation):

$$\frac{\partial U}{\partial t} = -\frac{\partial Uu}{\partial x} - \frac{\partial Vu}{\partial y} - \frac{\partial \Omega u}{\partial \eta} - \left(\mu\alpha\frac{\partial p'}{\partial x} + \mu\alpha'\frac{\partial \overline{p}}{\partial x}\right) - \left(\mu\frac{\partial \phi'}{\partial x} + \frac{\partial p'(\partial\phi/\partial x)}{\partial \eta} - \mu'\frac{\partial \phi}{\partial x}\right) + F_U \tag{A.7}$$

$$\frac{\partial V}{\partial t} = -\frac{\partial Uv}{\partial x} - \frac{\partial Vv}{\partial y} - \frac{\partial \Omega v}{\partial \eta} - \left(\mu\alpha\frac{\partial p'}{\partial y} + \mu\alpha'\frac{\partial \overline{p}}{\partial y}\right) - \left(\mu\frac{\partial \phi'}{\partial y} + \frac{\partial p'(\partial\phi/\partial y)}{\partial \eta} - \mu'\frac{\partial \phi}{\partial y}\right) + F_V \tag{A.8}$$

$$\frac{\partial W}{\partial t} = -\frac{\partial Uw}{\partial x} - \frac{\partial Vw}{\partial y} - \frac{\partial \Omega w}{\partial \eta} + g(\frac{\partial p'}{\partial \eta} - \mu') + F_W \tag{A.9}$$

$$\frac{\partial \Theta}{\partial t} = -\frac{\partial U\theta}{\partial x} - \frac{\partial V\theta}{\partial y} - \frac{\partial \Omega\theta}{\partial \eta} + F_\Theta \tag{A.10}$$

$$\frac{\partial \mu'}{\partial t} = -\frac{\partial U}{\partial x} - \frac{\partial V}{\partial y} - \frac{\partial \Omega}{\partial \eta} \tag{A.11}$$

$$\frac{\partial \phi'}{\partial t} = -\mu^{-1}\left(U\frac{\partial \phi}{\partial x} + V\frac{\partial \phi}{\partial y} + \Omega\frac{\partial \phi}{\partial \eta} - gW\right) \tag{A.12}$$

Eqns. (A.7) to (A.12), along with the TKE prognostic equation, represent the equations integrated in the WRF model.

Note that WRF has a series of options for physical diffusion - we describe the option for the 1.5 order turbulent closure scheme. The momentum equations include the velocity stress tensor for evaluating diffusion in physical space:

$$\frac{\partial U}{\partial t} = \cdots - \left[\frac{\partial \tau_{11}}{\partial x} + \frac{\partial \tau_{12}}{\partial y} - \frac{\partial[(\partial z/\partial x)\tau_{11} + (\partial z/\partial y)\tau_{12}]}{\partial z}\right] - \frac{\partial \tau_{13}}{\partial z} \tag{A.13}$$

$$\frac{\partial V}{\partial t} = \cdots - \left[\frac{\partial \tau_{12}}{\partial x} + \frac{\partial \tau_{22}}{\partial y} - \frac{\partial[(\partial z/\partial x)\tau_{12} + (\partial z/\partial y)\tau_{22}]}{\partial z}\right] - \frac{\partial \tau_{23}}{\partial z} \tag{A.14}$$

$$\frac{\partial W}{\partial t} = \cdots - \left[\frac{\partial \tau_{13}}{\partial x} + \frac{\partial \tau_{23}}{\partial y} - \frac{\partial[(\partial z/\partial x)\tau_{13} + (\partial z/\partial y)\tau_{23}]}{\partial z}\right] - \frac{\partial \tau_{33}}{\partial z} \tag{A.15}$$

The stress tensor τ is written as:

$$\tau_{11} = \mu K_h D_{11},$$

$$\tau_{22} = \mu K_h D_{22},$$

$$\tau_{33} = \mu K_v D_{33},$$

$$\tau_{12} = \mu K_h D_{12},$$

$$\tau_{13} = \mu K_h D_{13},$$

$$\tau_{23} = \mu K_h D_{23}.$$

K_h is the horizontal eddy viscosity, and K_v is the vertical eddy viscosity. D is the deformation tensor (it is symmetric so that $D_{ij} = D_{ji}$). The individual components of D are:

$$D_{11} = 2\left[\frac{\partial u}{\partial x} - \frac{\partial z}{\partial x}\frac{\partial u}{\partial z}\right],$$

$$D_{22} = 2\left[\frac{\partial v}{\partial y} - \frac{\partial z}{\partial y}\frac{\partial v}{\partial z}\right],$$

$$D_{33} = 2\frac{\partial w}{\partial z},$$

$$D_{12} = \left[\frac{\partial u}{\partial y} - \frac{\partial z}{\partial y}\frac{\partial u}{\partial z} + \frac{\partial v}{\partial x} - \frac{\partial z}{\partial x}\frac{\partial v}{\partial z}\right],$$

$$D_{13} = \left[\frac{\partial w}{\partial x} - \frac{\partial z}{\partial x}\frac{\partial w}{\partial z}\right] + \frac{\partial u}{\partial z},$$

$$D_{23} = \left[\frac{\partial w}{\partial y} - \frac{\partial z}{\partial y}\frac{\partial w}{\partial z}\right] + \frac{\partial v}{\partial z}.$$

For the prognostic potential temperature equation, the diffusion deformation is

$$\frac{\partial \Theta}{\partial t} = \cdots + \left[\left(\frac{\partial}{\partial x} - \frac{\partial(\partial z/\partial x)}{\partial z}\right)\left(\mu K\left(\frac{\partial}{\partial x} - \frac{\partial z}{\partial x}\frac{\partial}{\partial z}\right)\right)\right]\theta +$$
$$\left[\left(\frac{\partial}{\partial y} - \frac{\partial(\partial z/\partial y)}{\partial z}\right)\left(\mu K\left(\frac{\partial}{\partial y} - \frac{\partial z}{\partial y}\frac{\partial}{\partial z}\right)\right) + \frac{\partial \mu K(\partial/\partial z)}{\partial z}\right]\theta \tag{A.16}$$

The next step in formulating the turbulence closure scheme is to determine a value for the eddy viscosity, K. As the scheme used here is of order 1.5, inclusion of the prognostic equation for TKE is incorporated into K.

$$K_{h,v} = C_k l_{h,v} \sqrt{e}$$

where e is the turbulent kinetic energy. C_k is a constant which typically varies between 0.15 and 0.25, and l is a length scale. If the grid spacing $\triangle x$ is less than the user-specified critical length scale l_{cr}, then

$$l_{h,v} = min[\triangle x \triangle y \triangle z)^{1/3}, 0.76\sqrt{e}/N] \qquad \text{for } N^2 > 0,$$

$$l_{h,v} = (\triangle x \triangle y \triangle z)^{1/3} \qquad \text{for } N^2 \leq 0$$

For scalar mixing such as potential temperature, $K_{h,v}$ is also multiplied by an inverse turbulent Prandtl number $P_r^{-1} = 1 + 2l/(\triangle x \triangle y \triangle z)^{1/3}$.

When the grid spacing $\triangle x$ is greater than the critical length scale l_{cr}, then $l_h = \sqrt{\triangle x \triangle y}$ for the calculation of K_h. For K_v, the vertical length scale l_v is calculated

$$l_v = min[\triangle z, 0.76\sqrt{e}/N] \qquad \text{for } N^2 > 0,$$

$$l_v = \triangle z \qquad \text{for } N^2 \leq 0$$

For scalar mixing, K is multiplied by an inverse turbulent Prandtl number. For horizontal eddy viscosity K_h the Prandtl number is $P_r = 1/3$, and for vertical eddy viscosity K_v, it is expressed as $P_r = 1 + 2l/\triangle z$.

The turbulent kinetic energy prognostic equation takes the form

$$\frac{\partial \mu e}{\partial t} = -\frac{\partial Ue}{\partial x} - \frac{\partial Ve}{\partial y} - \frac{\partial \Omega e}{\partial \eta} + \mu(\text{shear production} + \text{buoyancy} + \text{dissipation}). \quad \text{(A.17)}$$

The three source and sink terms on the right are shown below. Shear production, is written as

$$\text{shear production} = K_h D_{11}^2 + K_h D_{22}^2 + K_v D_{33}^2 + K_h D_{12}^2 + K_v D_{13}^2 + K_v D_{23}^2. \quad \text{(A.18)}$$

The buoyancy term in the TKE equation is:

$$\text{buoyancy} = -K_v N^2. \quad \text{(A.19)}$$

The dissipation term depends in part on the critical length scale l_{cr}. If $\triangle x < l_{cr}$ then the dissipation term takes the form

$$\text{dissipation} = -\frac{Ce^{3/2}}{l} \quad \text{(A.20)}$$

where

$$C = 1.9C_k + \frac{(0.93 - 1.9C_k)l}{\triangle s}. \quad \text{(A.21)}$$

$\triangle s = (\triangle x \triangle y \triangle z)^{1/3}$, and $l = min[(\triangle x \triangle y \triangle z)^{1/3}, 0.76\sqrt{e}/N]$

If $\triangle x > l_{cr}$ the dissipation term is

$$\text{dissipation} = -\frac{2\sqrt{2}}{15}\frac{e^{3/2}}{l} \quad \text{(A.22)}$$

where

$$l = \frac{kz}{1 + kz/l_0} \quad \text{(A.23)}$$

and

$$l_0 = min\left(\frac{\alpha_b \int_0^{z_1} \sqrt{e} z dz}{\int_0^{z_1} \sqrt{e} dz}, 80\right). \tag{A.24}$$

$\alpha_b = 0.2$, and $k = 0.4$ is the von Karman constant.

A.2 Discretization of the Equations

Many options are available in choosing the method of finite difference discretization. In short, one can use a second or third Runge-Kutta time-stepping option, and horizontal and vertical advection schemes can be anywhere from second to sixth order. The recommended options are a third order Runge-Kutta time step, a fifth order horizontal advection scheme, and a third order vertical advection scheme. Those options are chosen for the model runs in this dissertation.

A.2.1 The Time Stepping Scheme

The WRF model has a time-split integration scheme, where the slow or low frequency modes of meteorological significance are integrated with the third order Runge-Kutta scheme (RK3), and the high-frequency acoustic modes are integrated over smaller time steps for reasons of numerical stability. This time stepping scheme has its origins in Klemp and Wilhelmson (1978), Skamarock and Klemp (1992), and Wicker and Skamarock (2002).

The RK3 scheme uses a predictor-corrector formulation to integrate the prognostic equations. Using $\Phi = (U, V, W, \Theta, \phi', \mu')$ to denote the prognostic variables and $\frac{\partial \Phi}{\partial t} = R(\Phi)$ for the prognostic equations, the RK3 integration is accomplished in 3 steps to advance a solution $\Phi(t)$ to $\Phi(t + \triangle t)$:

$$\Phi* = Phi^t + \frac{\triangle t}{3} R(\Phi^t), \tag{A.25}$$

$$\Phi ** = \Phi^t + \frac{\triangle t}{2} R(\Phi*), \tag{A.26}$$

$$\Phi^{t+\triangle t} = \Phi^t + \triangle t R(\Phi **). \tag{A.27}$$

$\triangle t$ is the low-frequency modes time step, and superscripts denote time levels. Skamarock et al. (2005) note that this is technically not a true RK3 scheme because it is second-order accurate for nonlinear equations (for linear equations it has third order accuracy).

To prevent limitations in the $RK3$ time step $\triangle t$, high-frequency meteorologically insignificant acoustic modes are handled in a way outlined by Wicker and Skamarock (2002). A perturbation form of the governing equations is integrated using smaller acoustic time steps within the $RK3$ larger time steps. The perturbation equations are formed for the $RK3$ time-split acoustic integration by denoting small time step variables that are deviations from the most recent $RK3$ predictor (which is denoted by the superscript $t*$ and represents either Φ^t, $\Phi*$, or $\Phi **$).

$$\mathbf{V}'' = \mathbf{V} - \mathbf{V}^{\mathbf{t}^*}, \qquad \Omega'' = \Omega - \Omega^{t^*}, \qquad \Theta'' = \Theta - \Theta^{t^*}$$
$$\phi'' = \phi' - \phi'^{t^*}, \qquad \alpha'' = \alpha' - \alpha'^{t^*}, \qquad \mu'' = \mu' - \mu'^{t^*}$$

The new definitions are then substituted into the hydrostatic relation, the equation of state, and used to derive a new vertical pressure gradient. These variables are then substituted into the prognostic equations to derive the acoustic time-step equations:

$$\frac{\delta U''}{\delta t} + \left(\mu^{t^*} \frac{\partial \overline{p}}{\partial x}\right) \alpha''^{\tau} + \left[\mu^{t^*} \frac{\partial \phi''^{\tau}}{\partial x} + \frac{\partial \phi^{t^*}}{\partial x} \left(\frac{\partial p''}{\partial \eta} - \mu''\right)^{\tau}\right] = R_U^{t^*} \tag{A.28}$$

$$\frac{\delta V''}{\delta t} + \left(\mu^{t^*}\frac{\partial \overline{p}}{\partial y}\right)\alpha''^{\tau} + \left[\mu^{t^*}\frac{\partial \phi''^{\tau}}{\partial y} + \frac{\partial \phi^{t^*}}{\partial y}\left(\frac{\partial p''}{\partial \eta} - \mu''\right)^{\tau}\right] = R_V^{t^*} \tag{A.29}$$

$$\frac{\delta W''}{\delta t} - g\overline{\left[\frac{\partial C(\partial \phi''/\partial \eta)}{\partial \eta} + \frac{\partial}{\partial \eta}\left(\frac{c_s^2}{\alpha^{t^*}}\frac{\Theta''}{\Theta^{t^*}}\right) - \mu''\right]}^{\tau} = R_W^{t^*} \tag{A.30}$$

$$\frac{\delta \Theta''}{\delta t} + \left[\frac{\partial (U''\Theta^{t^*})}{\partial x} + \frac{\partial (V''\Theta^{t^*})}{\partial y}\right]^{\tau+\triangle\tau} + \frac{\partial (\Omega''^{\tau+\triangle\tau}\theta^{t^*})}{\partial \eta} = R_\Theta^{t^*} \tag{A.31}$$

$$\frac{\delta \mu''}{\delta t} + \left[\frac{\partial U''}{\partial x} + \frac{\partial V''}{\partial y}\right]^{\tau+\triangle\tau} + \frac{\partial \Omega''^{\tau+\triangle\tau}}{\partial \eta} = R_\mu^{t^*} \tag{A.32}$$

$$\frac{\delta \phi''}{\delta t} + \frac{1}{\mu^{t^*}}\left[\Omega''^{\tau+\triangle\tau}\frac{\partial \phi}{\partial \eta} - \overline{gW''}^{\tau}\right] = R_\phi^{t^*} \tag{A.33}$$

The terms on the RHS of Eqns. (A.28) to (A.33) are held fixed for the acoustic steps that are used in the integration of each $RK3$ sub-step, and are written as

$$\begin{aligned} R_U^{t^*} = & -\frac{\partial U u}{\partial x} - \frac{\partial V u}{\partial y} - \frac{\partial \Omega u}{\partial \eta} - \left(\mu\alpha\frac{\partial p'}{\partial x} - \mu\alpha'\frac{\partial \overline{p}}{\partial x}\right) - \\ & \left(\mu\frac{\partial \phi'}{\partial x} - \frac{\partial p'(\partial \phi/\partial x)}{\partial \eta} + \mu'\frac{\partial \phi}{\partial x}\right) + F_U \end{aligned} \tag{A.34}$$

$$R_V^{t^*} = -\frac{\partial Uv}{\partial x} - \frac{\partial Vv}{\partial y} - \frac{\partial \Omega v}{\partial \eta} - \left(\mu\alpha\frac{\partial p'}{\partial y} - \mu\alpha'\frac{\partial \overline{p}}{\partial y}\right) -$$

$$\left(\mu\frac{\partial \phi'}{\partial y} - \frac{\partial p'(\partial\phi/\partial y)}{\partial \eta} + \mu'\frac{\partial \phi}{\partial y}\right) + F_V \tag{A.35}$$

$$R_W^{t^*} = -\frac{\partial Uw}{\partial x} - \frac{\partial Vw}{\partial y} - \frac{\partial \Omega w}{\partial \eta} + g(\frac{\partial p'}{\partial \eta} - \mu') + F_W \tag{A.36}$$

$$R_\Theta^{t^*} = -\frac{\partial U\theta}{\partial x} - \frac{\partial V\theta}{\partial y} - \frac{\partial \Omega\theta}{\partial \eta} + F_\Theta \tag{A.37}$$

$$R_\mu^{t^*} = -\frac{\partial U}{\partial x} - \frac{\partial V}{\partial y} - \frac{\partial \Omega}{\partial \eta} \tag{A.38}$$

$$R_\phi^{t^*} = -\mu^{-1}\left(U\frac{\partial \phi}{\partial x} + V\frac{\partial \phi}{\partial y} + \Omega\frac{\partial \phi}{\partial \eta} - gW\right) \tag{A.39}$$

Note that the RHS of these equations is identical to the RHS of Eqns. (A.7) to (A.12). All of the variables are evaluated at time $t*$. Further information regarding the exact details of the order of integration for the variables and their perturbations can be found in Skamarock et al. (2005). To summarize, each prognostic variable is integrated using two loops: one loop is for the three steps of the Runge-Kutta time stepping scheme ($RK3$), and an internal loop handles the acoustic step loop for each stage of $RK3$. Scalar variables such as potential temperature have no acoustic terms, and so are advanced a time step using $RK3$ only.

Spatial Discretization

The variables are spatially discretized using C grid staggering. Normal velocities are staggered one-half grid length from the thermodynamic variables. Variable indices (i,j,k) are used to indicate variable locations where $(x, y, \eta) = (i\triangle x, j\triangle y, k\triangle\eta)$. *Mass* points are denoted as the points where θ is located, and velocity locations are referred to as u points, v points, and w points. In the WRF model, column mass μ and geopotential ϕ are located at the w points, and diagnostic variables such as pressure p and inverse density α are calculated at the mass points. The grid lengths $\triangle x$ and $\triangle y$ are constants (specified by the user), and the vertical grid length $\triangle\eta$ is specified at the initialization by the user. η varies from 1 at the surface of the model to 0 at the top, and has to decrease monotonically from the surface to the top.

To spatially discretize the acoustic step equations (A.7) to (A.12), the column-mass-coupled variables are first defined relative to the uncoupled variables. The horizontal velocities are horizontally staggered relative to the column mass variables, so that they must be discretized as

$$U = \mu u \rightarrow \overline{\mu}^x u, \qquad V = \mu v \rightarrow \overline{\mu}^x v,$$

where the discrete operator $\overline{a}^x$ denotes linear interpolation in the x direction. Since the horizontal grid lengths are constant, the operator is simply represented as $\overline{a}^x = (a_{i+1/2} + a_{i-1/2})/2$. The vertical velocity W is staggered only in k, and so can be directly coupled to the column mass. The spatially discrete acoustic step equations can now be written as

$$\frac{\delta U''}{\delta t} + \overline{\mu^{t^*}}^x \overline{\alpha^{t^*}}^x \frac{\delta p''^\tau}{\delta x} + \left(\overline{\mu^{t^*}}^x \frac{\delta \overline{p}}{\delta x} \right) \overline{\alpha''^{\tau^*}}^x + \left[\overline{\mu^{t^*}}^x \frac{\delta \overline{\phi''^\tau}^\eta}{\delta x} + \frac{\delta \overline{\phi^{t^*}}^\eta}{\delta x} \left(\frac{\delta \overline{\overline{p''}}^{x\eta}}{\delta \eta} - \overline{\mu''}^x \right)^\tau \right] = R_U^{t^*} \tag{A.40}$$

$$\frac{\delta V''}{\delta t} + \overline{\mu^{t^*}}^y \overline{\alpha^{t^*}}^y \frac{\delta p''^\tau}{\delta y} + \left(\overline{\mu^{t^*}}^y \frac{\delta \overline{p}}{\delta y} \right) \overline{\alpha''^{\tau^*}}^y +$$

$$\left[\overline{\mu^{t^*}}^y \frac{\delta \overline{\phi''^\tau}^\eta}{\delta y} + \frac{\delta \overline{\phi^{t^*}}^\eta}{\delta x} \left(\frac{\delta \overline{\overline{p''}^y}^\eta}{\delta \eta} - \overline{\mu''}^y \right)^\tau \right] = R_V^{t^*} \tag{A.41}$$

$$\frac{\delta W''}{\delta t} - g \overline{\left[\frac{\delta C(\delta \phi'' / \partial \eta)}{\partial \eta} + \frac{\partial}{\partial \eta} \left(\frac{c_s^2}{\alpha^{t^*}} \frac{\Theta''}{\Theta^{t^*}} \right) - \mu'' \right]}^\tau = R_W^{t^*} \tag{A.42}$$

$$\frac{\delta \Theta''}{\delta t} + \left[\frac{\delta (U'' \overline{\Theta^{t^*}}^x)}{\delta x} + \frac{\delta (V'' \overline{\Theta^{t^*}}^y)}{\delta y} \right]^{\tau + \triangle \tau} + \frac{\delta (\Omega''^{\tau + \triangle \tau} \overline{\theta^{t^*}}^\eta)}{\delta \eta} = R_\Theta^{t^*} \tag{A.43}$$

$$\frac{\delta \mu''}{\delta t} + \left[\frac{\delta U''}{\delta x} + \frac{\delta V''}{\delta y} \right]^{\tau + \triangle \tau} + \frac{\delta \Omega''^{\tau + \triangle \tau}}{\delta \eta} = R_\mu^{t^*} \tag{A.44}$$

$$\frac{\delta \phi''}{\delta t} + \frac{1}{\mu^{t^*}} \left[\Omega''^{\tau + \triangle \tau} \frac{\delta \phi}{\delta \eta} - \overline{g W''}^\tau \right] = R_\phi^{t^*} \tag{A.45}$$

where the discrete operator $\delta a / \delta x = \triangle x^{-1} (a_{i+1/2} - a_{i-1/2})$, with analogous operators defined for y and z. The vertical interpolation operator $\overline{a}^n$ interpolates variables on mass levels k to the w levels $(k + 1/2)$, and is defined as

$$\overline{a}^n |_{k+1/2} = \frac{1}{2} \left(\frac{\triangle \eta_k}{\triangle \eta_{k+1/2}} a_{k+1} + \frac{\triangle \eta_{k+1}}{\triangle \eta_{k+1/2}} a_k \right). \tag{A.46}$$

A similar interpolation scheme is used for mass levels. The RHS terms in the discrete acoustic equations are discretized as

$$R_U^{t^*} = -\left(\overline{\mu}^x \overline{\alpha}^x \frac{\delta p'}{\delta x} - \overline{\mu}^x \overline{\alpha'}^x \frac{\delta \overline{p}}{\delta x}\right) - \left(\overline{\mu}^x \frac{\delta \overline{\phi'}^\eta}{\delta x} - \frac{\delta \overline{\overline{p'}^x}^\eta (\delta\phi/\delta x)}{\delta \eta} + \overline{\mu'}^x \frac{\delta \overline{\phi}^\eta}{\delta x}\right) + \text{advection} + \text{mixing} \qquad \text{(A.47)}$$

$$R_V^{t^*} = -\left(\overline{\mu}^y \overline{\alpha}^y \frac{\delta p'}{\delta y} - \overline{\mu}^y \overline{\alpha'}^y \frac{\delta \overline{p}}{\delta y}\right) - \left(\overline{\mu}^y \frac{\delta \overline{\phi'}^\eta}{\delta y} - \frac{\delta \overline{\overline{p'}^y}^\eta (\delta\phi/\delta y)}{\delta \eta} + \overline{\mu'}^y \frac{\delta \overline{\phi}^\eta}{\delta y}\right) + \text{advection} + \text{mixing} \qquad \text{(A.48)}$$

$$R_W^{t^*} = g\left(\frac{\delta p'}{\delta \eta} - \mu'\right) + \text{advection} + \text{mixing} \qquad \text{(A.49)}$$

Advection terms in WRF can be represented by second to sixth order discretization terms, depending on what the user wishes. The WRF developers recommend using fifth order horizontal advection terms, and third order vertical advection terms, which is done here. In discrete form, advection for a scalar q is discretized as

$$R_{q_{adv}}^{t^*} = -\frac{\delta U \overline{q}^x}{\delta x} - \frac{\delta V \overline{q}^y}{\delta y} - \frac{\delta \Omega \overline{q}^\eta}{\delta \eta}, \qquad \text{(A.50)}$$

where the discrete operator is defined as

$$\frac{\delta U \overline{q}^x}{\delta x} = \triangle x^{-1}\left[(U\overline{q}^{x^{adv}})_{i+1/2} - (U\overline{q}^{x^{adv}})_{i-1/2}\right]. \qquad \text{(A.51)}$$

The operator $\overline{q}^{x^{adv}}$ is represented in the third order advection scheme as

$$(\overline{q}^{x^{adv}})_{i-1/2} = \frac{7}{12}(q_i + q_{i-1}) - \frac{1}{12}(q_{i+1} + q_{i-2}) + \\ \text{sign}(U)\frac{1}{12}[(q_{i+1} + q_{i-2}) - 3(q_i - q_{i-1})] \tag{A.52}$$

The same operator is represented in the fifth order advection scheme as

$$(\overline{q}^{x^{adv}})_{i-1/2} = \frac{37}{60}(q_i + q_{i-1}) - \frac{2}{15}(q_{i+1} + q_{i-2}) + \frac{1}{60}(q_{i+2} + q_{i-3}) - \\ \text{sign}(U)\frac{1}{60}[(q_{i+2} + q_{i-3}) - 5(q_{i+1} - q_{i-2}) + 10(q_i - q_{i-1})] \tag{A.53}$$

The odd-order discretization schemes are inherently diffusive since they are upwind-biased. These schemes contain the next order (even) centered schemes plus an upwind term, which acts as a hyper-viscosity for the next order term and is proportional to the Courant number (Cr).

A.2.2 Stability Constraints

Both the RK3 and acoustic time steps used in the WRF model have stability constraints which are limited by the advective Courant number, $u\triangle t/\triangle x$, and the choice of advective scheme (2nd order through 6th order). The time step should satisfy the following equation:

$$\triangle t_{max} < \frac{Cr_{theory}}{\sqrt{3}}\frac{\triangle x}{u_{max}}, \tag{A.54}$$

where Cr_{theory} is a value dependent on the order of the Runge-Kutta scheme and the order of advection. This value, obtained from Wicker and Skamarock (2002) for RK3 and

5th order advection, is 1.42. For a typical case in this dissertation, where $\triangle x = 1km$ and $u_{max} = 30ms^{-1}$, the limiting time step $\triangle t_{max} = 27.3s$. In practice, the time step is usually set to 2 seconds because in our simulations large values of w are not uncommon and the vertical grid spacing is about 100m.

A.3 Numerical Filters and Damping Terms

The WRF model uses three filters for the time-split RK3 scheme: three dimensional divergence damping, an external-mode filter, and off-centering acoustic step filtering. Divergence damping is used as a filter for acoustic modes, and is accomplished in the pressure update of the acoustic step loop with forward weighting. This damping scheme uses a modified pressure when computing the pressure gradient terms in the horizontal momentum equations (A.40) to (A.45). The modified updated pressure $p^{*\tau}$ is written as

$$p^{*\tau} = p^{\tau} + \gamma_d (p^{\tau} - p^{\tau - \triangle\tau}), \tag{A.55}$$

where p^{τ} is the updated pressure, and γ_d is the damping coefficient. This modification to the updated pressure is equivalent to adding a diffusion term into the equation for 3D mass divergence. $\gamma_d = 0.1$ is recommended for WRF, regardless of the time step or grid size.

The external mode filter damps external modes in the solution by filtering the vertically-integrated horizontal divergence. This filter is represented by an additional term in the horizontal momentum equations (A.40) and (A.45):

$$\frac{\delta U''}{\delta \tau} = \ldots - \gamma_c \frac{\delta[\delta u''_{\mu}/\delta(\tau - \triangle\tau)]}{\delta x}, \tag{A.56}$$

and

$$\frac{\delta V''}{\delta \tau} = \ldots - \gamma_c \frac{\delta[\delta u''_\mu / \delta(\tau - \triangle\tau)]}{\delta y} \tag{A.57}$$

$\delta u''_\mu/\delta\tau - \triangle\tau$ is the vertically-integrated mass divergence from the previous acoustic step, and γ_c is the external mode damping coefficient. $\gamma_c = 0.01$ is the recommended value, independent of time step or grid size.

The last filter for the time-split RK3 scheme is a semi-implicit acoustic step off-centering scheme. This filtering scheme damps instabilities associated with vertically-propagating sound waves, and also damps instabilities from sloping mode levels and horizontally propagating sound waves. Off-centering is accomplished with a positive coefficient β in the acoustic time-step vertical momentum equation (A.42) and geopotential equation (A.44). $\beta = 0.1$ is recommended for WRF for all grid sizes and time steps.

In addition to the acoustic filters noted above, there is an additional Rayleigh damping term used to relax a variable back to a predetermined background state value at the top of the model domain. This is beneficial for damping upwards propagating gravity waves such as those modeled extensively in this research. In WRF, the following is added for the variables u, v, w, and θ

$$\frac{\delta u}{\delta t} = \tau(z)(u - \overline{u}) \tag{A.58}$$

$$\frac{\delta v}{\delta t} = \tau(z)(v - \overline{v}) \tag{A.59}$$

$$\frac{\delta w}{\delta t} = \tau(z) w \tag{A.60}$$

$$\frac{\delta \theta}{\delta t} = \tau(z)(\theta - \overline{\theta}). \tag{A.61}$$

Overbars represent the horizontally homogeneous reference state fields, which are functions of z only ($\overline{w}$ is assumed to be zero). The variable τ represents the vertical damping layer above a height z_r, which represents the height at which damping begins

$$\tau(z) = -\gamma_r sin^2 \left[\frac{\pi}{2} \left(1 - \frac{z_{top} - z}{z_d} \right) \right]. \tag{A.62}$$

τ increases from z_r to z_{top}, the top of the model domain. z_d is the depth of the damping layer (= $z_{top} - z_r$, and below z_r, $\tau(z) = 0$. Since the model horizontal surfaces change their height z at each time step, the background values must also be recalculated. It should be noted that WRF also has a gravity-wave absorbing layer option to use in place of the Rayleigh damping layer. The Rayleigh scheme is preferred for this research as it has been successfully applied in similar simulations of mountain waves (Klemp and Lilly, 1978; Durran and Klemp, 1983).

Bibliography

Bibliography

Bacmeister, J. T. and R. T. Pierrehumbert, 1988: On high drag states of nonlinear stratified flow over an obstacle. *Journal of the Atmospheric Sciences*, **45**, 63–80.

Baines, P. G., 1995: *Topographic effects in stratified flows*. 1st ed., Cambridge University Press, 508 pp.

Bauer, M. H., G. M. Mayr, I. Vergeiner, and H. Pichler, 2000: Strongly nonlinear flow over and around a three-dimensional mountain as a function of the horizontal aspect ratio. *Journal of the Atmospheric Sciences*, **57**, 3971–3991.

Booker, J. R. and F. P. Bretherton, 1967: The critical layer for internal gravity waves in a shear flow. *Journal of Fluid Mechanics*, **27**, 513–539.

Bougeault, P., P. Benech, P. Bessemoulin, B. Carissmo, A. Clar, J. Pelon, M. Petitdidier, and E. Richard, 1997: Pyrex: A summary of findings. *Bulletin of the American Meteorological Society*, **78**, 637–650.

Bougeault, P., A. J. Clar, B. Benech, B. Carissimo, J. Pelon, and E. Richard, 1990: Momentum budget over the pyrenees: The pyrex experiment. *Bulletin of the American Meteorological Society*, **71**, 806–818.

Braham, R. and M. Draginis, 1960: Roots of orographic cumuli. *Journal of Meteorology*, **17**, 214–226.

Bretherton, F. P., 1966: The propagation of groups of internal gravity waves in a shear flow. *Quarterly Journal of the Royal Meteorological Society*, **92**, 466–480.

Broutman, D., J. Ma, S. D. Eckermann, and J. Lindeman, 2006: Fourier-ray modeling of transient trapped lee waves. *Monthly Weather Review*, **134**, 2849–2856.

Broutman, D., J. Rottman, and S. Eckermann, 2003: A simplified fourier method for nonhydrostatic mountain waves. *Journal of the Atmospheric Sciences*, **60**, 2686–2696.

Chen, Y. L. and J. Feng, 2001: Numerical simulations of airflow and cloud distributions over the windward side of the island of hawaii. part i: The effects of trade wind inversion. *Monthly Weather Review*, **129**, 1117–1134.

Clark, T. L. and R. D. Farley, 1984: Severe downslope windstorm calculations in two and three spatial dimensions using anelastic interactive grid nesting: A possible mechanism for gustiness. *Journal of the Atmospheric Sciences*, **41**, 329–350.

Clark, T. L. and W. R. Peltier, 1977: On the evolution and stability of finite-amplitude mountain waves. *Journal of the Atmospheric Sciences*, **34**, 1715–1730.

Clark, T. L. and W. R. Peltier, 1984: Critical level reflection and the resonant growth of nonlinear mountain waves. *Journal of the Atmospheric Sciences*, **41**, 3122–3134.

Ding, L., R. J. Calhoun, and R. Street, 2003: Numerical simulation of strongly stratified flow over a three-dimensional hill. *Boundary Layer Meteorology*, **107**, 81–114.

Doyle, J. D., 2005: Evaluation of coamps and wrf-arw dynamic cores for topographic flow test problems. *11th Conference on Mesoscale Processes*, Albuquerque, NM, American Meteorological Society, Poster.

Doyle, J. D. and Q. Jiang, 2006: Observations and numerical simulations of mountain waves in the presence of directional wind shear. *Quarterly Journal of the Royal Meteorological Society*, **132**, 1877–1905.

Doyle, J. D., M. Shapiro, Q. Jiang, and D. Bartels, 2004: Large-amplitude mountain wave breaking over greenland. *Journal of the Atmospheric Sciences*, **62**, 3106–3126.

Doyle, J. D. and R. B. Smith, 2003: Mountain waves over the hohe tauern: Influence of upstream diabatic effects. *Quarterly Journal of the Royal Meteorological Society*, **129**, 799–823.

Doyle, J. D., et al., 2000: An intercomparison of model-predicted wave breaking for the 11 january 1972 boulder windstorm. *Monthly Weather Review*, **128**, 901–914.

Durran, D. R., 1986: Another look at downslope windstorms. part i: The development of analogs to supercritical flow in an infinitely deep, continuously stratified fluid. *Journal of the Atmospheric Sciences*, **43**, 2527–2543.

Durran, D. R. and J. B. Klemp, 1983: A compressible model for the simulation of moist mountain waves. *Monthly Weather Review*, **111**, 2341–2361.

Durran, D. R. and J. B. Klemp, 1987: Another look at downslope winds. part ii: Nonlinear amplification beneath wave-overturning layers. *Journal of the Atmospheric Sciences*, **44**, 3402–3412.

Eckermann, S., D. Broutman, J. Ma, and J. Lindeman, 2006a: Fourier-ray modeling of short wavelength trapped lee waves observed in infrared satellite imagery near jan mayen. *Monthly Weather Review*, **134**, 2830–2848.

Eckermann, S., A. Dornbrack, S. Vosper, H. Flentje, M. Mahoney, T. Bui, and K. Carslaw, 2006b: Mountain wave-induced polar stratospheric cloud forecasts for aircraft science flights during solve/theseo 2000. *Weather and Forecasting*, **21**, 42–68.

Epifanio, C. C. and D. R. Durran, 2001: Three dimensional effects in high-drag-state flows over long ridges. *Journal of the Atmospheric Sciences*, **58**, 1051–1065.

Grubisic, V. and P. K. Smolarkiewicz, 1997: The effect of critical levels on three dimensional orographic flows: linear regime. *Journal of the Atmospheric Sciences*, **54**, 1943–1960.

Hafner, J. and S. P. Xie, 2003: Far-field simulation of the hawaiian wake: Sea surface temperature and orographic effects. *Journal of the Atmospheric Sciences*, **60**, 3021–3032.

Holton, J. R., 1992: *An introduction to dynamic meteorology.* 3d ed., Elsevier Academic Press, 511 pp.

Hunt, J. C. R., H. Ólafsson, and P. Bougeault, 2001: Coriolis effects on orographic and mesoscale flows. *Quarterly Journal of the Royal Meteorological Society*, **127**, 601–633.

Hunt, J. C. R. and W. H. Snyder, 1980: Experiments on stably and neutrally stratified flow over a model three-dimensional hill. *Journal of Fluid Mechanics*, **96**, 671–704.

Jaubert, G. and J. Stein, 2003: Multiscale and unsteady aspects of a deep fohn event during map. *Quarterly Journal of the Royal Meteorological Society*, **129**, 755–776.

Jiang, J. H., S. D. Eckermann, D. L. Wu, K. Hocke, B. Wang, J. Ma, and Y. Zhang, 2005: Seasonal variation of gravity wave sources from satellite observation. *Advances in Space Research*, **35**, 1925–1932.

Jiang, Q. and J. Doyle, 2004: Gravity wave breaking over the central alps: Role of complex terrain. *Journal of the Atmospheric Sciences*, **61**, 2249–2266.

Jiang, Q., J. Doyle, S. Wang, and R. Smith, 2007: On boundary layer separation in the lee of mesoscale topography. *Journal of the Atmospheric Sciences*, **64**, 401–420.

Kaimal, J. C. and J. J. Finnigan, 1994: *Atmospheric boundary layer flows.* 1st ed., Oxford University Press, 304 pp.

Kim, Y., S. Eckermann, and H. Chun, 2002: An overview of the past, present, and future of gravity-wave drag parameterization for numerical climate and weather prediction models. *Atmosphere-Ocean*, **41**, 65–98.

Klemp, J. and R. Wilhelmson, 1978: The simulation of three-dimensional convective storm dynamics. *Journal of the Atmospheric Sciences*, **35**, 1070–1096.

Klemp, J. B. and D. K. Lilly, 1975: The dynamics of wave-induced downslope winds. *Journal of the Atmospheric Sciences*, **32**, 320–339.

Klemp, J. B. and D. K. Lilly, 1978: Numerical simulation of hydrostatic mountain waves. *Journal of the Atmospheric Sciences*, **35**, 78–106.

Lindeman, J., D. Broutman, S. Eckermann, J. Ma, J. Rottman, and Z. Boybeyi, 2008: Mesoscale model initialization of the fourier transform method for mountain waves. *Journal of the Atmospheric Sciences*, submitted.

Miranda, P. M. A. and I. James, 1992: Non-linear three-dimensional effects of gravity-wave drag: Splitting flow and breaking waves. *Quarterly Journal of the Royal Meteorological Society*, **118**, 1057–1081.

Nappo, C., 2002: *An introduction to atmospheric gravity waves.* 1st ed., Academic Press, 305 pp.

Ólafsson, H. and P. Bougeault, 1996: Nonlinear flow past an elliptic mountain ridge. *Journal of the Atmospheric Sciences*, **53**, 2465–2489.

Peltier, W. R. and T. L. Clark, 1979: The evolution and stability of finite amplitude mountain waves. part ii: Surface wave drag and severe downslope windstorms. *Journal of the Atmospheric Sciences*, **36**, 1498–1529.

Peltier, W. R. and T. L. Clark, 1983: Nonlinear mountain waves in two and three spatial dimensions. *Quarterly Journal of the Royal Meteorological Society*, **109**, 527–548.

Pielke, R., 2002: *Mesoscale meteorological modeling*. 2d ed., Academic Press, 704 pp.

Pierrehumbert, R. T. and B. Wyman, 1985: Upstream effects of mesoscale mountains. *Journal of the Atmospheric Sciences*, **42**, 977–1003.

Rasmussen, R. M., P. Smolarkiewicz, and J. Warner, 1989: On the dynamics of hawaiian clud bands: comparison of model results with observations and island climatology. *Journal of the Atmospheric Sciences*, **46**, 1589–1608.

Rasmussen, R. M., P. Smolarkiewicz, and J. Warner, 1993: On the dynamics of hawaiian cloud bands. part iii: Local aspects. *Journal of the Atmospheric Sciences*, **50**, 1560–1572.

Reisner, J. and P. Smolarkiewicz, 1994: Thermally forced low froude number flow past three-dimensional obstacles. *Journal of the Atmospheric Sciences*, **122**, 1175–1195.

Schär, C. and D. Durran, 1997: Vortex formation and vortex shedding in continuously stratified flows past isolated topography. *Journal of the Atmospheric Sciences*, **54**, 534–554.

Scorer, R. S., 1949: Theory of lee waves of mountains. *Quarterly Journal of the Royal Meteorological Society*, **75**, 41–56.

Sheppard, P. A., 1956: Airflow over mountains. *Quarterly Journal of the Royal Meteorological Society*, **82**, 528–529.

Skamarock, W. C. and J. B. Klemp, 1992: The stability of time-split numerical methods for the hydrostatic and nonhydrostatic elastic equations. *Monthly Weather Review*, **120**, 2109–2127.

Skamarock, W. C., J. C. Klemp, J. Dudhia, D. O. Gill, D. M. Barker, W. Wang, and J. G. Powers, 2005: A description of the advanced research wrf version 2. NCAR Technical Note NCAR/TN468+STR, National Center for Atmospheric Research, 100 pp.

Smith, R., 1979: The influence of mountains on the atmosphere. *Advances in Geophysics*, **60**, 87–230.

Smith, R., 1985: On severe downslope winds. *Journal of the Atmospheric Sciences*, **42**, 2597–2603.

Smith, R. B., J. Doyle, Q. Jiang, and S. Smith, 2007: Alpine gravity waves: Lessons from map regarding mountain wave generation and breaking. *Quarterly Journal of the Royal Meteorological Society*, **133**, 917–936.

Smith, R. B. and V. Grubisic, 1993: Aerial observations of hawaii's wake. *Journal of the Atmospheric Sciences*, **50**, 3728–3750.

Smith, R. B., S. Skubis, J. Doyle, A. Broad, C. Kiemle, and H. Volkert, 2002: Mountain waves over mont blanc: Influence of a stagnant boundary layer. *Journal of the Atmospheric Sciences*, **59**, 2073–2092.

Smith, S. A. and A. Broad, 2003: Horizontal and temporal variability of mountain waves over mont blanc. *Quarterly Journal of the Royal Meteorological Society*, **129**, 2195–2216.

Smolarkiewicz, P. K., R. M. Rasmussen, and T. Clark, 1988: On the dynamics of hawaiian cloud bands: island forcing. *Journal of the Atmospheric Sciences*, **45**, 1872–1905.

Smolarkiewicz, P. K. and R. Rotunno, 1989a: Low froude number flow past three-dimensional obstacles. part i: Baroclinically generated lee vortices. *Journal of the Atmospheric Sciences*, **46**, 1154–1164.

Smolarkiewicz, P. K. and R. Rotunno, 1989b: Low froude number flow past three-dimensional obstacles. part ii: Upwind flow reversal zone. *Journal of the Atmospheric Sciences*, **47**, 1498–1511.

Snyder, W. H., R. S. Thompson, R. E. Eskridge, R. E. Lawson, I. P. Castro, J. T. Lee, J. C. R. Hunt, and Y. Ogawa, 1985: The structure of strongly stratified flow over hills: dividing streamline concept. *Journal of Fluid Mechanics*, **152**, 249–288.

Trombetti, F. and F. Tampieri, 1987: An application of the dividing streamline concept to the stable airflow over mesoscale mountains. *Monthly Weather Review*, **115**, 1802–1806.

Volkert, H., C. Keil, C. Kiemle, G. Poberaj, J. Chaboureau, and E. Richard, 2003: Gravity waves over the eastern alps: A synopsis of the 25 october 1999 event (iop 10) combining in situ and remote-sensing measurements with a high resolution simulation. *Quarterly Journal of the Royal Meteorological Society*, **129**, 777–797.

Wang, J. J., H. H. Juang, K. Kodama, S. Businger, Y. Chen, and J. Partain, 1998: Application of the ncep regional spectral model to improve mesoscale weather forecasts in hawaii. *Weather and Forecasting*, **13**, 560–575.

Wang, T. and Y. Lin, 1999: Wave ducting in a stratified shear flow over a two-dimensional mountain. part ii: Implications for the development of high-drag states for severe downslope windstorms. *Journal of the Atmospheric Sciences*, **56**, 437–452.

Wicker, L. J. and W. Skamarock, 2002: Time-splitting methods for elastic models using forward time schemes. *Monthly Weather Review*, **130**, 2088–2097.

Wurtele, M., R. Sharman, and A. Datta, 2002: Atmospheric lee waves. *Annual Review of Fluid Mechanics*, **28**, 429–476.

Xie, S. P., W. T. Liu, Q. Liu, and M. Nonaka, 2001: Far-reaching effects of the hawaiian islands on the pacific ocean-atmosphere system. *Science*, **292**, 2057–2060.

Zhang, Y., Y. Chen, and K. Kodama, 2005: Validation of the coupled ncep mesoscale spectral model and an advanced land surface model over the hawaiian islands. part ii: A high wind event. *Weather and Forecasting*, **20**, 873–895.

Curriculum Vitae

John Lindeman was born in Alexandria, VA in 1972. As an undergraduate of Milersville University in Millersville, PA, John majored in meteorology and minored in mathematics, and graduated in May, 1995. That Fall, John went to England for a master's degree in Weather, Climate, and Modelling at the University of Reading. In 2001, John began working at the Naval Research Laboratory in Washington, DC as a research assistant in the field of mountain wave modeling. John began his PhD at George Mason University in the Fall of 2003, and was funded by NRL until 2005 when Dave Broutman secured his funding through a National Science Foundation grant. The research presented in this dissertation has been for the benefit of NRL.